A.I. Alikhanian National Scientific Laboratory

Armine Amekhyan

Dark Matter and Galactic Halos

Thesis for acquiring the degree of candidate of physical-mathematical sciences in division 01.04.02, Theoretical Physics

Supervisor: Prof. V. G. Gurzadyan

Yerevan 2020

Contents

List of Figures

List of Tables

-

Introduction

Our understanding of the Universe i.e. of its origin, structure and evolution, is essentially based on the General Relativity and Einstein equations which are given as [1], [2], [3]

$$R_{\mu\nu} - \frac{1}{2} g_{\mu\nu} R + \Lambda g_{\mu\nu} = \frac{8\pi G}{c^4} T_{\mu\nu}, \tag{1}$$

where $T_{\mu\nu} = (\rho + p/c^2) u^\mu u^\nu - p g^{\mu\nu}$ is the energy-momentum tensor, $R_{\mu\nu}$ Ricci tensor and Λ is the cosmological constant.

The observational fact that our Universe, on the large scales, is homogeneous and isotropic enables one to use Friedmann–Robertson–Walker (FRW) metric

$$ds^2 = c^2 dt^2 - R^2(t) \left[\frac{dr^2}{1 - Kr^2} + r^2 (d\theta^2 + \sin^2 \theta d\phi^2) \right], \tag{2}$$

where the curvature $K = [\pm 1; 0]$ is constant, as a consequence of the homogeneity and isotropy of the space-time, $R(t)$ is the scale factor and (r, θ, ϕ) are the comoving coordinates. By solving Einstein equations e.g. for FRW metric with a contracted energy-momentum tensor ($T = \rho c^2 - 3p$) one can find the Friedmann equations

$$\ddot{R} = -\frac{4\pi G}{3} \left(\rho + 3p/c^2 \right) R + \frac{1}{3} \Lambda c^2 R, \tag{3}$$

$$\dot{R}^2 = \frac{8\pi G}{3} \rho R^2 + \frac{1}{3} \Lambda c^2 R^2 - c^2 K. \tag{4}$$

These equations describe the evolution of the scale factor. Currently, the observations support the zero curvature of the Universe, so below we will adopt the "flat" Universe model. The cosmological constant Λ is attributed to the to vacuum energy density

$$\rho_\Lambda = \frac{\Lambda c^2}{8\pi G}. \tag{5}$$

The "matter" term contains all types of matter (including dark and baryonic) and radiation (including photons and neutrinos), so that the matter density is changing during the evolution, while the vacuum density remains constant i.e:

$$\rho(t) = \rho_{m,0}\left[\frac{R_0}{R(t)}\right]^3 + \rho_{r,0}\left[\frac{R_0}{R(t)}\right]^4 + \rho_\Lambda, \tag{6}$$

where the zero index indicates the parameters' present day values.

The expansion of the Universe is characterized by the Hubble parameter $H(t) = \frac{\dot{R}(t)}{R(t)}$. Namely, the relation between galaxies recessional velocity and distance is described by Hubble law [4], [5], [6], written as

$$v = H_0 d, \tag{7}$$

where H_0 is present-day value of the Hubble parameter. Observationally, the redshift z is the parameter determining the expansion, i.e. when in the expanding space-time the frequency of the outgoing object is decreased for the observer as

$$1 + z = \frac{\nu_e}{\nu_r} \equiv \frac{R(t_r)}{R(t_e)}. \tag{8}$$

The outstanding observational discovery of the recent decades is the fact of the accelerating expansion of the Universe [7, 8]. Together with a bunch of other observational data, it is concluded that the major fraction of the matter of the Universe is dark, i.e. the form

of dark matter and of dark energy. For the density parameters one has

$$\Omega_i(t) = \frac{8\pi G}{3H^2(t)}\rho_i(t), \tag{9}$$

where the index i denotes the components of the cosmological fluid and [9]

$$\Omega_{total} = \Omega_M + \Omega_R + \Omega_\Lambda, \tag{10}$$

where $\Omega_M = \Omega_{DM} + \Omega_B$ is the matter density parameter, including dark matter (Ω_{DM}) and baryonic matter (Ω_B), meantime Ω_R and Ω_Λ are radiation and dark energy densities, accordingly. Note, that the major components are the dark energy and dark matter (DM), while the radiation density fraction is far small. As reported by latest *Planck Collaboration's* study [11], present-day values of Ω_Λ and Ω_M are 0.6847 ± 0.0073 and 0.3111 ± 0.0056, respectively, i.e. the DM density is significantly higher than the baryonic matter density.

Despite numerous studies and hypotheses, the nature of dark matter and dark energy is still unknown. In this study we will investigate DM indications based on the data on galactic halos, including those obtained by the *Planck* mission in the microwaves.

Let us inquire into the DM problem in more details. The first observational evidence of DM was found by F. Zwicky [12], who obtained the radial velocities of several galaxies in Coma cluster. He used the virial theorem, which states that

$$2K + W = 0, \tag{11}$$

where K is the total kinematic energy of a self-gravitating, stationary system $K = \frac{1}{2}\sum_{i=1}^{N} m_i \vec{v_i}^2$ and $W = \frac{-G}{2}\sum_{i=1}^{N}\sum_{j\neq i}\frac{m_i m_j}{\|\vec{r_i}-\vec{r_j}\|}$ is the gravitational potential energy. If we assume that the

objects of self-gravitating system have identical masses, then this yields

$$m = \frac{v^2 r}{G} \tag{12}$$

Thus, Zwicky estimated the total mass of Coma cluster $3 \times 10^{14} M_{\odot}$, while the observable (luminous) mass was $10^{12} M_{\odot}$. So, it was assumed that there is an additional undetectable mass (i.e. DM). Similar analysis was performed by [13] for Virgo cluster. The author had calculated radial velocities over 30 galaxies and had obtained mass-to-light ratio equal to 100. Note, that if one assumes that there is no any unseen mass, then galaxies will rotate very fast (because of large mass) and eventually escape from the cluster. So, it was stated that the DM is an important component of clusters. Similar evidences were found for galaxies, again using the virial theorem [14]. Using the rotational velocities in galaxies it was shown that galaxies have also unseen mass, larger than the visible one. Namely, according to Newtonian gravity the orbital velocity of a point object should follow Keplerian law: $V \propto r^{-1/2}$. However, the observations show that $V = constant$ for enough large radii. An evidence for existence DM comes from an object, called bullet cluster. It consists of two colliding clusters (one of them more massive) separated on $720 kpc$, and weak gravitational lensing of this object shows that centers of the total and baryonic masses do not coincide, which means that there is fraction of unseen mass.

In order to clarify the properties of DM it is important to consider the evolution of the Universe during the large-scale structure formation. From this point of view DM is classified as cold dark matter (CDM), warm dark matter (WDM) and hot dark matter (HDM). CDM is assumed to be non-relativistic, ideal fluid. Before recombination epoch (or more exactly radiation domination epoch), these perturbations grow logarithmically [3]

$$\delta_{CDM}(\eta) = -9\Phi_{(i)}(log\frac{k\eta}{\sqrt{3}} + C - \frac{1}{2}) \tag{13}$$

where $\Phi_{(i)}$ is the initial gravitational potential, η and k are conformal time and momentum and C is Euler constant. Gravitational potential, produced by CDM is written as

$$\Phi_{CDM}(\eta) = -\frac{a^2(\eta)}{k^2} 4\pi G \rho_{CDM} \delta_{CDM}(\eta), \tag{14}$$

and after recombination the perturbations become

$$\delta_{CDM}(\eta_r) = -\frac{k^2}{4\pi G \rho_{CDM}(\eta_r) a^2(\eta_r)} \Phi(\eta_r). \tag{15}$$

Structure formation process, starting from linear scalar perturbations, continues also in the non-linear regime, which leads to formation of the first gravitationally bound structures. Since CDM and baryons are non-relativistic, their self-gravity is dominant, thanks to which they are collapsed to the overdense regions. The relativistic fluid, can easily pass through this environment. The situation is significantly different in the case of HDM and WDM scenario, where ideal flux approximation is not valid. In this case a suppression of perturbations (of gravitation potential as well) caused by free streaming effect, will occur.

Without having any knowledge about DM composition, it is still possible to study its spatial distribution via numerical simulations and comparison of the density profiles with observational data. In this study we will use three DM distribution profiles. First, as suggested by [15], considered the evolution of more than 262000 particles in $30 Mpc$ sized box. During the evolution the overdense regions are formed due to gravitational collapse (as expected by structure formation process). As a result the derived dark matter density distribution (called Navarro-Frenk-White (NFW) distribution) inside spherical halo is

$$\frac{\rho_r}{\rho_{crit}} = \frac{\delta_0}{(r/r_c)(1 + r/r_c)^2}, \tag{16}$$

where $\rho_{crit} = \frac{3H^2}{8\pi G}$ is critical density, r_c is characteristic radius. δ_0 is called the overdensity

parameter and defined as:

$$\delta_0 = \frac{200}{3}\frac{c^3}{(ln(1+c) - c/1+c)}, \tag{17}$$

where c is concentration of the particles. The dark matter mass inside r radius is

$$M(r) = 4\pi\rho_{crit}\delta_0 r_s^3 \left[\frac{1}{1+cx} - 1 + ln(1+cx)\right], \tag{18}$$

where $x = r/R_{200}$. R_{200} is the virial radius defined as the radius at which the density of overdense region (where virial equilibrium holds) is $\rho = 200\rho_{crit}$. Note that, it is an approximated estimation and can be changed with different DM models. Finally, the DM velocity distribution, which ensures the flatness of rotational curves is

$$V_{NFW}^2(r) = 4\pi G\rho_c \frac{r_c^3}{r}[ln(1+\frac{r}{r_c}) - \frac{\frac{r}{r_c}}{1+\frac{r}{r_c}}] \tag{19}$$

So, NFW distribution perfectly describes flat rotational curves. Next DM distribution profile is Burkert profile [16], where DM density and velocity distributions are given by:

$$\rho_{Burkert}(r) = \frac{\rho_c}{\left(1+\frac{r}{r_c}\right)\left[1+(\frac{r}{r_c})^2\right]}, \tag{20}$$

$$V_{Burkert}^2(r) = 2\pi G\rho_c \frac{r_c^3}{r}\Big\{\left[ln(1+\frac{r}{r_c})\sqrt{1+(\frac{r}{r_c})^2}\right] - \arctan(\frac{r}{r_c})\Big\}. \tag{21}$$

The third profile which we will use is the Moore profile [17]. The latter is derived from more efficient simulation parameters. Namely, the number of particles (over 10^6) and box size ($100Mpc$) are significantly higher, than in the NFW case and the density distribution is

$$\rho_{Moore}(r) = \frac{\rho_c}{(\frac{r}{r_c})^{1.5}\left[1+(\frac{r}{r_c})^{1.5}\right]}, \tag{22}$$

while velocity distribution becomes

$$V^2_{Moore}(r) = \frac{8}{3}\pi G\rho_c \frac{r_c^3}{r} ln\Big[1 + (\frac{r}{r_c})^{1.5}\Big]. \tag{23}$$

Besides the intensely studied particle models for DM, that problem is studied also within the modified gravity models such as the Modified Newtonian dynamics (MOND) [18]. In that approach it is suggested that in outer parts of galaxies, where the objects have very low acceleration, the gravitational force is expressed not via Newton's law $F = m \times a$, but "Milgrom's law" $F = m\mu(\frac{a}{a_0})a$. So, when $a \ll a_0$, where a is acceleration of the object located far from center of the galaxies, and a_0 is a constant, the gravitational force is expressed as: $F = m\frac{a^2}{a_0}$. This approach aims to describe the existence of flat rotation curves of galaxies, but it fails to explain the DM problem in galaxy clusters and more general in the cosmological context. Another model to explain DM halo features is $f(R)$ theory [19], [20], via which one can obtain flat rotation curves of galaxies. In recent studies [21], [22] the authors have examined the DM problem for galaxy and galaxy clusters using modified weak-field limit of General Relativity involving the cosmological constant (i.e. weak-field Λ).

Our study aims to investigate the DM problem regarding the dark galactic halos [23], taking into account the possible contribution of circumgalactic dust in dark matter halo mass. The importance of such study is also due to the available microwave band data from the *Planck* satellite. Namely, the revealed microwave asymmetry for a sample of nearby galaxies can be made linked to the dust optical depth via Doppler shift formula

$$\frac{|\Delta T|}{T} = \frac{2vsini}{c}\tau. \tag{24}$$

Then using two dust models, we derive rotational curves for large radii, typically $30-100kpc$. Finally, having dust velocities and masses on the large radii it is not difficult to evaluate the fit to the theoretical models (NFW, Moore or Burkert profiles).

The thesis consists of three chapters.

In the first chapter we describe the main physical mechanisms for the Cosmic Microwave Background (CMB) local anisotropies. Particularly, a mechanism for the primary CMB anisotropy can be non-uniform gravitational and adiabatic perturbations, the Sachs–Wolfe effect. There is also a secondary CMB anisotropy arisen by several physical process such as the Sunyaev-Zeldovich effect, the scattering of CMB photons on the high energy electrons in the galaxy cluster scale. The theoretical basis of the analysis and data processing techniques, which are used during further calculations, are presented. Namely, in order to calculate CMB anisotropies at different frequencies for several galaxies, we use HEALPiX scheme for sky pixelization as well as publicly released *Planck* low Frequency Instrument (LFI) and High Frequency Instrument (HFI) data. Each of these issues is described in details.

In the second chapter CMB temperature asymmetry is studied for two nearby galaxies, M81 and M104 for 4 frequency bands. For M81 galaxy we find temperature asymmetry with $50-70\mu K$ values and up to 1.5° galactocentric distances. The asymmetry is frequency independent and is correlated with rotational direction of the galaxy. Namely, the temperature of that side, which rotates in our direction, is higher than of the opposite side, thus indicating the Doppler origin of the effect. This and other sources of asymmetry are also discussed. For M104 galaxy we consider temperature asymmetry in four radial distances: 0.2°, 0.4°, 0.6°, 1.0°. The north–south temperature asymmetry increases with increasing galactocentric radius from $25\mu K$ (within 0.2°) up to $65\mu K$ (within 0.6°). As in the M81's case, for M104 also there was rotation-oriented temperature asymmetry. The possible contribution of the cold-gas clouds in halo mass also is discussed.

In the third chapter we investigate the interstellar dust's contribution in the M31, M81 and M82 galaxies halos. For this purpose we need to estimate dust's rotational velocities and compare it with DM distributions profiles (i.e. NFW, Moore and Burkert). First, we

estimate CMB asymmetry values on the large radial distances (30-100kpc), at three high frequencies: 353 GHz, 545 GHz and 857 GHz. Then we use two dust models (GNILC and DL07) for optical depth values evaluation and finally we check it for radial distances. At the end, by considering the CMB asymmetry data and dust optical depth values, we obtain the dust rotational velocities. Then, we compare the results of dust velocity and DM profiles. We also compare the modified gravity models (now widely used for dark matter interpretation) with respect to the parameters of the dark halo configurations which we had obtained.

The main results of the thesis are formulated in Conclusions.

The results of the thesis are published in the papers [24, 25, 26, 27].

Acknowledgments

I would like to express my deep gratitude to my supervisor, Professor V.G. Gurzadyan, who introduced me the field of modern Cosmology. His knowledge and integral view on the research and his advice for providing 'only high-quality work and never less' have made a deep impression on me.

I am grateful to my co-authors, especially to F. De Paolis, A.L. Kashin, A. Stepanian and S. Sargsyan.

My thanks are due to colleagues of the Alikhanian National Laboratory for their valuable advice and friendly help. The extensive discussions at various phases of my work have been very helpful.

Chapter 1

Analysis of Cosmic Microwave Background maps

1.1 Introduction

The discovery of Cosmic Microwave Background radiation (CMB) [28] was undoubtedly one of the most important scientific achievements in cosmology. It is the key experimental fact that confirms hot Big Bang model of the Universe, according to which the Universe has started to expand from singularity, with hot and very dense matter epoch, then cooling adiabatically, see [1]. At the very beginning, just after Big Bang at $T > 10^{15}K$, strong and electroweak interactions were still unified. Then comes the weak interaction era, when neutrinos appeared. The Universe cooled, until it reached at $T < 10^{9}K$, when the nucleosynthesis processes occur. Cosmic fluid (radiation and matter) was in thermal equilibrium. In this stage ideal gas approximation (i.e. no interaction between particles) is valid, hence for bosons (like photons or gauge bosons) the particle number density is given by

$$n(E)dE = \frac{4\pi g_B}{h^3}\frac{E^2 dE}{c^3}\frac{1}{e^{E/KT}-1}, \tag{1.1}$$

where g_B is the number of internal degrees of freedom. While for fermions the number density is

$$n(E)dE = \frac{4\pi g_F}{h^3}\frac{E^2 dE}{c^3}\frac{1}{e^{E/KT}+1}. \tag{1.2}$$

Total energy density is obtained by integrating Eqs.(1.1, 1.2)

$$U = \frac{G}{2}aT^4, \tag{1.3}$$

where $G = \sum_i g_{B_i} + \sum_i g_{F_i}$. For very high temperatures ($KT \gg 300Gev$) the particle in equilibrium with photons. However, due to expansion, the temperature fall down and non-ralativistic matter is described by Maxwell–Boltzmann distribution:

$$n(v)dv = 4\pi N(\frac{m}{2\pi KT})^{3/2}v^2 e^{-\frac{mv^2}{2KT}}dv. \tag{1.4}$$

Moreover, velocities of particles are inversely proportional to scale factor

$$v \propto \frac{1}{R(t)}. \tag{1.5}$$

During expansion, the matter density is changed according to

$$\rho_m \propto (1+z)^3, \tag{1.6}$$

while for radiation density we have

$$\rho_r \propto (1+z)^4. \tag{1.7}$$

Therefore the redshift (z_{eq}) at which $\rho_r = \rho_m$ is

$$1 + z_{eq} = \frac{\rho_M}{\rho_R} = 2.4 \times 10^4 \Omega_M h^2. \tag{1.8}$$

At $z \simeq 1100$ electrons and photons are coupled through Thomson scattering, with

$$\sigma_T = \frac{8\pi\alpha^2}{3m_e^2} = 6.65 \times 10^{-29} m^2. \tag{1.9}$$

Also, the mean-free-path of photon is defined as

$$\lambda = \frac{1}{n_e \sigma_T}. \tag{1.10}$$

At $T \simeq 3000K$ temperature photon's number density became less than baryon's density and energy above than hydrogen ionization energy (13.6eV). So, protons (electrons) remained coupled to neutral hydrogen or helium. This is the well known recombination era. Hydrogen building process is described by Saha equation

$$\frac{n_p n_e}{n_H} = \frac{(2\pi m_e kT)^{3/2}}{h^3} e^{-\chi/kT}, \tag{1.11}$$

where χ is the ionization energy of hydrogen. After recombination, photons were decoupled from electrons and radiation filled the whole Universe. Originating just after Big Bang, CMB contains wealth information not only about the early Universe, but also about its dynamics and geometry. CMB photons are described by Bose-Einstein distribution

$$f(p) = \frac{1}{e^{p/T} - 1}, \tag{1.12}$$

where p is the photon momentum. While the number density (n_γ) and energy density are (ρ_γ) written as:

$$n_\gamma = \int \frac{4\pi p^2 dp}{(2\pi)^3} f(p) \approx \frac{2.4}{\pi^2} T^3, \tag{1.13}$$

$$\rho_\gamma = \int \frac{4\pi p^2 dp}{(2\pi)^3} p f(p) \approx \frac{\pi^2}{15} T^4. \tag{1.14}$$

Because of expansion, the momentum and temperature of the CMB photon are also redshifted

$$1 + z \equiv \frac{p}{p_0}, \tag{1.15}$$

$$1 + z \equiv \frac{T}{T_0}. \tag{1.16}$$

CMB temperature is decreased with an inverse proportion to the size of the Universe $T \propto \frac{1}{a}$, while the density is changed as $\rho_\gamma \propto \frac{1}{a^4}$. Nowadays, the CMB radiation temperature is 2.76 K, described by nearly perfect blackbody spectrum.

An informative property of the CMB radiation are the angular fluctuations induced by inhomogeneities (for example matter's density perturbations) of last scattering surface (primary anisotropies), as well as interactions between CMB photons and particles in the line of sight (secondary anisotropies). This phenomenon was first detected by the Cosmic Background Explorer (COBE) satellite [29] on the order of 10^{-5}, over wide range of frequencies. There are three possible phenomena, which can be explained by primary anisotropy: gravitational (Sachs–Wolfe) perturbations, where there are non-uniform (perturbed) gravitational potential between two particular points, thanks to which the temperature deviation occurs between above mentioned points. This is caused by gravitational redshifting (expansion). Next source of primary asymmetry are adiabatic perturbations, due to radiation compression in at the high density regions. It arose, when the matter and radiation were

still coupled. Finally, the third reason of the primary anisotropy is the non-zero velocity of plasma (electrons and photons) at recombination era. Therefore, it can lead to Doppler shifting of the frequency. Various physical processes can cause secondary asymmetry, however main contributors are the integrated Sachs-Wolfe effect, when photons are traveling in linearly varying gravitational field, the Rees-Sciama effect, when CMB photons are traveling in non-linearly varying gravitational field, gravitational lensing of the CMB, the Sunyaev-Zeldovich or the kinematic Sunyaev-Zeldovich effects and so on. Generally, CMB radiation anisotropy strongly depends on the given angular size. For example primary asymmetry has greater than 7° angular scales, while secondary fluctuations has more small angular sizes. We will discuss these aspects with more details in the next paragraphs. After the data of COBE mission were provided, several ground-based and space-based experiments were performed to make more and more accurate CMB measurements, see [10]. The experiments were aimed to increase the quality of CMB maps and extend both frequency coverage and spatial resolution range. For this purpose, it is important to have not only highly sensitive instruments, but also a powerful tools for numerical calculations (to calculate power spectrum of CMB) and data analysis (to separate of CMB component from background). A successful ground-based missions, which have measured CMB asymmetry at the small scales are South Pole Telescope (SPT) [30] and Atacama Cosmology Telescope (ACT) [31], with 10m and 6m diameters, accordingly. The another step of CMB studies began with launching of Wilkinson Microwave Anisotropy Probe (WMAP) [32] proposed by NASA. The WMAP sky maps have minimum systematic errors and covers $23 - 94$ GHz frequency range. Its full-width-half-max (FWHM) antenna's beam resolution is 13 arcmin , which is significantly higher than the resolution of COBE mission. During nine working years, WMAP gathered huge amount of data about the Universe content, geometry, evolution and so on, which were published as 3-year [33], 5-year [34], 7-year [35], and 9-year [36] WMAP data. The third generation of CMB satellite, is ESA's *Planck* mission [37]. Having higher angular resolution

than WMAP, *Planck* was able to measure and study not only CMB anisotropy, but also interstellar medium components, galaxy clusters, extragalactic radio and infrared sources and so on. In this thesis, the *Planck* data over $30 - 857$ GHz frequencies is used to study CMB Doppler-induced asymmetry of halos for 4 galaxies: M31, M82, M81 and M104.

1.2 Sunyaev-Zeldovich effect

The Sunyaev-Zeldovich (SZ) effect reflects small angular distortions of the CMB spectrum arisen from inverse Compton scattering on high energy electrons. The latter occurs at the inter-cluster medium (ICM) of galaxy clusters, when CMB photon meets the electron. After scattering, the energy of the CMB photon is amplified by $\frac{k_B T_e}{m_e c^2}$, which leads to distortion of the CMB spectrum. Since hot gas fraction in the whole cluster's mass is small, the probability of inverse Compton scattering is only $\simeq 1\%$. As a result the expected distortion is also small ($\simeq 1mK$), while the electron energy is detectable in the X-ray emission. Because of this effect, the intensity of CMB is decreased at low frequencies and increased once the frequency range becomes higher. The SZ effect is independent from the redshift and has two types: thermal Sunyaev-Zeldovich effect (tSZ) and kinematic Sunyaev-Zeldovich effect (kSZ). The derivation of the SZ effect is presented in papers [38], [39] by Sunyaev and Zeldovich. Here we will briefly discuss the important aspects of this effect.

1.2.1 Thermal Sunyaev-Zeldovich effect

Small scale distortions of the CMB spectrum, described above, is mathematically expressed as the ratio of the tSZ-inducted CMB temperature fluctuation (ΔT_{tSZ}) and undistorted CMB temperature (T_{CMB}) at the $x \equiv \frac{h\nu}{k_B T_{CMB}}$ frequency

$$\frac{\Delta T_{tSZ}}{T_{CMB}} = f(x) \int n_e (\frac{k_B T_e}{m_e c^2}) \sigma_T dl. \tag{1.17}$$

The integrand is called the Comptonization parameter (y), which for isothermal clusters is expressed as the product of the optical depth and the coefficient of fractional energy gained per scattering. Moreover, σ_T is Thomson cross-section (because Compton scattering is in Thomson limit $h\nu \ll mc^2$), T_e, n_e, and $m_e c^2$ are electron's temperature, number density and rest mass energy, respectively. Finally, the $f(x)$ is frequency-dependent part of tSZ

$$f(x) = (x\frac{e^x+1}{e^x-1} - 4)(1 + \delta_{tSZ}(x, T_e)), \tag{1.18}$$

where $\delta_{tSZ}(x, T_e)$ is relativistic correction, which is negligible for non relativistic electrons. Indeed, the Eq.(1.17) is the consequence of the solution of Kompaneets equation, which describes the change of photon number during Compton scattering by isotropic, non relativistic electrons [40]. It should be noticed that besides the temperature form Eq.(1.17), it is also possible to express the tSZ effect according to intensity

$$\Delta I_{tSZ} = g(x) I_0 y, \tag{1.19}$$

where $I_0 = 2(\frac{(k_B T_{CMB})^3}{(hc)^2})$ and $g(x)$ is the frequency-dependent function written as

$$g(x) = \frac{x^4 e^x}{(e^x-1)^2} \times (x\frac{e^x+1}{e^x-1} - 4)(1 + \delta_{tSZ}(x, T_e)). \tag{1.20}$$

In that case, when the velocity distribution of electrons in ICM is isotropic, the distortion of CMB spectrum is obtained through T_e. Namely, during the scattering, the CMB photons accumulate energy from ICM electron, which leads to the shift of their spectrum from Rayleigh–Jeans to Wien range. So, it is possible to register that shifting. It should be noticed that, all above considerations are valid in the non-relativistic limit. However, relativistic corrections are also significantly important especially at the high frequencies. In addition, it is possible to detect new large distanced galaxy clusters, as well as to estimate

their shape, mass of hot gas in ICM, angular size and so on, through SZ effect. There are many studies of SZ effect. An interesting result was obtained by *Planck* collaboration, which they had examined tSZ effect toward Virgo cluster [41]. They found an excess of tSZ maps, extending beyond from the virial radius. Recently, the mass of neutrinos have been included in the SZ power spectrum. [42].

1.2.2 Kinematic Sunyaev-Zeldovich effect

The origin of kSZ effect is cluster bulk motion with respect to CMB, which leads to Doppler shifting of the CMB temperature. In the non-relativistic limit it is written as

$$\frac{\Delta T_{kSZ}}{T_{CMB}} = -\tau_e(\frac{v_{pec}}{c}), \tag{1.21}$$

where v_{pec} is cluster velocity projected along the line of sight. The intensity shifting is

$$\Delta I_\nu \approx -I_0(\frac{x^4 e^x}{(e^x-1)^2})y_{ksz}, \tag{1.22}$$

where $I_0 = \frac{2(k_B T_{CMB})^3}{(hc)^2} = 270.33[\frac{T_{CMB}}{2.7255k}]^3 Mjy/sr$, and y_{ksz} is the Comptonization parameter for kSZ.

1.2.3 The rotational-kinematic-Sunyaev-Zeldovich imprint on the CMB

Although kSZ effect is typical for galaxy clusters, it can be observed in the individual galaxies, particularly in circumgalactic medium (CGM), too. CGM is a mixture of both cool and hot matter, with a very complicated dynamics. In this case also CMB photon can interact with hot electrons, which leads to small angular scale distortions of the CMB spectrum. Rotational kSZ effect can be detected via CMB data stacking analysis [23].

In the case of clusters, the temperature variation, caused by kSZ, depends on the hot gas electrons' peculiar velocity and optical depth, which in its turn is determined through electron number density along the line-of-sight. rotating CGMs is distribution of free electrons.

These definitions remain valid also for rotating CGMs. Assuming that the distribution of hot electrons in CGM is spherically symmetric, one can reformulate Eq.(1.21), in such a way that it becomes applicable for rotating gaseous halos [23]

$$\frac{\Delta T}{T}(\vec{n}) = \frac{\sigma_T}{c}\int n_e \vec{v}\times\vec{n}dl = \frac{\sigma_T}{c}\int n_e(r)v(R)\cos\phi\sin i, \tag{1.23}$$

where $\vec{n}$ is the direction along which the CMB temperature measurement is performed. Meantime, σ_T, n_e and $\vec{v}$ are Thomson cross section, electron's number density and velocity, respectively. In the last part r is the distance from center of halo and R is the radius within which the hot plasma is rotating. Moreover, ϕ and i are azimuthal and inclination angles. So, the most important parameters are the electron distribution profile and velocity. In CGM, electron distribution is determined via multi-phase atmospheric model [43], according to which the hot gas is cooled down and reaches at hydrostatic equilibrium. So, the electron density is defined as:

$$n_e(\zeta) = n_e^c[1+\frac{3.7}{\zeta}\ln(1+\zeta) - \frac{3.7}{\zeta_c}\ln(1+\zeta_c)]^{\frac{3}{2}}, \tag{1.24}$$

where ζ_c is cooling radius and n_e^c is the density, above which the cooling process is occurred. In order to estimate the electron velocity profile, it is assumed that CGM rotates with the halo's circular velocity:

$$v_c(r) = \sqrt{\frac{4\pi G r_s^2[\ln(1+r) - r(1+r)^{-1}]}{r}} \tag{1.25}$$

where r is the cylindrical radial coordinate (because velocity field has cylindrical symmetry).

In this case the spin parameter of the halo (λ) is 1, while the typical value of spin parameter for halo is $\lambda = 0.05$ [44]. For the case $\lambda < 1$ the velocity is expressed as: $v(r) = f(r, M_v)v_c(r)$. Thus, the velocity field depends not only on electrons' distance from the center of halo, but also on their masses i.e. $f = min\{m \log \frac{R}{R_{vir}} + 0.1, 1\}$, where $m = -6 \times 10^{-6}(\log M_v^2) + 3.2 \times 10^{-1} \log M_v - 4.4$. Velocities, defined in this way are significantly slow than those in Eq.(1.25).

For extracting rkSZ signal from CMB and noise the [23] authors were used aperture filter and matched filter. In the first approach a direct measurement is performed to fix the difference of CMB temperature between two halves, while in the second method, the form (profile) of expected rkSZ signal is taken into account. The magnitude of CMB signal is significantly higher than rkSZ, thus a large number of galaxies (nearly $10^6 - 10^8$) is needed to extract this effect from CMB and noise (with 3σ confidence level). However, the matched filtering method works more effective and reduces the number of required galaxies.

1.3 CMB maps: HEALPiX system

1.3.1 The Sachs-Wolfe effect, power spectrum

Generally, there are three quantity, which are possible to measure in the CMB experiments. They are frequency spectrum ($f(\nu)$), temperature (T($\mathbf{n}$)) and polarization. However, for our analysis the crucial parameter is temperature, particularly its anisotropy, which we discuss with more details.

Because CMB radiation anisotropy $\Theta(\mathbf{n}) = \frac{\Delta T}{T}$, depends on the given point of the sky (i.e. defined on the sphere), one can mathematically express it as a spherical harmonics expansion of the $\Theta(\mathbf{n})$:

$$\Theta(\mathbf{n}) = \sum_{l=2}^{\infty} \sum_{m=-l}^{l} a_{lm} Y_{lm}(\mathbf{n}), \tag{1.26}$$

where the a_{lm} coefficients, which are form orthonormal basis on the sphere $\int d\Omega_n Y_{lm}(\mathbf{n}) Y^*_{l'm'}(\mathbf{n}) =$

$\delta_{ll'}\delta_{mm'}$ is temperature fluctuations for given angular multipole, with zero mean value. It is well-known that CMB radiation temperature fluctuations have Gaussian distribution, so one can calculate power spectrum (C_l) of these fluctuations as follows:

$$\langle a_{lm}a^*_{l'm'}\rangle = \delta_{ll'}\delta_{mm'}C_l, \tag{1.27}$$

where l is the multipole, determined by angular scale (α) on the sky $l = \frac{\pi}{\alpha}$. As follows from Eq.(1.26) there is a limitation for multipoles (l). Actually, l is determined by harmonics via m-modes $m \in [-l; l]$, while the numbers of independent m-modes are only $(2l + 1)$. So, we came to the following conclusion: for any given multipole we have $(2l + 1)$ values for power spectrum (C_l). Thus, for "observable" (we mean the independent part) power spectrum one can define

$$C_l = \frac{1}{2l+1}\sum_m a^*_{lm}a_{lm}. \tag{1.28}$$

It is clear that large angular scales are related to small $l < 100$ multipoles. On the other hand as already mentioned in the previous section, the main contributor of large-scale CMB asymmetry (primary asymmetry) is Sachs-Wolfe effect, for which asymmetry is

$$(\frac{\Delta T}{T})_{SW} = v \times e|^e_o - \phi|^e_o + \frac{1}{2}\int_o^e h_{\nu\sigma,0}n^\nu n^\sigma d\xi, \tag{1.29}$$

where the first term is due to Doppler shifting, the second term is referred to gravitational redshifting due to potential perturbations and the last term is inducted by Integrated Sachs-Wolfe (ISW) effect. Corresponding power spectrum written as

$$(C(l))^{SW} \propto \frac{1}{l(l+1)}. \tag{1.30}$$

The major parts of ΔT pointed on the small multipoles are $l \simeq 0, 1, 2$. Here $l = 0$ corresponds to angle-independent case for ΔT. The $l = 1$ is dipole component, related to Doppler effect,

and the $l = 2$ is called the quadrupole, whose origin can be in the adiabatic perturbations[45]. The dipole anisotropy for non-perturbed CMB temperature, is caused not only by Doppler shifting at the early conditions, but also from our relative motion with respect of CMB. It is crucial parameter for our work, so let us consider dipole asymmetry in more details. If the speed of relative motion of observer with respect CMB is v, then the temperature is given by [46]

$$T(\theta) = T_0 \frac{(1-\beta^2)^{1/2}}{(1-\beta\cos\theta)}, \tag{1.31}$$

where θ is the angle between v and direction towards which one makes observations and $\beta = \mid \frac{\vec{v}}{c} \mid \ll 1$. So, we can expand $T(\theta)$ in Taylor series

$$\frac{\Delta T(\theta)}{T_0} \simeq \beta\cos\theta + \frac{\beta^2}{2}\cos 2\theta + O(\beta^3), \tag{1.32}$$

where β corresponds dipole moment and β^2-quadrupole moment. Since higher order terms of the series are small, we can ignore them and keep only the first term. Another form of Eq.(1.31), suggested by, [47] acceptable for galaxies is

$$\frac{\Delta T}{T} = 2\beta \sin i\tau, \tag{1.33}$$

where v is galactic rotational velocity, i is galaxy inclination angle and τ is the optical depth.

1.3.2 CMB data processing and analysis

In order to calculate CMB dipole asymmetry we need some techniques, which allow us to make maps from registered data set and compute CMB power spectrum. Here we shortly present the sequence of steps, thanks which we can achieve our goals. So, the main stages of CMB data processing are a) receiving and processing time -ordered data (TOD), b) CMB data pixelization and map making, c) component separation, d) power spectrum calculation.

In Fig.(1.1) a schematic view of these steps are given. The data registered by our instruments

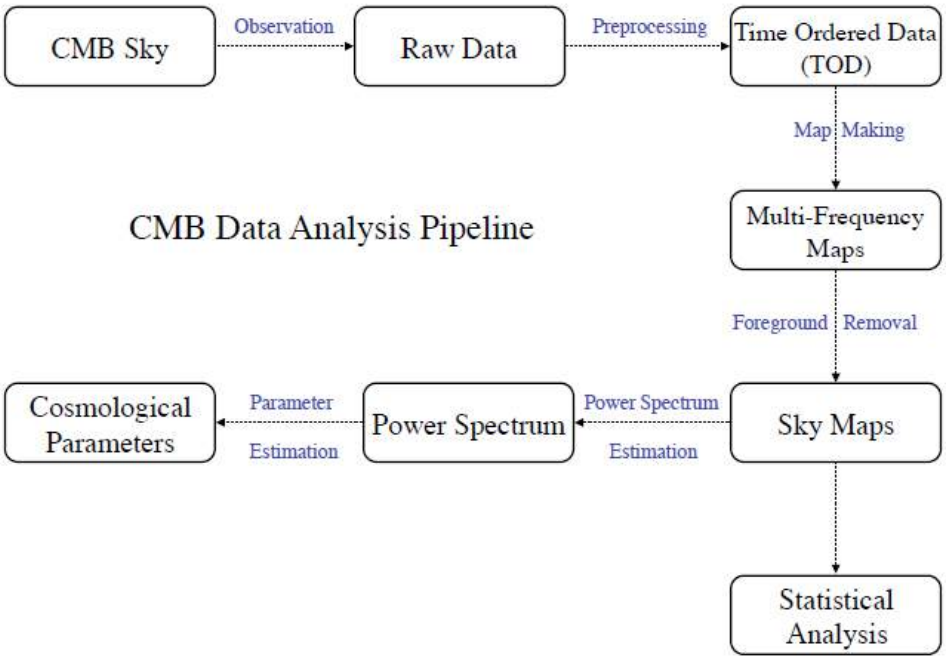

Figure 1.1: CMB data analysis diagram

(satellite or ground-based telescope) are so called the "raw" data, which contains many systematic errors, random fluctuations, instrumental noise and so on. After filtering all these effects, the raw data becomes to TOD data. Actually TOD is the list, which contains the measurable quantity for each observable point of sky (in our case it is temperature) and two pairs of coordinates (for example longitude (α) and latitude (β)). So, we have noise-cleaned values of temperature at any given point of the celestial sphere. Next step is map-making, aimed to compress large data set of TOD into more small data set, without losing any information. For this purpose we assume TOD value ($\mathbf{d}$) and given map's pixel ($\mathbf{m}$) are linearly related to each other:

$$\mathbf{d} = P\mathbf{m} + n, \tag{1.34}$$

where n is the random noise and P is $N_{\mathbf{d}} \times N_{\mathbf{m}}$ pointing matrix, which projects TOD ($\mathbf{d}$) into map ($\mathbf{m}$). So $N_{\mathbf{d}}$ is the number of observations (TOD) and $N_{\mathbf{m}}$ is the number of pixels of map. In addition, the shape of P matrix depends on the instrument's beam profile (via $\mathbf{m}$) and differs for different experiments. To find $\mathbf{m}$ we used the generalized least squares (GLS) method (because of linearity):

$$\chi^2 = n^T V n = (d^T - m^T P^T) V (d - mP), \tag{1.35}$$

where V is the noise inverse covariance matrix $v^{-1} = N = \langle nn^T \rangle$ of some symmetric matrix. So, map-making estimator ($\mathbf{k}$) is expressed by

$$k = (P^T V P)^{-1} P^T V d, \tag{1.36}$$

which solution by GLS method is

$$k = \Sigma^{-1} P^T N^{-1} d, \tag{1.37}$$

where $\Sigma = P^T N^{-1} P$. Because our instrument registers photons, coming not only from CMB, but also various types of radiation sources, it is critically important to extract CMB photons from others. There are two basic techniques for component separation. In general, the flux, which we receive from different sources are not affected (there is a superposition) from each other. Hence one can model received data as mixed linear combination of all possible sources (like superposition):

$$d_{ilm} = \sum_{k=1}^{N_c} A_{ik} s_{klm} + n_{ilm}, \tag{1.38}$$

where last term is noise component, A_{ik} is mixing matrix and s_{klm} contains CMB and foreground amplitudes. Meantime, (l, m) are spherical harmonic coefficients (see Eqs.(1.26-1.28)). There are two basic approaches of component separation that are parametric and

blind. In the first case one can fit foreground emission, which is mixed with CMB. For that purpose, we perform an estimation of mixing matrix in Eq.(1.38) and then we use an inversion of the Eq.(1.38) in order to recover foreground signal from s_{klm}. In the case of second approach by having some models for foreground components, one can focus on CMB component reconstruction (this is because we know spectrum of CMB radiation). However we will not deal with these methods, since we use the already component-separated data from *Planck* mission.

1.3.3 Sky pixelization

Accuracy of spherical harmonics integration on the sky (sphere) strongly depends on the selected pxelization technique. The simplest way of sky pixelization is the equal division of coordinate's pairs (θ, ϕ), which is called Equidistant Cylindrical Projection (ECP). It is useful, when one performs fast fourier transforms and significantly accelerated map-making process [48]. However, the disadvantage of ECP method is that the polar pixeles are small comparing to with equator's pixels, which affects completeness of the data. Another scheme suggested by Sloan Digital Sky Survey [49] named Hierarchical Triangular Mesh (HTM), which consists of 8 basis triangles, equally located along two hemispheres. Having equal areas, these basis pixels are able to be divided into four pixels and so on. COBE satellite uses the Quadrilateralized Sky Cube Projection, which is based on the rule of projecting cubes into spheres. Since its geometry does'n have azimuthal symmetry, the numerical computations of spherical harmonics require a lot of time. Beside these, there are numerous methods for sky pixelization. The most popular of which are the Icosahedron pixelizing by [50], the Igloo pixelization by [51], the Hierarchical Equal Area iso-Latitude Pixelization (HEALPix) method by [52], the Gauss–Legendre Sky Pixelization (GLESP) by [53]. The idea of last scheme is determination of pixelization algorithm based on the a_{lm} coefficients calculation method. In the next sections we use the HEALPiX scheme, so let us discuss the

details. According to HEALPiX scheme, in order to having powerful tool of pixelization, it is important that the given algorithm satisfy several conditions. Firstly, given scheme must be able to find the closest neighbor pixels, which is critical important for many computations. Namely if one analyze a parameter (pixel), whose value depends on the surrounding pixel's values, then hierarchical structure of HEALPiX allows to do it easy and fast. The second condition is equal areas of pixels partition. This feature of HEALPiX allows us to exclude the dependence of measured signal on the pixel's shape. For this reason the pixel size must be very small compared to instrument's resolution. Next feature of HEALPiX is iso-latitude distribution of discrete area elements on a sphere, which is aimed to perform very fast Legendre polynomials calculations. It is necessary when we are dealing with huge amount of data sets. In fact none of pixelization strategies, which are discussed above, have these three features. For example, Quadrilateralized Sky Cube Projection satisfies first and second conditions, but not the third. ECP does not satisfied the second condition (i.e. equal areas) and GLESP's geometry is not hierarchical. The situation is illustrated in Fig.(1.2), where all methods are presented together [52]. HEALPiX have 12 basis pixels, within three rings located along poles and equator. The next hierarchical level is formed from the previous by dividing each pixel of the previous level into four equal parts, as presented in Fig.(1.3). The resolution is controlled by N_{side} parameter, which is defined as the number of pixels obtained by previous structure (hierarchical level). So, the total number of pixels are $12N_{side}^2$, with equal areas $S = \frac{\pi}{3N_{side}^2}$. There are two numbering schemes for HEALPiX: ring and nested. For the ring indexation the numbering starts from north and reaches up to south pole. For nested scheme were use tree structures, within which it becomes easier to find neighbor pixels. By now we have all necessary tools for moving to *Planck* data analysis.

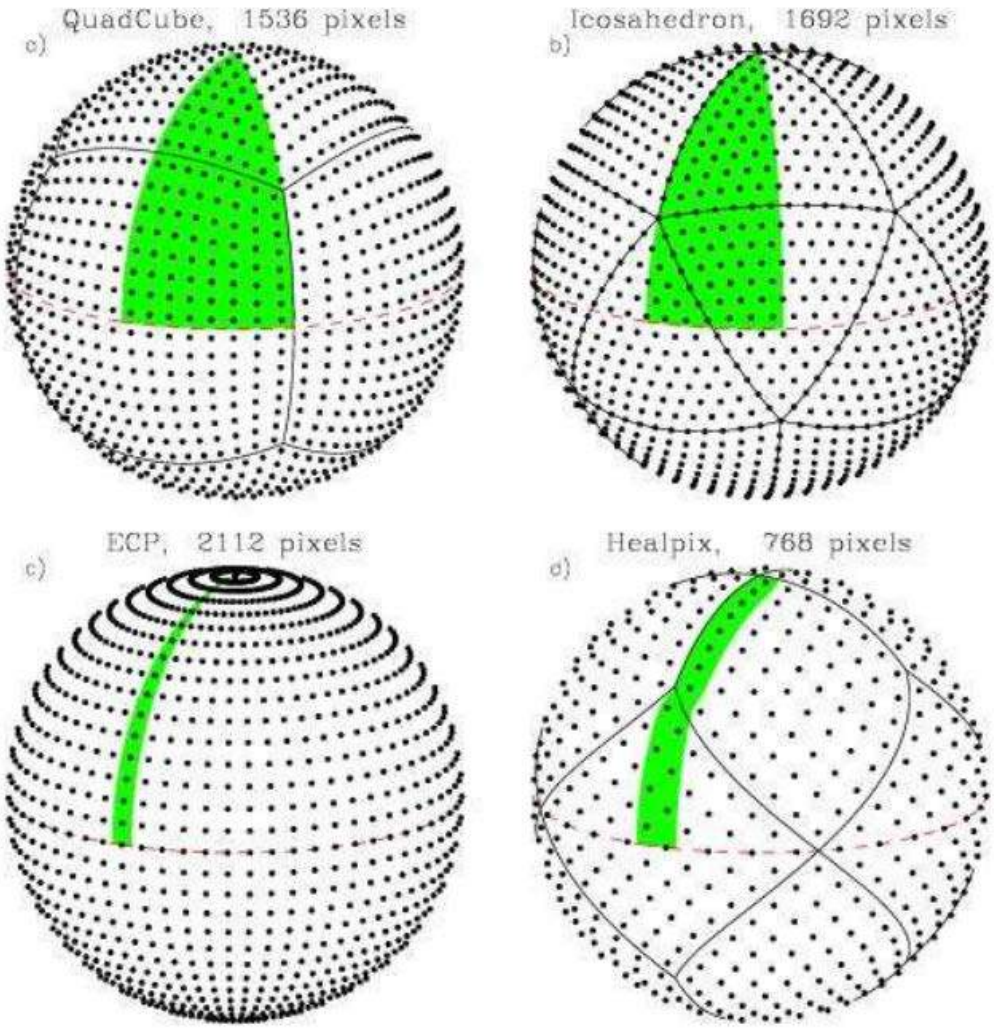

Figure 1.2: Comparison of iso-latitude structure with non iso-latitude structures by [52]. Green regions are given pixel, for which assumed performs Legendre polynomials calculations. From here the advantages of iso-latitude structure become clear(i.e. from number of pixels for different pixelization).

1.4 Analysis of PLANCK CMB maps

Planck mission has several advantages. For example it has three times higher resolution, which allows to measure large multipoles (l). It is also ten times sensitive, than previous generation's missions and cover 9 frequency bands. Planck has two instrumental tools for 9 frequencies: Low Frequency Instrument (LFI), with 30, 44, and 70 GHz and High Frequency Instrument (HFI) with 100, 143, 217, 353, 545, and 857 GHz. HFI consists of 48 bolometric detectors produced by JPL (Caltech), also its noise level is significantly low. In one hour

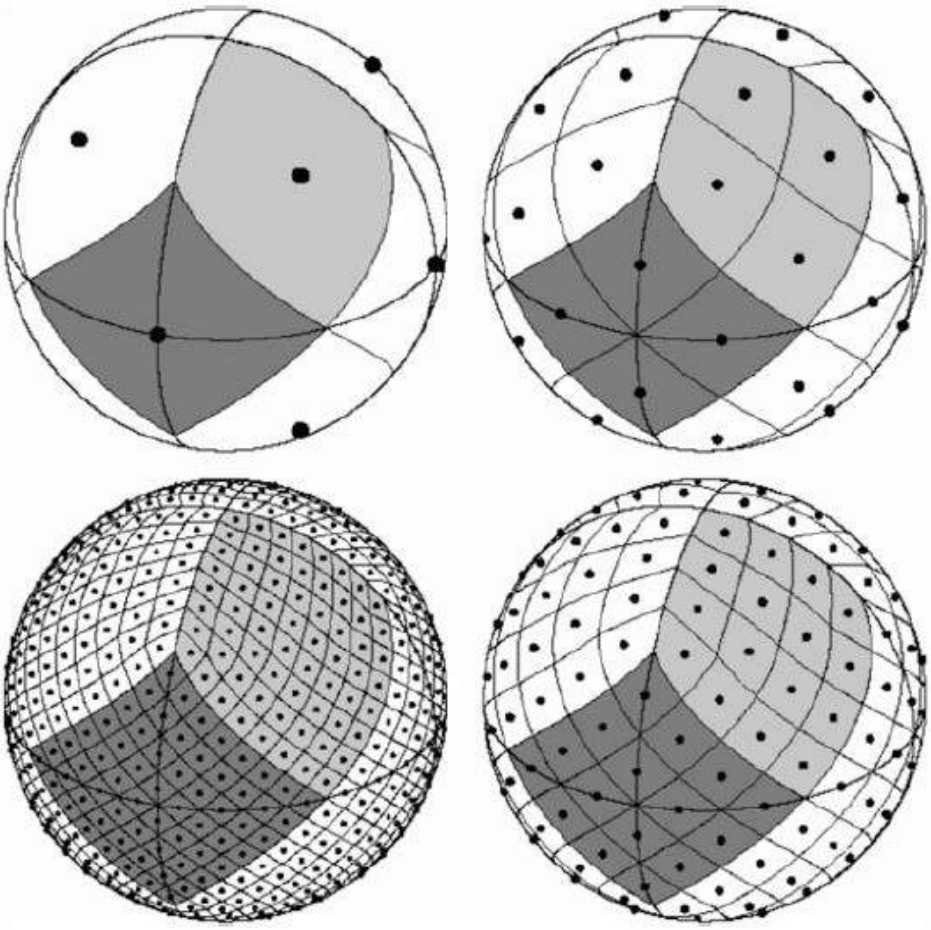

Figure 1.3: HEALPiX hierarchical levels formation from basis resolution($N_{side} = 12$) by [52]

Planck satellite spins with fixed (85^o) angle, during which instrument's beams cover nearly great circles in the sky. Then, every hour the rotation axis is changed by 2.5armin. As a result one can have multiple scanned sky, both for LFI and HFI instruments. A possible Doppler-inducted asymmetry were examined for M31 [56], M82 [57] and M81 [59] galaxies. Here we use Planck 2015 data [160] for the same purpose but only at three high frequencies 353, 545, 857 GHz and large galactocentric distances. Our data again has HELPiX nested ordering pixelization, but in this time the resolution $N_{side} = 2048$ is significantly higher, thanks to large number of pixels are available. Using the same geometry and calculation technique, which are described previous section we obtain CMB asymmetry values for M31 and M104 halos up to 100kpc, M81 and M82 halos up to 25kpc. Note, that M82 is satellite of

M81 and there distance is just 100kpc. Note, that the temperature asymmetry is significantly lower at high frequencies and it also decreases within very large radii.

1.5 Conclusion

We discussed the methods of CMB data analysis aimed to obtain the temperature asymmetry. Our analysis reveals the Doppler nature of this phenomenon. For that aim, the analysis involves both high and low frequencies in the *Planck* data, along with the high resolution, $N_{side} = 2048$ and of low "noise" instruments. Then, we will inquire into the possible emission mechanisms or components of interstellar medium (ISM) like dust, free-free, hydrogen clouds which can give contribution to CMB signal. Therefore one can combine these data with ISM components to extract an information about galactic halo's rotation or other parameters. In the next section, we will apply those methods for the analysis of M81 and M104 galaxies microwave data.

Chapter 2

Rotating baryonic dark halos

2.1 PLANCK data analysis for M81 galaxy

2.1.1 Introduction

Cosmic Microwave Background (CMB) data are mainly used with the primary aim to infer the values of the parameters of the cosmological standard model. In addition, CMB data also offer a unique opportunity to study the large-scale temperature asymmetries far beyond the size typically accessible with other tools toward nearby astronomical systems ((see, e.g.,[55], [54]). Here we continue the use of CMB data to map the dark halos of nearby galaxies, the latter often studied in most details on other bands or via other methods. Indeed, in the recent past we have analyzed *Planck* data toward four nearby galaxies with the main aim of testing if microwave data show a substantial temperature asymmetry of one side with respect to the other about the rotation axis of the galactic disk. We have considered, in particular: M31 galaxy and its halo [56], the active radio galaxy Centaurus A (Cen A) that is considered the closest AGN [57], M82, the largest galaxy in the M81 Group in the Ursa Major constellation [58], the M33 galaxy where we found a substantial temperature asymmetry with respect to its minor axis projected onto the sky plane, which extends up to about 3° from the galactic

center and correlates well with the HI velocity field at $21cm$, at least within about 0.5° [59]. We emphasize that the very fact that the detected temperature asymmetries are always almost frequency independent is a strong indication of an effect due to the galaxy rotation and remark the importance of the methodology proposed which, in spite of its simplicity, may allow one to consistently estimate the galaxy dynamical mass contained within a certain galactocentric distance. We have also shown that, in general, our method, can be applied to nearby nearly edge-on spirals and may be used to trace the halo bulk dynamics on rather large scales in a model-independent way. The present paper is a follow-up of the previous paper on the M82 galaxy [58] where a substantial North-South and East-West temperature asymmetry was found, extending up to about 1° from the M82 center. The main conclusion about the origin of the temperature asymmetry (almost frequency independent) was its link with a Doppler-induced effect regarding the line-of-sight dynamics on the real halo scale-invisible in other bands-the ejections from the galactic center or the tidal interaction of M82 with the M81 galaxy. Here, we consider again this issue from the point of view of the M81 galaxy, one of the last objects in the Local Group which can be studied by available *Planck* data.

2.1.2 Data analysis and results for M81 galaxy

M81, also known as Bode's galaxy (or NGC 3031), at $J2000$ coordinates $R.A.: 09^h55^m33.1730^s$, $Dec: +69^\circ 3' 55.061''$ (Galactic Longitude $l = 142.0918406^\circ$, Galactic Latitude $b = 40.9001409^\circ$) is a SA(s)ab type galaxy at a distance of $3.6Mpc$ from us [61]. We have used the publicly released *Planck* 2015 data [1] [62] in the bands at 70 GHz of the Low Frequency Instrument (LFI), and in the bands at 100 GHz, 143 GHz and 217 GHz of the High Frequency Instrument (HFI). We have also used the foreground-corrected SMICA band, which should display the lowest contamination by the galactic foregrounds. We notice here that *Planck*'s resolution is

[1] From the Planck Legacy Archive, http://pla.esac.esa.int.

$13.2^{'}$, $9.6^{'}$, $7.1^{'}$, and $5^{'}$ in terms of FHWM at 70, 100, 143 and 217 GHz bands, respectively, and frequency maps [63] are provided in CMB temperature at resolution corresponding to $N_{side} = 2048$ in HEALPix scheme [52]. The study of CMB asymmetry is organized in several stages. In what follows we consider them with more details.

We need to examine CMB temperature along different parts of M81 galaxy [24]. For this purpose, first fix the parameter of galaxy components (i.e. bulge, disk and halo). Due to the symmetry of our object, we were identify disk component as an ellipse and halo component like circle.

The apparent size of M81 is $0.7^{\circ}(26.9 \times 14.1 arcmin)^2$. Thus, by conisdering this fact, we can find other parameters of ellipse. The dimension of semi-major and semi-minor axes of the ellipse are equal to $26.90 arcmin$ and $14.1 arcmin$, correspondingly, while the inclination angle is 58°. Moreover, centers of both ellipse and circle are coincide with the center of the galaxy. Therefore the axes of ellipse and circle also must coincide. In this way one can divide the galaxy into different parts and estimate temperature difference between them. Meantime we can study both disk and halo components separately. Different cases of galaxy field division are illustrated in Fig.(2.1). For example, we can estimate temperature asymmetry measuring the difference a) and b) or c) and d) as shown below.

Next, we apply the above mentioned tools to find temperature asymmetry on three different galactocentric distances and three frequencies: 70, 100, 143 and 217 GHz. For this, the Planck field of the region of interest (we give in Fig.(2.2)) the map in the case of the 143 GHz band) has been divided into four quadrants A1, A2, A3 and A4. As detailed in the histograms in Figs. (2.3) and (2.5) we have considered the temperature asymmetry in three radial regions about the M81 center within 0.5° 1° and 1.5° (indicated as R0.50, R1.00 and R1.50, respectively). In Fig.(2.2) the optical extension of the M81 galaxy is shown, as indicated by the inner ellipse. Planck temperature field for four frequencies are

[2]During our analysis we are working with degrees and arcmins, in our case 1° is equal $62.78 kpc$.

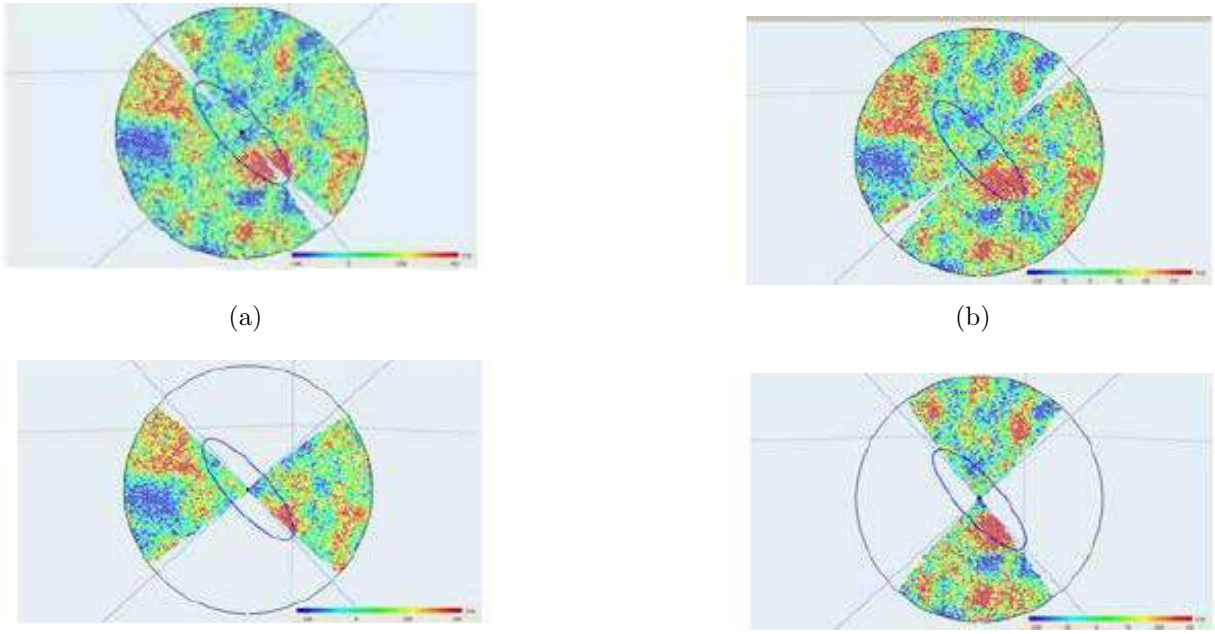

(a) (b)

(c) (d)

Figure 2.1: Two possible cases of M81 field division, through which is possible to make temperature asymmetry calculations. For study that, needs to obtain the temperature difference between any two equidistant regions (i. e. a) and b) or c) and d)).

shown in Fig.(2.4). As it was expected the temperature map for the same region of M81 are qualitatively different. In Fig.(2.3) we give the temperature asymmetry toward M81 in μK (with the standard errors) of the A1+A2 region (A12) with respect to the A3+A4 region (A34) in the five considered Planck bands within the three radial distances. In the bottom panel we give the same for the 360 control fields with the same geometry (shown in Fig.(2.2) equally spaced at one degree distance to each other in Galactic longitude and at the same latitude as M81. As one can see from Fig.(2.5) and as expected by considering the rotation direction of the M81 disk about its rotation axis, the A12 region always appears hotter than the A34 region by $32 - 44\mu K$ within 0.5°, by $28 - 40\mu K$ within 1° and by about $50 - 70\mu K$ within 1.5°. Note that the control fields show a much smaller temperature asymmetry of only a few μK and that the detected effect is practically the same in any of the five Planck's bands. We also note that the size of the virial radius of the M81 galaxy (equivalent to the R_{200} radius where the galaxy density is about 200 times larger than the critical density) can

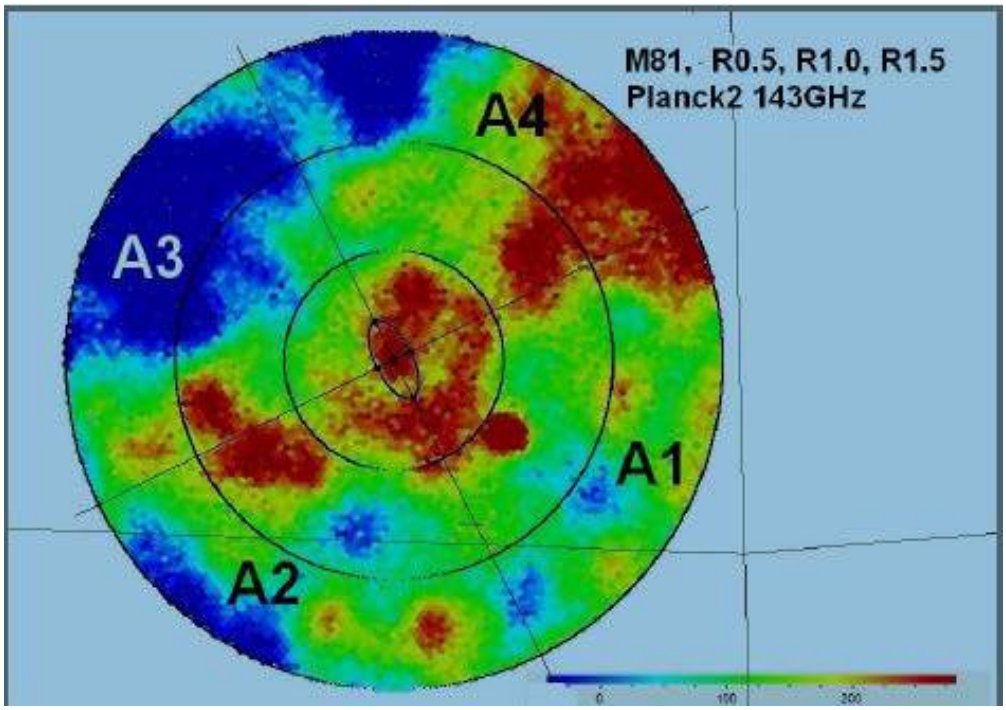

Figure 2.2: The Planck field toward the M81 galaxy in the 143 GHz band. The pixel color gives the temperature excess in μK with respect to the mean CMB temperature. The optical extension of the M81 galaxy is indicated by the inner ellipse with apparent dimensions of $26.9'$ and $14.1'$, respectively. The four quadrants A1, A2, A3 and A4 are used in the analysis. The thin dashed black line marks the Galactic latitude $b = 40^{\circ}$ North. We note that the M82 galaxy is clearly visible as the red spot in the A1 region at about $38'$ from the center of M81.

be estimated to be about 3.6° [64]. Although from the geometry and the direction rotation of the M81 disk, the expected temperature asymmetry was along the A12/A34 axis, we have also considered the temperature asymmetry toward M81 in the A14 region with respect to the A23 region and found an even more consistent asymmetry in all the considered Planck bands. This resembles what was already found towards the companion galaxy M82 [58]. In the present case the temperature asymmetry amounts to $40 - 80\mu K$ as implied by a prolate M81 halo rotation, while the control fields always show an asymmetry consistent to zero. As far as the foreground-corrected SMICA band is concerned, the temperature asymmetry is negligible within 0.5° (although one has to consider that the pixel number in this region is very low) and increases to large values within 1° and 1.5°. Also SMICA data show a clear and more consistent A14/A23 temperature asymmetry with values comparable with those in

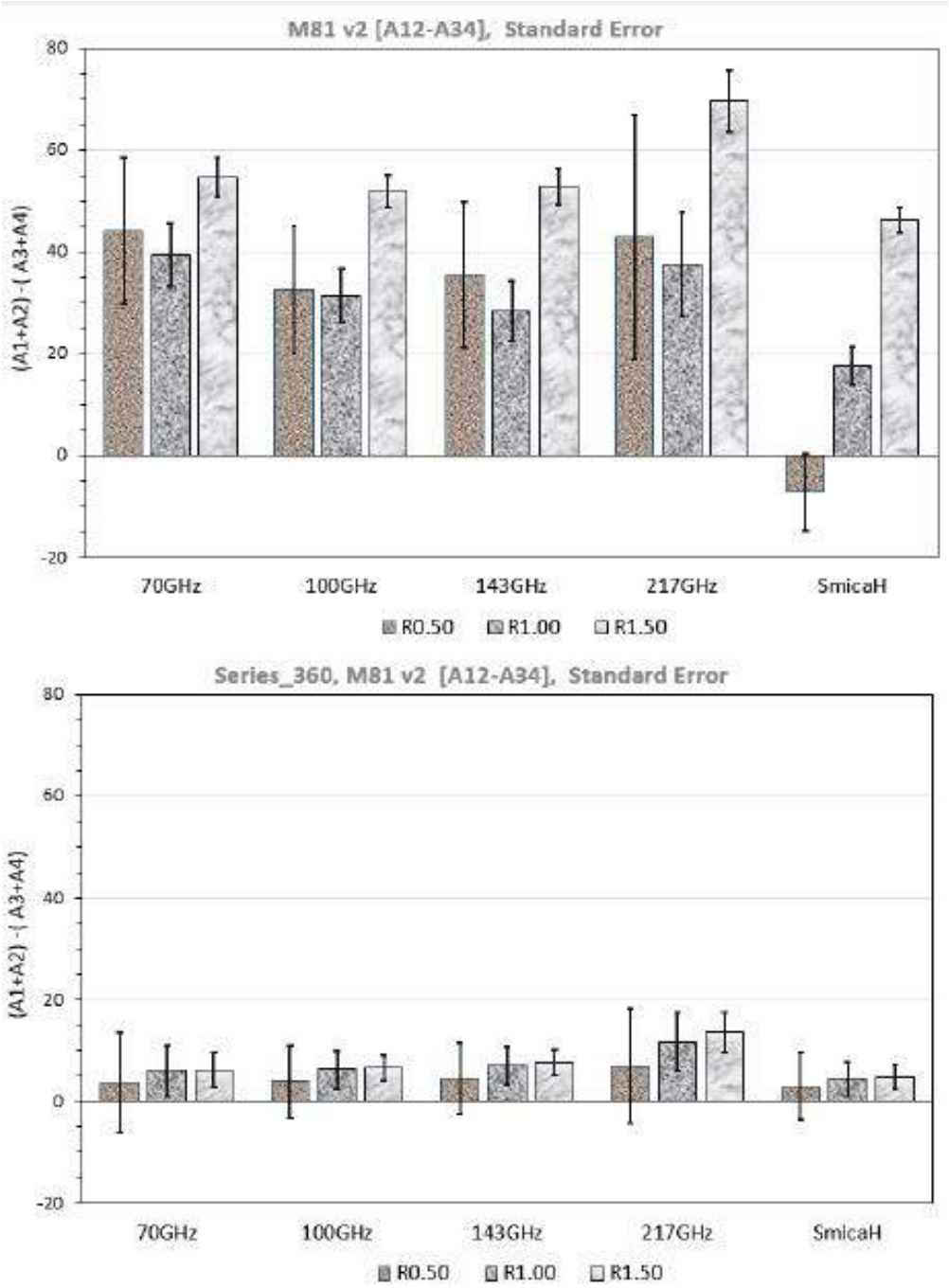

Figure 2.3: Upper panel: the temperature asymmetry toward M81 in μK (with the standard errors) of the A1+A2 region (indicated as A12) with respect to the A3+A4 region (A34) in the five considered Planck bands (see text for details) within three radial distances of $30^{'}$ (R0.50), $60^{'}$ (R1) and $90^{'}$ (R1.50). Bottom panel: the same for the 360 control fields with the same geometry (shown in Fig.(2.2)) equally spaced at one degree distance to each other in Galactic longitude and at the same latitude as M81.

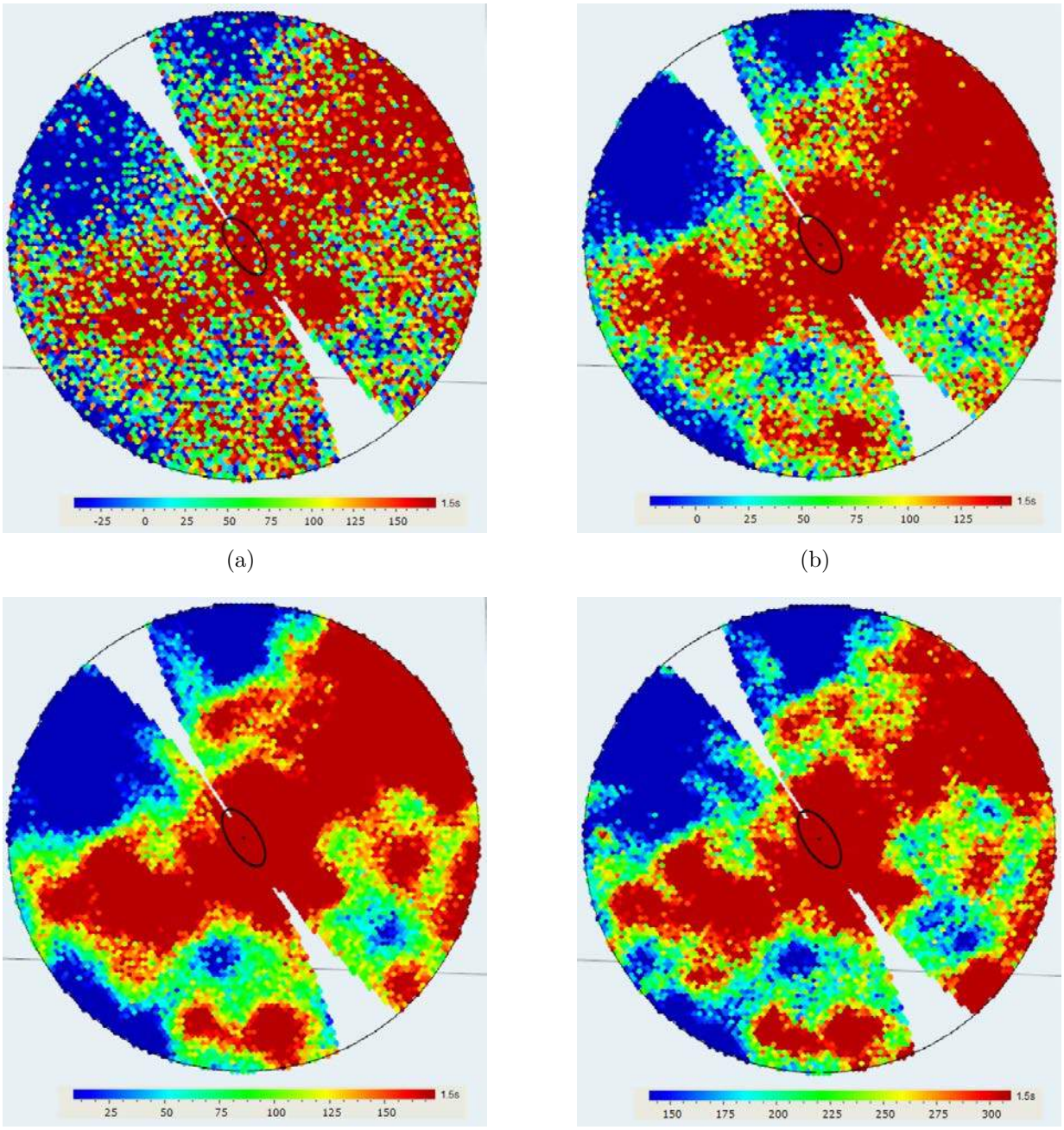

(a) (b)

(c) (d)

Figure 2.4: Upper panel:M81 region for 70 GHz (a) and 100 GHz (b) frequencies. Bottom panel: The same region for 143 GHz (c) and 217 GHz (d). Both cases with ellipse marked the disk of galaxy

the other bands within R1.00 and R1.50, although within 0.5° there may be a non-negligible foreground contamination in the other *Planck*'s bands.

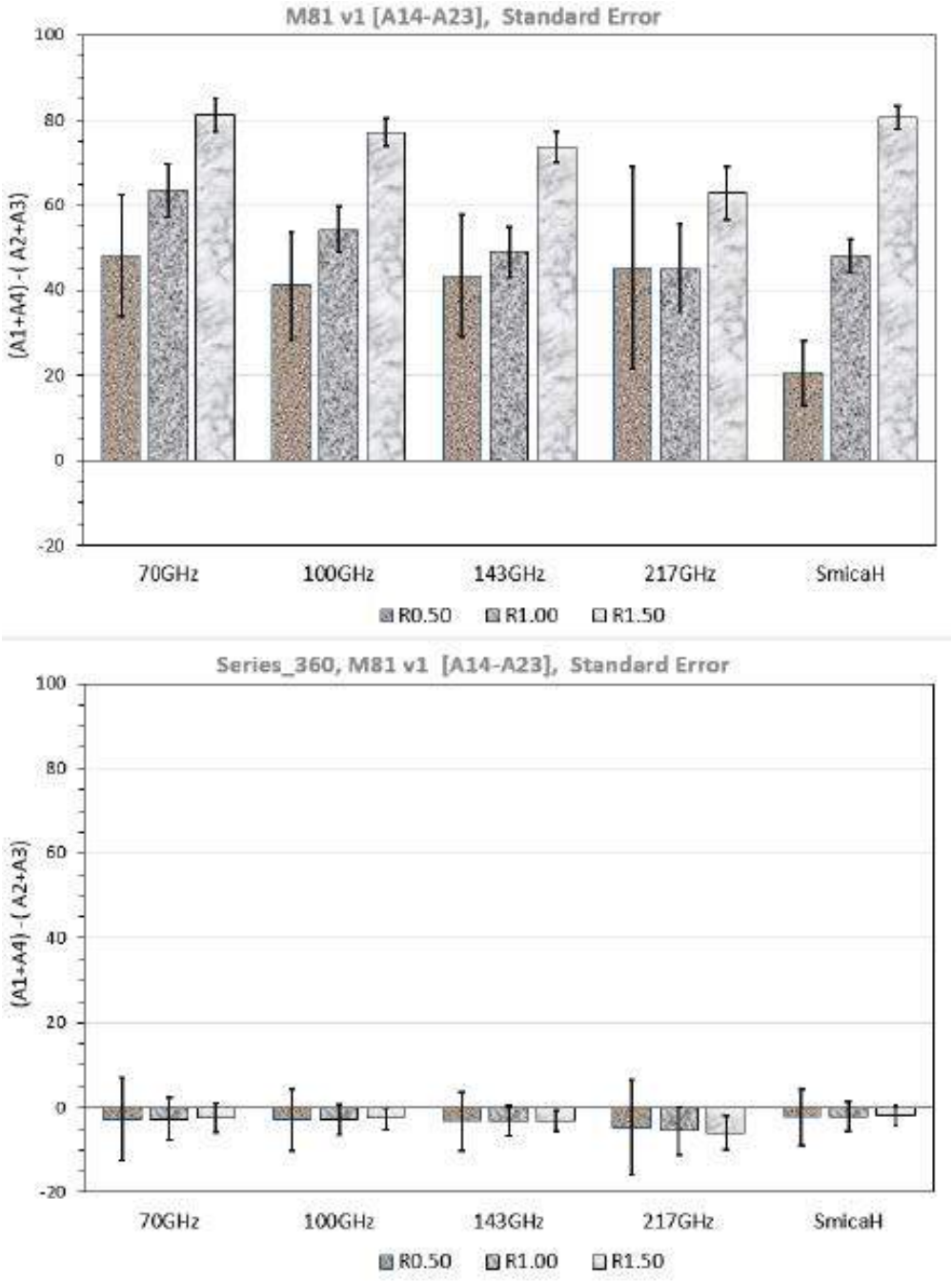

Figure 2.5: Upper panel: the temperature asymmetry toward M81 in μK (with the standard errors) of the A1+A4 region (A14) with respect to the A2+A3 region (A23) in the five considered Planck bands. Bottom panel: the same for the 360 control fields.

2.1.3 Conclusion

Similar to the case of the other galaxies of the Local Group considered previously and in particular toward M82, we found a consistent North-South and East-West temperature

asymmetry also toward the M81 galaxy, that reaches values up to about $80\mu K$ within 1.5° in all considered Planck bands. We believe, that the most plausible explanation relies in a Doppler-induced effect due to the spin of the M81 halo, possibly along an axis tilted (up to about 90°) with respect to the rotation axis of the M81 disk. In this case the temperature asymmetry can be estimated from the Eq.(1.33). In order to account for the detected temperature anisotropy, however, the M81 halo should be filled by a relatively large amount of gas (likely in the form of cold gas clouds), as in the models proposed, e.g., by [65], [66]. A viable explanation of the detected effect could be, in principle, also the rotational kinematic Sunyaev-Zel'dovich (rkSZ) effect, which is known to be active on galaxy cluster scales [67], [68]. Naturally, to be active, the rkSZ effect does require the presence of a conspicuous population of high energy electrons in the rotating M81 halo. By rescaling to the free electron density, temperature and size of the galaxy halos, the effect appears to be smaller by at least one order of magnitude (with respect to that in galaxy clusters), giving expected temperature asymmetries below a few μK. However, it might be that the temperature asymmetry derives from a multi component effect due to the presence of cold gas clouds together with a halo of hot and also, possibly, a warm component. Also other effects, such as the case that M81 is an interacting system with a rather recent merging event may induce an increase of the temperature asymmetry, as outlined in the following discussion. Many galaxies belong to multiple systems and constitute dynamically linked objects which are affected by their mutual gravitational interaction. An example of such systems is indeed constituted by the M81, M82 and NGC 3077 galaxies (the first two objects interacted about $200 Myrs$ ago, see e.g. [82], [69]). The radio images of the system, obtained for example by the VLA radio telescopes (see [70]), shows with strong evidence that the HI gas is not only associated with each galaxy but is also present around the galaxies and in the intergalactic space. Clear gaseous filaments are visible among the three major objects of the galaxy group (which is likely composed by at least six objects: M81, M82, NGC 3077, Holmberg IX, Arp's

Loop and NGC 2976 (see, e.g., [71], [72], [73]). This gas and the associated dust could give some contribution to the detected temperature asymmetry toward the M81 halo. In this respect we note that an enhancement of the emission arising from the rkSZ effect is expected to occur in recent merging events of rich galaxy clusters giving temperature asymmetries up to $146\mu K$ [68]. In the present case, the previous merging event between the M81 and M82 galaxies might have generated large scale turbulence and bulk motion with an increase of the free electron density and temperature which may amplify the rkSZ effect producing possibly temperature asymmetries up to $10 - 20\mu K$ (although a realistic estimate of the effect would require a detailed hydrodynamic modeling of the past merging event). [3]

Moreover, there could also be some contribution to the detected temperature asymmetry from high-latitude gas clouds in our Galaxy along the line of sight towards M81. In this respect we note that M81 is at about 40.9° North of the Galactic disk, where contamination from the Milky Way is expected to be low. However, interpretation of astronomical observations is often hampered by the lack of direct distance information. Indeed, it is often not easy to judge whether objects on the same line of sight are physically related or not. Since the discovery of the Arp's Loop [75] the nature of the interstellar clouds in this region has been debated; in particular whether they are related to the tidal arms around the galaxy triplet ([76], [77]) or to Galactic foreground cirrus ([78], [79]). Already [80] presented evidence showing that we are observing the M81 triplet through wide spread Galactic foreground cirrus clouds and [81] built large-scale HI, CO and dust maps which showed Galactic cirrus emission towards the M81 region with $N_H \simeq 1 - 2 \times 10^{20} cm^{-2}$. The technique used to distinguish between the emission from extragalactic or Galactic gas and dust relies on spectral measurements and on the identification of the line of sight velocities which are expected to be different in each case. Unfortunately, in the case of the M81 Group, this technique ap-

[3] We also mention that presence of baryonic jets from an ultra-luminous supersoft X-ray source discovered in the M81 galaxy, called ULS-1 (see [74] and references therein), may lead to an unexpected growth of the high-energy electrons and hot plasma populations in the M81 halo.

pears hardly applicable since the radial velocities of extragalactic and Galactic clouds share a similar LSR (local standard of rest) velocity range [82]. Several small-area molecular clouds (SAMS), i.e. tiny molecular clouds in a region where the shielding of the interstellar radiation field is too low (so that these clouds cannot survive for a long time) have been detected by [83] toward the M81 Group. More recently, data from the SPIRE instrument onboard Herschel ESA space observatory and MIPS onboard of Spitzer allowed the identification of several dust clouds north of the M81 galaxy with a total hydrogen column density in the range $1.5 - 5 \times 10^{20} cm^{-2}$ and dust temperatures between 13 and 17 K [82]. However, since there is no obvious difference among the individual clouds there was no way to distinguish between Galactic or extragalactic origin although it is likely that some of the IR emission both towards M81 and NGC 3077 is of Galactic origin. Temperature asymmetry studies in Planck data may be indicative of the bulk dynamics in the observed region provided that other Local (Galactic) contamination in the data is identified and subtracted. This is not always possible, as in the case of the M81 Group, and therefore it would be important to identify and study other examples of dust clouds where their origin, either Galactic or extragalactic, is not clear.[4] Incidentally, the region A1 within R0.50 has been studied by [85], who found evidence for the presence of an extended structural component beyond the M81 optical disk, with a much flatter surface brightness profile, which might contain $\simeq 10 - 15\%$ of the M81 total V-band luminosity. However, the lack of both a similar analysis in the other quadrants (and at larger distances from the M81 center) and the study of the gas/dust component associated to this evolved stellar population, hamper understanding whether this component may explain the observed temperature asymmetry toward the M81 halo.

Although the physical origin of the detected temperature asymmetry is not clearly identified at present, it appears obvious that the CMB asymmetry method is tracing the $M81$ halo and intergalactic bridges, not directly revealed in other bands and via conventional methods,

[4]One such example might be provided by the interacting system toward NGC 4435/4438 ([84]) where the SAMS found appear more consistent with Galactic cirrus clouds than with extragalactic molecular complexes.

based on stellar population studies, ISM, etc. In order to assess this issue, high-resolution and extended (up to $\simeq 1.5^{\circ}$) observations to infer the distribution of the cold, warm and hot gas components appears to be an urgent task to be performed. In this respect we emphasize that, in addition to radio observations at $21cm$ to map the HI component of the gas (integrated also by other techniques to study small-scale cold structures as done, e.g., through interstellar scintillations by [86] and to the X-ray band diffuse emission to infer the amount and distribution of the hot gas component, investigation of the warm gas component with the methodology employed, e.g., in [87] is extremely important. Given the serious quantitative disagreement between the microwave temperature asymmetry amplitude revealed for M81 and several other nearby galaxies and the rkSZ contributions there, the latter's alternative may be more exotic halo models (see, e.g., [88], [89], [90], [91]), a dilemma to be solved by future studies.

In conclusion, the available *Planck* data, by now, enabled one to trace, by this method, the haloes in the nearby edge-on spirals previously analyzed, while higher resolution data can be efficient for the studies of galaxies also outside the Local Group. This is particularly important in view of the next generation CMB experiments, such as LiteBird [92], CMB-S4 [93], CORE [94], DeepSpace[5], PIXIE [95] and Polarbear [131], which will attempt even more precise measurements of the CMB than available so far. Many of these experiments are designed to cover mainly the frequency range around 100 GHz where the relative intensity of the CMB is known to be highest and where one of the most dominant foreground components is dust emission (see, e.g., [96]). Understanding the properties of dust emission and distinguishing between Galactic foregrounds and extragalactic emission is an important premise for the optimized use of the next generation CMB experiments.

[5]See the DeepSpace website at http://deep-space.nbi.ku.dk.

2.2 PLANCK data analysis for M104

2.2.1 Introduction

As is well known, baryons contribute about 5% of our universe, but observations show that at least $40-50\%$ of the baryons in the local universe are undetected. The question therefore arises as to what form they take. Indeed, most of these baryons must be in a form that is difficult to detect. Cosmological simulations suggest that these baryons have been ejected from galaxies into the intergalactic medium and are present in the form of a warm-hot medium around galaxies ([97], [98], [99], [100]) at temperatures of about $10^5 - 10^7 K$. A non-negligible fraction of these baryons might also lie in a very cold form in clouds in the galactic halos. This possibility, previously suggested in [101], [66], was more recently directly evidenced by the detection of the so-called Herschel cold clouds (see [102] and references therein). Indeed, observations by Herschel-SPIRE towards the Large and Small Magellanic Clouds reveal the presence of thousands of gas clouds with temperatures of about $15K$, and it has been calculated that the full population of these clouds might constitute a non-negligible fraction of the Galactic halo dark matter.

We also remark here that galactic halos are on the one hand the least studied substructures of galaxies, and on the other are of particular importance for understanding large-scale structure formation. First, the parameters of galactic halos are sensitive to the non-Guassianity in the primordial cosmological perturbation spectrum ([103]), second, halos are probes for the mysterious nature of the dark matter([104], [105]), and third, halos determine the properties of the disks and the spheroidal structures of galaxies([106], [21]).

The primordial non-Gaussianity can be imprinted even in the profiles of the galactic halos ([107]), thus linking the latter to the inflationary phase of the Universe ([108]). Halo properties can thus be probes for the nature of perturbations; for example, even though we presently possess no observable evidence of non-adiabatic (iso-curvature) perturbations, we

have strong constraints on their possible resistance and it was shown that during re-ionization the iso-curvature modes are transferred to adiabatic ones ([109]).

In a series of papers we have used the cosmic microwave background (CMB) data, first that of WMAP and then that of *Planck*, to trace the halos of certain nearby galaxies ([54], [56], [57], [58], [59], [24]). The main aim was to test if the microwave data show a substantial temperature asymmetry of one side with respect to the other about the rotation axis of the galactic disks, as first suggested in [110] as due to the possible presence of a substantial amount of cold baryons in the galactic halos. Another motivation is that at the scales of galaxy clusters, the kinematic Sunyaev-Zeldovich (SZ) effect due to the cluster rotation is expected to induce temperature asymmetry in microwave data (see, e.g., [68], [111]). The same could in principle also happen for galaxies, provided they have a very hot gas halo component. Among the considered objects were the M31 galaxy, the active radio galaxy Centaurus A, M82, the largest galaxy in the M81 Group, the M33 galaxy, where we found a substantial temperature asymmetry with respect to its minor axis up to about 3° from the galactic center and which correlates well with the HI velocity field at $21cm$, at least within about 0.5°, and the M81 galaxy. In those galaxies we detected a clear temperature asymmetry of one side with respect to the other (as predicted for a Doppler shift) with $\frac{\Delta T}{T}$ values of typically about $(2-3)\times 10^{-5}$ and extending much further than the visible part of the galaxies (typically corresponding to peak values of $\Delta T \simeq 60-80\mu K$). Moreover, this temperature asymmetry is always almost frequency independent, which is an indication of an effect due to the galaxy rotation. It was thereby shown that our method can be applied to nearby edge-on spirals to trace the halo bulk dynamics on rather large scales in a model-independent way. In other words, the method is revealing the dark halos through the regular motion of either a cold gas component ([110]), for the possible modeling of the gas clouds and their distribution in galaxies we refer to, e.g., [65], [112], [113], [114], [115], or a hot ionized gas component (for a discussion of hot ionized gas through the thermal and

kinematic Sunyaev-Zeldovich effect we refer the reader to, e.g., [116]).

Along with the studies of the mentioned galaxies, we note that other galaxies, namely M63, M64, M65, and M66, analyzed in a similar manner, either do not show any significant microwave temperature asymmetry (for the first three galaxies) or the apparent asymmetry is frequency dependent (the M66 galaxy), and therefore has to be attributed, in this specific case at least, to a non-Doppler type signature ([24]).

Here we continue those studies on the microwave mapping of dark halos, analyzing the Planck data on a nearly edge-on Sa type spiral galaxy M104 known by its remarkable internal dynamics (see, e.g., [117]), and draw some conclusions on the baryonic dark matter content of its halo. The outline of the paper is the following: after a short presentation of the M104 galaxy, the analysis of *Planck* data is discussed in Section 2, while in Section 3 we present our main conclusions.

2.2.2 The M104 Sombrero galaxy

The galaxy M104, also known as the Sombrero galaxy (or NGC 4594), is a majestic galaxy located in the Virgo constellation at a distance of about $9.55Mpc$ from Earth (see Fig.(2.6) for a view in the optical band). The luminous bulge and the prominent dust lane give this galaxy its name. This dust lane is the site of star formation in the galaxy and a rich system of globular clusters (GCs) characterize the M104 halo. The estimated number of these GCs is about 2×10^3, about ten times larger than the number of GCs in the Milky Way. It is the brightest nearby spiral galaxy and is inclined at an angle of only about 7° to our line of sight and appears edge-on (its inclination angle is therefore $i = 83^{\circ}$). It is visible with binoculars and small telescopes, but only appears as a small patch of light. The large bulge of the Sombrero galaxy and the super-massive black hole at its core make it a popular target for study. The galaxy, at coordinates $RA : 12^h39^m59.4^s$, $Dec : -11^{\circ}39'23''$ (the galactic coordinates are $l = 298.46055^{\circ}$ and $b = 51.14929^{\circ}$), has major and minor diameters of about

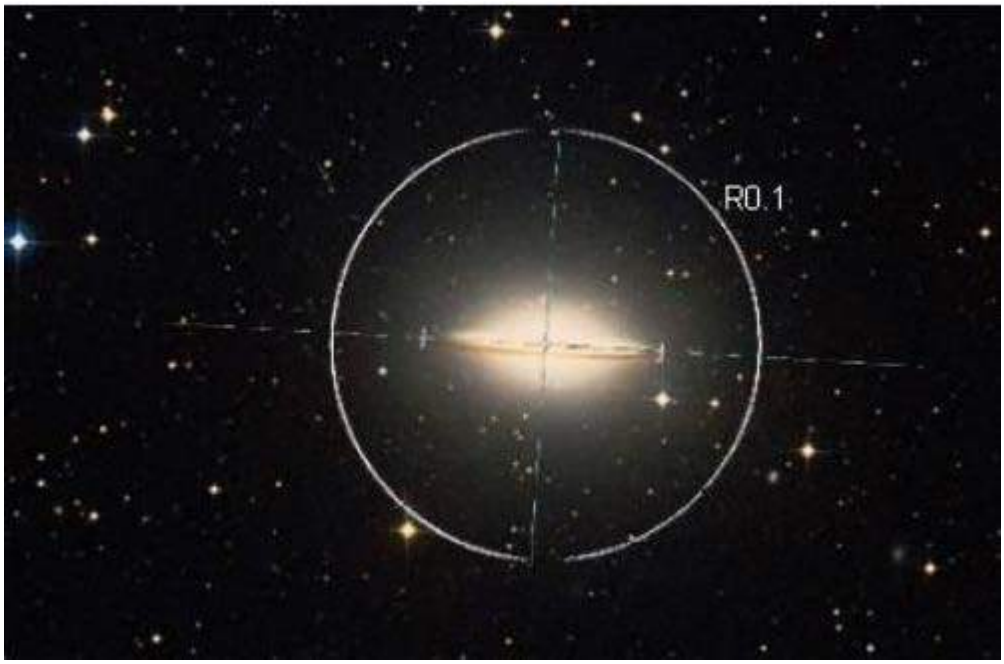

Figure 2.6: Sombrero galaxy in the visible band. The white circle traces the distance of 0.1° around the galaxy center at coordinates $RA: 12^h39^m59.4^s$, $Dec: -11^{\circ}39'23''$.

$8.6'$ and $4.2'$, corresponding to about $24kpc$ and $9.7kpc$, respectively (at the M104 distance $1'$ corresponds to about $2.78kpc$ and 1° to about $167kpc$). The galaxy has a visible mass of about $(22 \pm 3.2) \times 10^{10} M_{\odot}$ ([118]) and its center is thought to be home to a supermassive black hole.

Following the same procedures described in our previous papers we used the publicly released *Planck* 2015 data[6]([119])) in the 70 GHz bands of the Low-Frequency Instrument (LFI), and in the bands at 100 GHz, 143 GHz, and217 GHz of the High- Frequency Instrument (HFI). We also used the foreground-corrected SMICA map (indicated as SmicaH), which should display the lowest contamination by the galactic foreground. We notice here that the resolution of Planck is $13.2'$, $9.6'$, $7.1'$ and $5'$ in terms of FHWM (full width at half maximum) at 70, 100, 143, and 217 GHz bands, respectively, and the frequency maps by [120] are provided in CMB temperature at a resolution corresponding to $N_{side} = 2048$ in the HEALPix scheme ([52]). We also note that in the CMB maps we consider, the monopole

[6]From the Planck Legacy Archive, http://pla.esac.esa.int.

and dipole contributions have been removed. In Fig.(2.7) the Sombrero galaxy in the 143 GHz Planck band is shown. The optical extension of the M104 galaxy is shown, as indicated

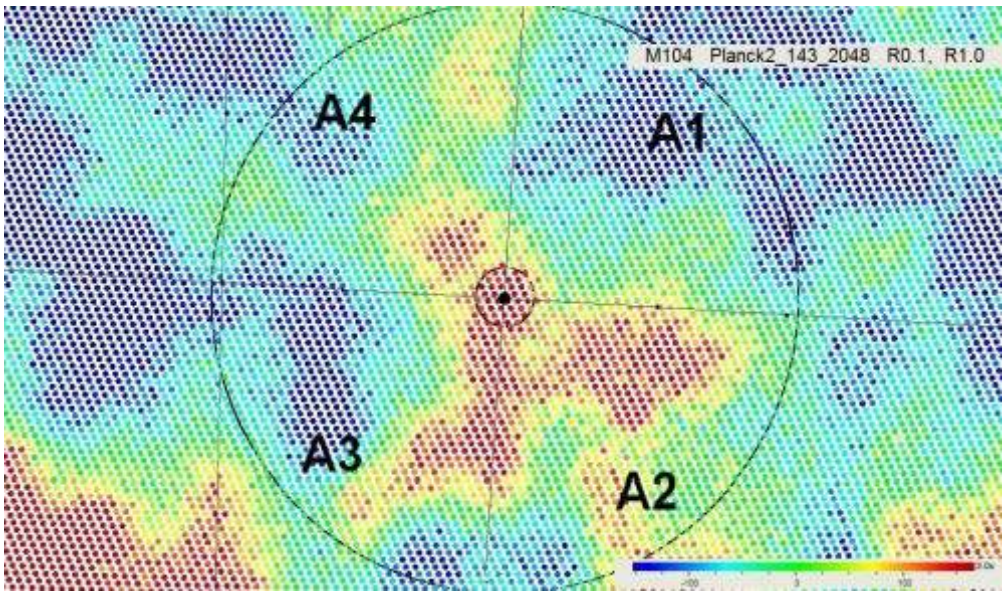

Figure 2.7: Sombrero galaxy in the 143 GHz Planck band. The inner and outer circles mark the galactocentric distances of 0.1° and 1°, respectively.

by the inner ellipse. Spectroscopic observations in the optical band and radio observations at $21cm$ show that the galaxy disk has an asymptotic rotation velocity of $376 \pm 12 kms^{-1}$ ([121]). Also, the globular cluster system around the M104 galaxy shows a global rotation with an estimated speed of about $100 kms^{-1}$ ([122]), with the eastern part moving towards Earth. To study the CMB data toward the M104 galaxy in the simplest way, the Planck field of the region of interest has been divided into four quadrants: A1, A2, A3, and A4 [26].

As detailed in the histograms in Figs.(2.8) and (2.9), we considered the temperature asymmetry in three radial regions about the M104 center within 0.2°, 0.4°, 0.6° and 1° (indicated as R0.2, R0.4, R0.6 and R1.0, respectively). In the upper panel of Fig.(2.8) we give the temperature asymmetry toward M104 in μK (with the standard errors) of the A1+A4 region with respect to the A2+A3 region in the four considered Planck bands within the four radial distances. In the bottom panel of the figure we give the same for the 360 control

fields with the same geometry (shown in Fig.(2.7)) equally spaced at one degree distance from each other in Galactic longitude and at the same latitude as M104. Here, we mention that we have intentionally avoided the use of CMB simulations to get the error bars. Indeed, simulations are mandatory when whole-sky CMB properties are studied (correlation functions, power spectra, etc.), while they could introduce additional uncertainties related to the modeling of foregrounds. As one can see from Fig.(2.8), the A1+A4 region always appears hotter than the A2+A3 region, and the temperature asymmetry increases with increasing galactocentric radius from about $25\mu K$ (within 0.2°) to a maximum value of about $65\mu K$ (within 0.6°). We note that $SMICA_H$ data show a similar trend. In the lower panel of Fig.(2.8), the 360 control fields show a temperature asymmetry consistent with zero in all Planck bands.

In Fig.(2.9) we show the second considered variant, namely the temperature asymmetry in the four considered Planck bands of the $A3 + A4$ region with respect to the $A1 + A2$ one. As one can see by comparing the upper and lower panels of Fig.(2.9), the temperature asymmetry now has a more complicated pattern; it is almost consistent with zero within 0.4° in the 70 GHz, 100 GHz, and 143 GHz bands, while $SMICA_H$ data indicate that the $A1 + A2$ region is hotter than the $A3 + A4$ one. The $A3 + A4$ side of the external M104 halo instead seems to be hotter than the other region in all considered bands by about $10 - 20\mu K$. We also illustrate M104 temperature field at four different frequency bands: 70, 100, 143 GHz and $SMICA_H$ (see Fig.(2.10)).

We also considered available data of the GCs in the M104 galaxy. [123] searched for rotation of the globular cluster systems around the M104 galaxy by considering the line of sight velocity of 108 GCs and found no evidence for global rotation. As also noticed by these latter authors, the lack of rotation is certainly surprising because there is a rotation of $300 - 350 kms^{-1}$ in the stellar and gas disk and, moreover, cosmological simulations of galaxy formation predict a significant amount of angular momentum in early-type galaxies.

In this respect, we note that most of the GCs towards M104 are detected relatively near to the galactic center. If one considers the 43 GCs with galactocentric distance larger than $5^{'}$ one finds a non-negligible rotation with the 95% upper limit on the rotation velocity of $250 kms^{-1}$ and a GC velocity dispersion (σ) of about $155 kms^{-1}$. Therefore, the obtained 95% upper limit on the value of $(\frac{v}{\sigma})$ is about 1.6. To further strengthen this discussion, in Fig.(2.11) we show the position of the eight outermost GCs (see [123] for details).

Unfortunately, these GCs reside in the A3 and A4 regions in Fig.(2.7), and therefore they can be used at most to probe the north–south asymmetry (as in the Variant 1), but not the east–west asymmetry. We obtain that the average line-of-sight velocity of the four GCs in the A3 region ($< v_r > \simeq 947 kms^{-1}$) is similar to that of the four GCs in the A4 region ($< v_r > \simeq 972 kms^{-1}$), also consistent with the observed recession velocity of the M104 galaxy of about $1024 kms^{-1}$. We note here that the two GCs with highest and lowest radial velocity are GC2200 in the A4 region and GC682 in the A3 region. These two globular clusters show a remarkable rotation about the M104 center since the first one is moving with line-of-sight velocity $< v_r > \simeq 1524 kms^{-1}$ while GC682 is moving towards Earth with $< v_r > \simeq 681 kms^{-1}$, thus with a relative velocity of $\simeq 343 kms^{-1}$ towards the observer. There is no doubt that an enlarged sample of GCs in the M104 galaxy at galactocentric distances larger than 0.4° could greatly help to probe the rotation of the Sombrero galaxy halo.

The detected temperature structure observed in the Planck microwave bands towards M104 may indicate the absence of a regular bulk motion at various scales and complicated internal dynamics. Indeed, the presence of an internal disk and an external ellipsoid has been suggested to explain the complex dynamics of the M104 galaxy. We would like to emphasize that our methodology to study the temperature asymmetry towards a given target aims to be maximally model-independent and, in particular, independent of the precise knowledge of the spectrum emitted in the considered regions (due to molecular clouds or to other

mechanisms such as the kinematic Sunyaev-Zeldovich effect or synchrotron emission, etc.). The temperature asymmetry signal we detect is practically frequency independent [7], which is a clear signature of the Doppler effect. In fact, we find that, in the case of the first Variant, the probability that the detected signal in each of the four considered rings is due to a random fluctuation of the CMB signal is 0.30, 0.31, 0.11, 0.26, respectively, which yield, assuming independent probabilities, a cumulative probability of about 1.8×10^{-3}, that is less than 0.2%, while for Variant 2, where the situation is less regular, the chance probability yields 3.1×10^{-2}.

Before closing this section, we also note that the simple Doppler nature of the temperature asymmetry can be influenced by several effects such as the peculiar motion of the halo clouds, the nonuniform spectrum of the clouds due to the radiation balance and radiative transfer details, and so on. However, obviously, at this stage, those are lower order effects with respect the global halo rotation. Moreover, since we consider M104 as being foreground to the CMB, we note that for the maps we study (with monopole and dipole extracted) the foregrounds could also be negative due to physical processes, for example, in the case of clouds, the particular molecular energy level transitions, metastable states, two-photon emission or absorption, and so on.

2.2.3 Conclusions

Similar to the case of other galaxies of the Local Group considered previously (in particular the galaxies M31, M82, M81, M33, and Cen A have been analyzed using *Planck* data and a temperature asymmetry ΔT about $60 - 80\ \mu K$ of one side with respect to the other about the rotation axis of the galactic disks has been detected in all cases), we found a consistent north–south temperature asymmetry toward the M104 galaxy, that reaches values up to

[7] We note that the slight apparent anomalies at small radii, where error boxes are larger, are due to the low number of pixels.

about $65\mu K$ within 0.6° (about $100kpc$) in all considered *Planck* bands [8], and then starts to decrease. We mention that Chandra observations in the X-ray band of the M104 galaxy show the presence of a diffuse X-ray emission extending at least up to $30kpc$ from its center ([124]), together with hundreds of point sources which are a mixture of objects in the M104 halo (mainly X-ray binaries) as well as background Quasars ([125]). However, the presence of this X-ray emitting hot gas cannot explain the temperature asymmetry detected in *Planck* data.

It is straightforward to show that if the cold-gas cloud model is at the origin of the detected temperature asymmetry (however, as anticipated in the previous section, other emission mechanisms may play a role in the detected signal), a lower limit to the M104 galaxy dynamical mass is given by

$$M_{dyn}(R) \simeq 700 M_{\odot} (\frac{R}{100kpc}) \frac{\Delta T^2_{\mu K}}{(\tau_{eff} sini)^2}, \tag{2.1}$$

where R is the considered galaxy halo radius in units of $100kpc$, ΔT is the measured temperature asymmetry (in μK) and τ_{eff} is the effective cloud optical depth (which depends on both the cloud filling factor and the averaged optical depth within a given Planck band. Expected values for τ_{eff} are about a few 10^{-3} ([126]), meaning that the M104 dynamical mass out to $\sim 100kpc$ is seen to be $M_{dyn} \simeq 3 \times 10^{10} M_{\odot}$, in agreement with other measurements (see, e.g., [118]). It is interesting to mention in this respect that this galactocentric distance appears close to the transonic point (at $\simeq 126kpc$), determined recently by [127] within the framework of the transonic outflow model in a dark matter halo applied to the Sombrero galaxy[9].

[8] We remark here that we consider maps of $N_{side} = 2048$ in the HEALPix scheme, which corresponds to a pixel size $\simeq 1.718'$ ([52], see also the web page https://irsa.ipac.caltech.edu/data/Planck/release1/ancillary-data), thus ensuring the pixel number statistics in the studied regions and the resulting error bars as in Figs. 2.8 and 2.9, and the discussion in Section 2.2.2)

[9] Indeed, outflow could be among the gas-heating mechanisms, together with shocks, turbulence, and galactic merging. The outflow itself could be uncorrelated to the rotation of the halo but the heated gas can contribute to the temperature asymmetry.

The detected temperature asymmetry is, as discussed in the previous section, almost frequency-independent and indicates that the M104 galaxy halo is rotating with respect to the major symmetry axis of the galaxy disk (Variant 1). However, the fact that a strong temperature asymmetry is detected also with respect to the minor symmetry axis of M104 (Variant 2), is a robust indication of a relatively complex geometry and rotation patterns. We note that that several different components have been shown to contribute to the observed galaxy kinematics (see, e.g.,[128]). These components have different rotational velocities and velocity dispersions. In addition, they cannot be described by a single Gaussian broadening function. This complex structure may explain the observations in the different Planck bands toward the Sombrero galaxy. As a matter of fact, the Sombrero galaxy exhibits the characteristics of both disk-like and elliptical galaxies. Recent observations by the Spitzer space telescope show that M104 is much more complex than previously thought and resembles a disk galaxy inside an elliptical one. We wish to emphasize here that the results in the present paper find strong support by Spitzer infrared vision which offers a different view of that emerging in visible light, with a glowing halo filled by old stars and a strong quantity of dust through which we observe a reddened star population. This implies that the M104 halo has the same size and mass as those of giant elliptical galaxies. The Sombrero galaxy resembles a giant elliptical that has swallowed a disk galaxy, but this is unlikely to have taken place since the process would have completely destroyed the galactic disk structure. Following [129], we propose that the M104 galactic structure is the result of a giant elliptical inundated by a huge amount of gas billions of years ago. This could explain the complex dynamical morphology of the Sombrero galaxy.

Before concluding this paper, we would like to make a general remark about the use of CMB data to map various galaxy halos. Indeed, the systematic study of the mean temperature asymmetry, applied here to the Sombrero galaxy, could become a conventional tool for studying and mapping the internal motions of not-too-distant galaxies (including their

halos) in the microwave band, in a complementary way with respect to other methods. As for the case of the Kolmogorov stochasticity parameter ([130]) and the Sunyaev-Zeldovich effect, software for an automated analysis, cross-correlating surveys in different bands with CMB data, may be developed. This is especially important in view of the next generation of CMB experiments, such as LiteBird ([92]), CMB-S4 ([93]), CORE (Cosmic Origins Explorer, [94]), DeepSpace [10], PIXIE (Cosmic Origins Explorer, [95]), and Polarbear ([131]), which will attempt to obtain measurements of the CMB that are even more precise than have been available so far and that may allow higher-resolution studies of the galaxies of the Local Group. Many of these experiments are designed to cover mainly the frequency range around 100 GHz where the relative intensity of the CMB is known to be highest and where one of the most dominant foreground components is dust emission (see, e.g., [132]). Understanding the properties of dust emission and distinguishing between Galactic foregrounds and extragalactic emission are important for the optimized use of the next-generation CMB experiments.

[10]See the DeepSpace website at http://deep-space.nbi.ku.dk.

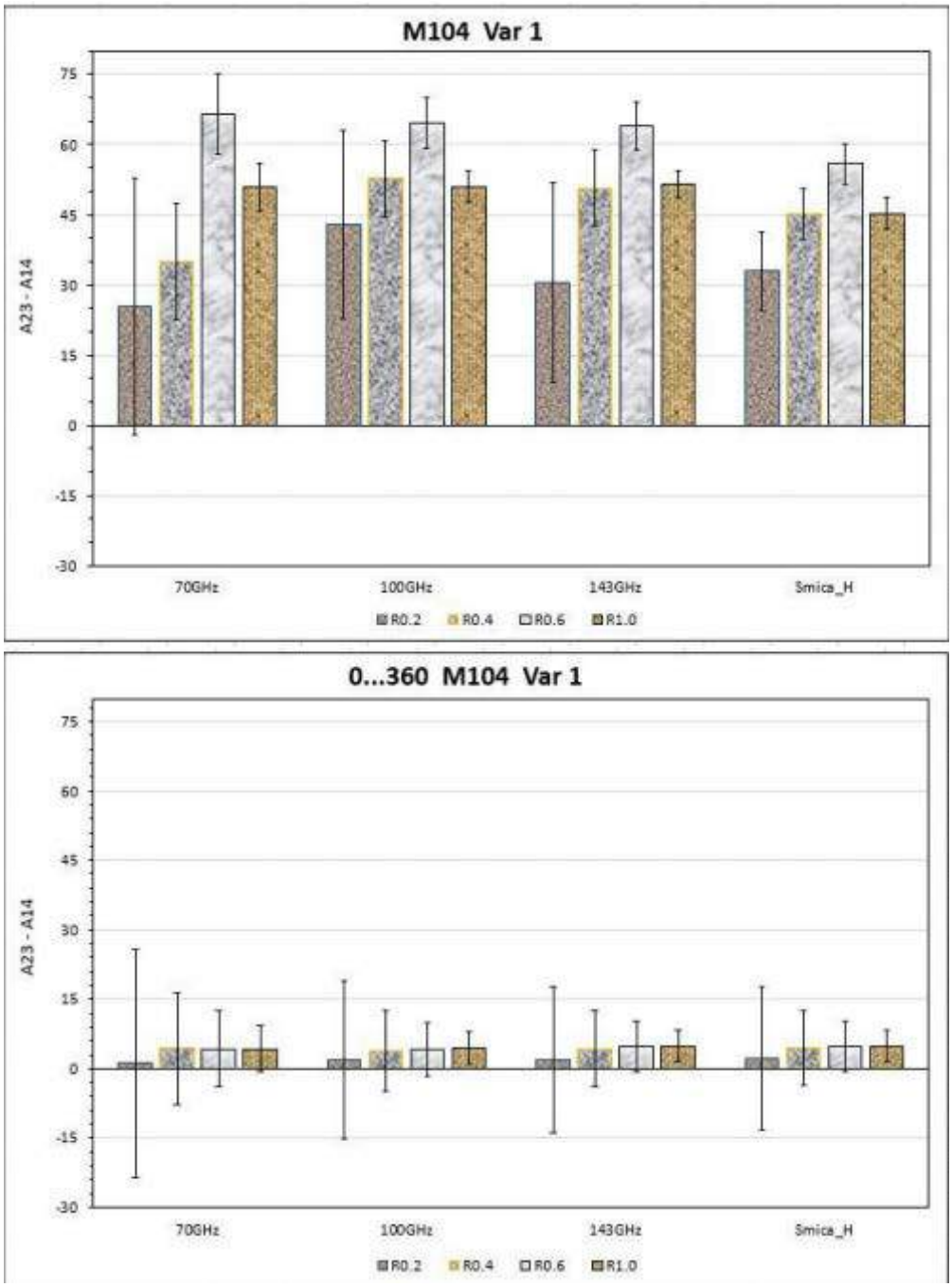

Figure 2.8: Temperature asymmetry towards (first panel) the M104 galaxy in μK (with the standard errors) of the Variant 1 (A2A3 - A1A4), in the four considered *Planck* bands (see text for details) within four radial distances of 0.2°(R0.2), 0.4°(R0.4), 0.6°(R0.6) and 1°(R=1.0); and (second panel) the same for the 360 control fields with the same geometry equally spaced at one degree distance from each other in Galactic longitude and at the same latitude as M104.

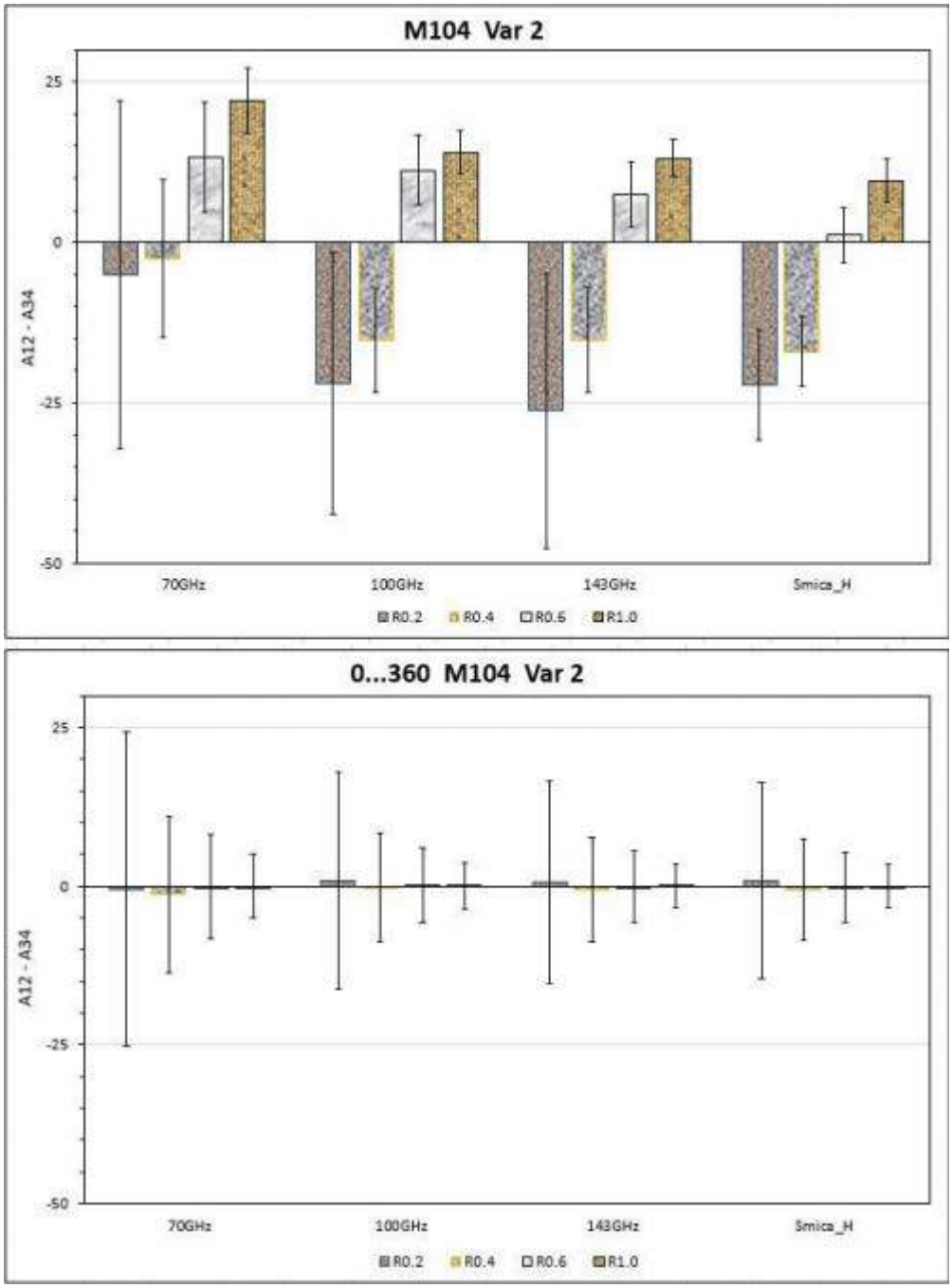

Figure 2.9: Temperature asymmetry towards (first panel) the M104 galaxy in μK (with the standard errors) of the Variant 2 (A1A2 - A3A4), in the four considered Planck bands (see text for details) within four radial distances of 0.2°(R0.2), 0.4°(R0.4), 0.6°(R0.6) and 1°(R=1.0); and (second panel) the same for the 360 control fields with the same geometry equally spaced at one degree distance from each other in Galactic longitude and at the same latitude as M104.

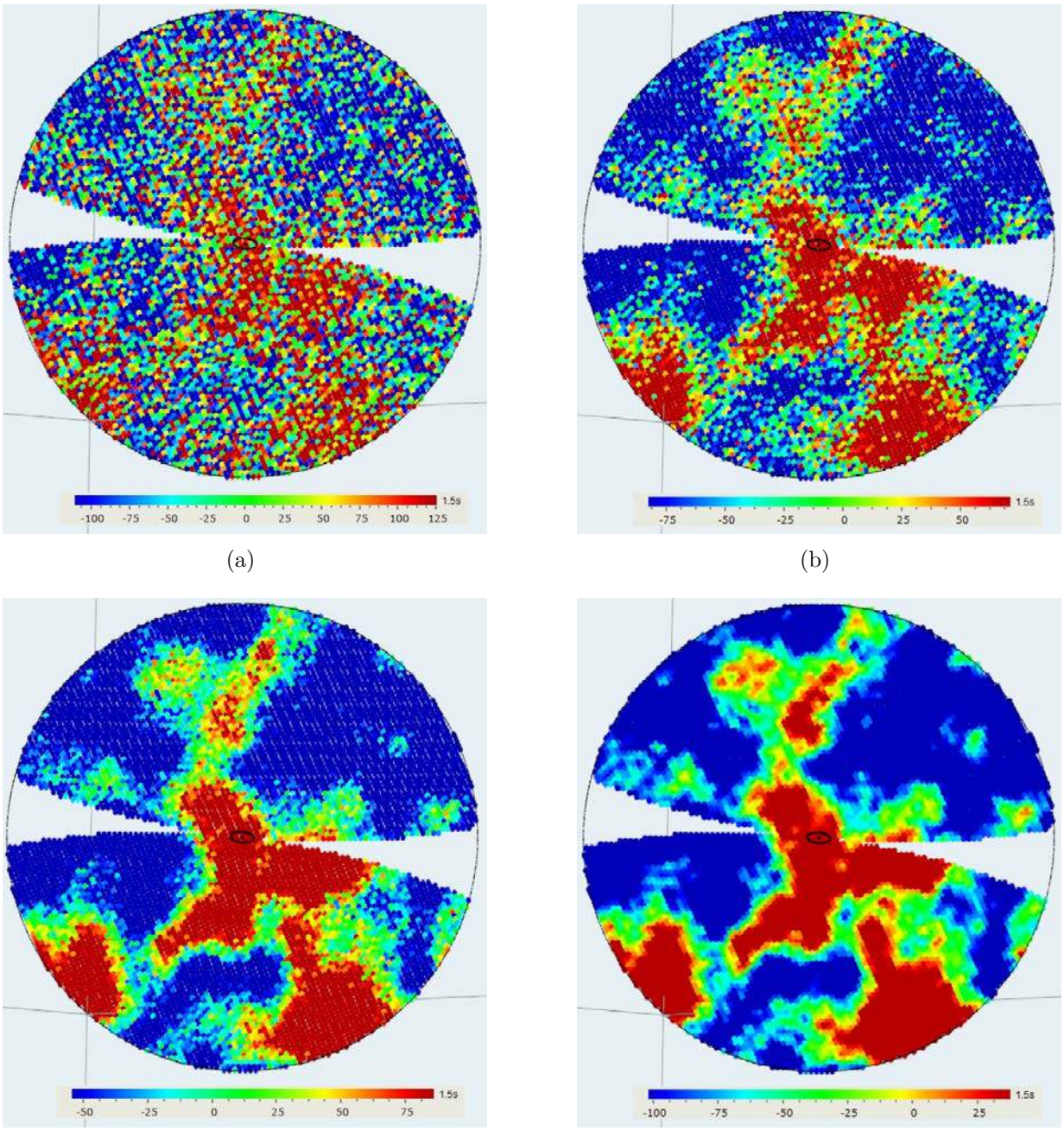

(a) (b)

(c) (d)

Figure 2.10: Upper panel: M104 region for 70 GHz (a) and 100 GHz (b) frequencies. Bottom panel: The same region for 143 GHz (c) and $SMICA_H$ (d).

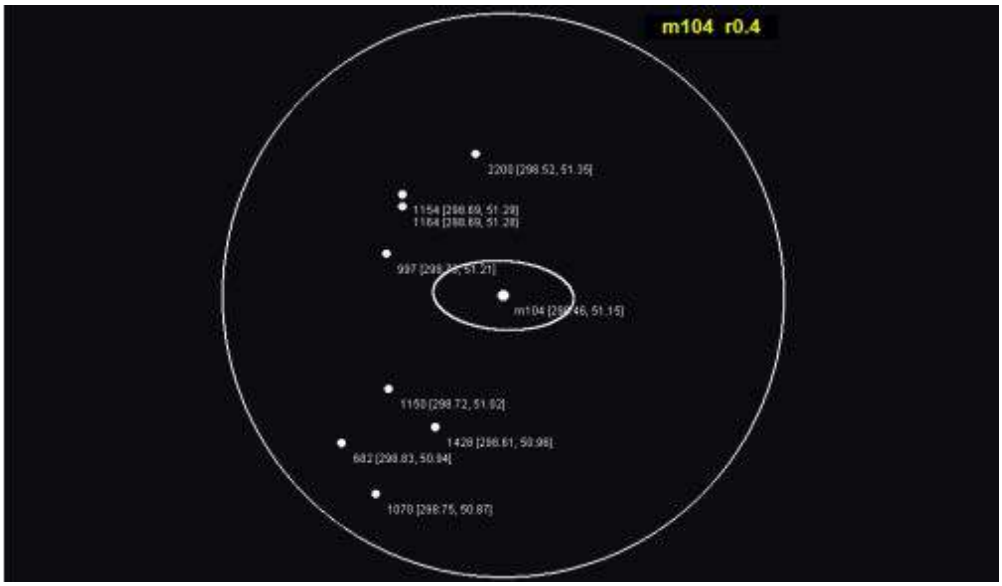

Figure 2.11: Plot of the position of the eight outermost globular clusters observed in the M104 galaxy (for details see [123]). The inner circle traces the visible part of the Sombrero galaxy while the outer circle is at a radius of 0.4°.

Chapter 3

Dark halo models and Cosmic Microwave Background

3.1 Introduction

3.2 On the structure of galactic halos and the microwave temperature maps

3.2.1 Introduction

The importance of studies of galactic halos is essentially determined by their key role in the deciphering of the nature of dark matter. The physical parameters of the halos not only determine the dynamics of galaxies including of the disks in spiral galaxies [133, 134], but also provide informative criteria to constrain the models of evolution of the cosmological perturbations [135].

Among the recent studies addressing the structure of galactic halos are those based on the analysis of the microwave temperature asymmetry of nearby galaxies using several frequency

bands of the *Planck* data [56, 57, 59, 58, 60]. Namely, for M31, then for several other Local Supercluster spiral edge-on galaxies it was shown that, the temperature asymmetry both in the disk and halo extends up to 130kpc. While the essentially frequency independent temperature asymmetry is indicating the Doppler nature of the effect, the Doppler induced anomaly itself can be due to different emission mechanisms of interstellar medium (ISM). One of the main components of ISM is the interstellar thermal dust, which emits especially at high frequencies. The possible contribution of the thermal dust in that effect is studied below using high frequency data of *Planck*. At the same time, dark matter configuration models have been actively developed. Among those there are Navarro-Frenk-White (NFW) [15], Moore [17], Burkert [16] models, which we will deal in our analysis. For M31, the dark halo profile, has been study in [136, 137, 138].

The present study concentrates on M31 galaxy, to probe the physical effects which can contribute to the microwave temperature asymmetry [27]. Various models have been proposed for interstellar dust, which fix the properties of dust particles, i.e. the chemical composition, dust grain size, distribution, etc. For our analysis we use the silicate-graphite-PAH model proposed in [139] (hereafter DL07), as well as *Planck*'s dust emission maps. According to *Planck* team [140, 141, 142], these models are described by single modified blackbody spectrum (MBB), from which we obtain radial variation of dust emission optical depth, using *Planck*'s dust emission map at three frequencies.

3.2.2 Interstellar thermal dust emission

The DL07 model: In this model, the dust is assumed to consist of a mixture of carbonaceous grains and amorphous silicate grains. In interstellar medium dust is heated from starlight and re-emits it in infrared or far-infrared wavelengths. DL07 model [139] has several parameters which completely define all the properties of dust grains. There are two types of dust grains: small grains ($a \leq 300$Å) and large grains ($a \approx 2200$Å). Small grains are warmer than big

grains. According to [143] major part of the emission comes from large grains, which is dominant part of all interstellar dust. DL07 model has several parameters, among those are the dust mass surface density Σ_{M_d}, dust optical extinction A_ν, starlight intensity U_{min}, the dust mass fraction in small PAH (Polycyclic Aromatic Hydrocarbon particles) grains q_{PAH}. Here the quantity q_{PAH} is defined as PAH's fraction of the total dust mass. PAHs are emitted at 3.3μm, 6.2μm, 7.7μm, 8.6μm, and 11.3μm wavelengths and we are not interested in their contribution, since we consider only three wavelengths (350μm, 550μm, 850μm). However, the exact modeling of PAHs is important for definition of the total dust mass [139].

The important parameter is the dust Spectral Energy Distribution (SED) shape as compared with the internal mechanism from which SED emerges. This is due to the fact that we need to calculate the radial variation of the dust emission optical depth.

Therefore, for our analysis we use only the dust mass surface density (or equivalent flux density from maps) to determine the dust velocity dispersion. As suggested by [143] there is a relationship between dust mass and optical depth

$$M_{dust} = \frac{\tau D^2 \Omega}{k}, \tag{3.1}$$

where τ is the optical depth, k is the dust mass absorption coefficient, which depends not only on given frequency, but also on chemical composition and structure of the dust grains; for example, at 353 GHz ($850\mu m$) $K_\nu = 0.43 \pm 0.04 cm^2 g^{-1}$ [144], D is the distance from the dust grains to observer, Ω is the solid angle. Optical depth (τ) shows intensity reduction of light emitted by dust grains and propagating over line-of-sight. The values of dust mass surface density, as well as of other parameters for DL07 model are publicly available in the *Planck* Legacy Archive and the parameters' processing is described in details in [151]. In Table (3.1) we present the values of dust mass surface density for M31 obtained based on the *Planck* maps.

The modified blackbody spectrum: As mentioned in the several *Planck* papers [140, 141,

142] the DL07 and GNILC-derived SEDs are compatible with MBB spectrum, which is obtained empirically from *Planck* observations of dust. For optically thin sources (like M31) the MBB function is as follows

$$S_{dust}(\nu) = 2h\frac{\nu^3}{c^2}\frac{1}{e^{\frac{h\nu}{kT_d}}-1}\tau(\frac{\nu}{\nu_0})^{\beta}, \tag{3.2}$$

where $S_{dust}(\nu)$ is the dust emission flux density, T_d is the dust temperature and β is the spectral index. Through spectral index we can identify the dust model. For DL07 model spectral index value of 2 for any radii is assumed. The dust temperature is changed in a more complex way. The *Planck* data indicates that there is an anti-correlation between T_d and β. T_d decreases, while β increases at large galactocentric distances. This anti-correlation has been examined in several papers [145, 146, 144]. The origin of anti-correlation is non-physical and is caused by instrumental noise or uncertainties at MBB spectrum fitting [147, 173]. However, as reported in [148], the spectral index for millimeter wavelengths is insensitive to temperature, while for FIR wavelengths the degeneracy is significant due to data uncertainties. The values of the dust temperature and spectral index are given in Table (3.1) and corresponding maps are shown in Fig.(3.1).

On the other hand, the temperature may change even for fixed values of spectral index. Therefore, we calculate the optical depth for two different cases:

1. Both T_d and β are constant at 19.635 K. Keeping fixed β, we vary the temperature. The data on temperature for different galactocentric distances are taken from *Planck* GNILC temperature maps.

2. Using GNILC maps for T_d and β we calculate the radial variation of the optical depth vs temperature and spectral index. We also cover optical depth, when $\beta = 2$, $T_d \neq$ const. These maps are available in *Planck* Legacy Archive, their processing is described in [149].

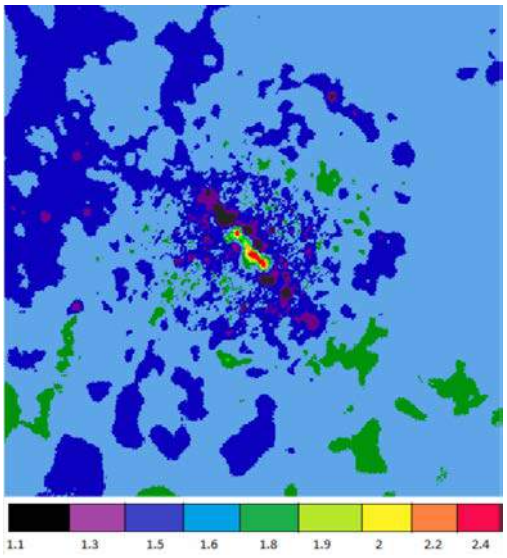

(a) M31 dust spectral index (β) map

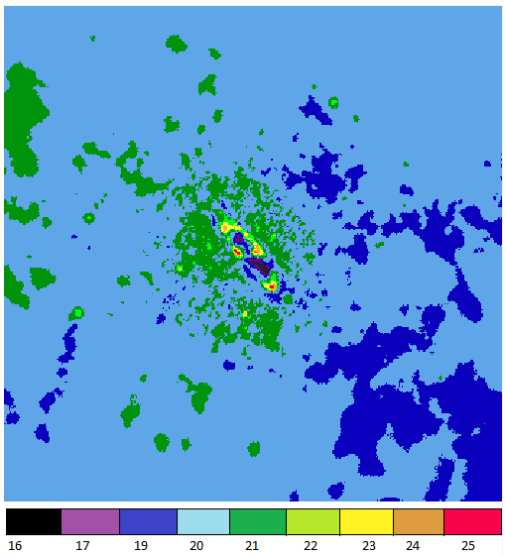

(b) M31 dust temperature(T) map

Figure 3.1: M31 spectral index (a) and temperature (b) maps from GNILC, with 10° width region. Each colored pixel gives the corresponding values of β and T. By the way β is a dimensionless quantity, while temperature given in K units.

Distance r (kpc)	Temperature $T_d(K)$	Spectral index β	Mass surface density $\frac{M_\odot}{kpc^2}(10^4)$
40	19.768	1.516	8.10
60	19.600	1.533	7.358
80	19.541	1.541	7.208
100	19.517	1.545	7.188

Table 3.1: Dust temperature, spectral index and mass surface density.

3.2.3 PLANCK maps vs halos

During the calculation of the optical depth we use several maps produced by Planck. These maps are publicly available in *Planck* Legacy Archive[1]. All maps, which we use during this study are given in Hierarchical Equal Area iso-Latitude Pixelization (HEALPix) with galactic coordinate system [52]. All maps have $N_{side} = 2048$ resolution, so the maps have $12\times2048\times2048 = 50331648$ pixels. For our analysis we extracted 2D projected maps centered on M31 ($l = 121.17^{\circ}$, $b = -21.57^{\circ}$), with 10° width region (see Fig.(3.2) for example).

[1]http://pla.esac.esa.int.

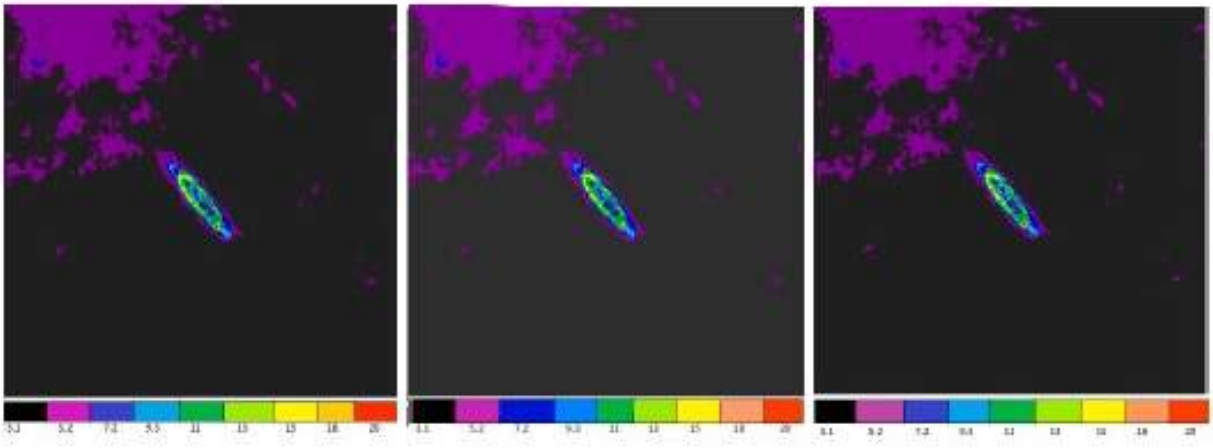

Figure 3.2: From left to right: Dust DL07 model flux density maps at 353 GHz, 545 GHz and 857 GHz frequencies, respectively. Note: The units of colored pixels given in MJy/sr.

DL07 and GNILC maps: The Generalized Needlet Internal Linear Combination (GNILC) method uses spatial information to separate dust emission and cosmic infrared background (CIB). The component-separation technique details are discussed in [149]. It is important to note, that GNILC maps are based on prior assumptions on the other foreground emissions (CMB, CIB, free-free, etc). In contrast, DL07 model-predicted fluxes are based on an individual dust model. Despite this, for galactic halo the MBB well describes both DL07 and GNILC methods. GNILC maps also have offsets at each frequencies ($0.556MJy/sr$ for 857 GHz, $0.335MJy/sr$ for 545 GHz and $0.124MJy/sr$ for 353 GHz), which we have taken into account. Besides the three frequency maps, we also use GNILC spectral index and temperature maps, which have been obtained using MBB fitting procedure (see Fig. (3.1)). For flux density $S_{dust}(\nu)$ values we use both DL07 (see Fig.(3.2)) and GNILC maps (see Fig.(3.3)) in three bandwidths.

In our calculations, we started from $35kpc$ distance from M31 center and substituted each pixel with the average value of the equidistant pixels.

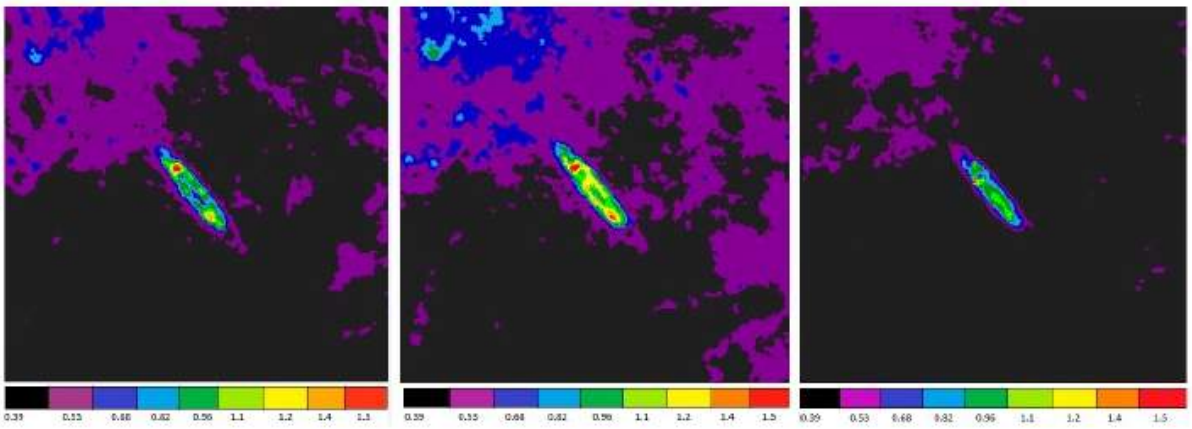

Figure 3.3: From left to right: Dust GNILC model flux density maps at 353 GHz, 545 GHz and 857 GHz frequencies, respectively. Note: The units of colored pixels given in MJy/sr

3.2.4 Dust emission optical depth

As mentioned above, we use MBB spectrum for obtaining the spatial variations of optical depth in M31 halo. We begin with DL07 model, where dust spectral index has fixed value of 2. Dust grain in thermal equilibrium with radiation field has uniform temperature distribution with average $19.635K$ (so here we consider this temperature value for M31 halo in the range of $30 - 100kpc$). Then we assume varying temperature (from GNILC map). The result of our calculations are given in the Table (3.2). The table shows, that the optical depth gradually decreases with increasing radius. In this case optical depth depends only on the dust emission flux density.

Next, we calculate optical depth using GNILC maps. In this case both spectral index and temperature are changed. There is anti-correlation between T_d and β reported by *Planck* collaboration [140, 141]. The spectral index of dust increases with radius, which means that dust emission properties depend on the temperature. Meantime, the heating rate of dust depends on the spectral index. The corresponding values of the optical depth in this case are given in Table (3.3) and Table (3.4). As in DL07, in this case also there is almost no temperature dependency of optical depth. Optical depth is only determined through spectral index and flux density (derived by GNILC method).

DL07 $\beta = 2$, $T = 19.635K$			
Distance r (kpc)	Optical depth τ_{857}	Optical depth τ_{545}	Optical depth τ_{353}
40	7.671×10^{-4}	1.616×10^{-3}	2.629×10^{-3}
60	6.122×10^{-4}	8.345×10^{-4}	1.465×10^{-3}
80	4.166×10^{-4}	4.314×10^{-4}	1.066×10^{-3}
100	3.456×10^{-4}	1.911×10^{-4}	1.508×10^{-4}
DL07 $\beta = 2$, $T \neq const$			
Distance r (kpc)	Optical depth τ_{857}	Optical depth τ_{545}	Optical depth τ_{353}
40	7.620×10^{-4}	1.605×10^{-3}	2.612×10^{-3}
60	6.133×10^{-4}	8.366×10^{-4}	1.468×10^{-3}
80	4.187×10^{-4}	4.337×10^{-4}	1.071×10^{-3}
100	3.480×10^{-4}	1.923×10^{-4}	1.517×10^{-4}

Table 3.2: The optical depth for DL07 model.

GNILC $\beta = 2$, $T \neq const$			
Distance r[kpc]	Optical depth τ_{857}	Optical depth τ_{545}	Optical depth τ_{353}
40	7.999×10^{-4}	1.482×10^{-3}	2.214×10^{-3}
60	6.421×10^{-4}	8.630×10^{-4}	1.208×10^{-3}
80	4.786×10^{-4}	3.177×10^{-4}	4.003×10^{-4}
100	3.587×10^{-4}	1.962×10^{-4}	1.083×10^{-4}

Table 3.3: The optical depth for GNILC model.

GNILC $\beta \neq const$, $T \neq const$			
Distance r (kpc)	Optical depth τ_{857}	Optical depth τ_{545}	Optical depth τ_{353}
40	2.100×10^{-2}	3.152×10^{-2}	3.771×10^{-2}
60	1.503×10^{-2}	1.648×10^{-2}	1.862×10^{-2}
80	1.084×10^{-2}	5.778×10^{-3}	5.989×10^{-3}
100	7.850×10^{-3}	3.493×10^{-3}	1.564×10^{-3}

Table 3.4: The optical depth for GNILC model.

3.2.5 Dark matter distribution profiles for M31

M31 is one of the most studied galaxy in the Local Group. Various authors have suggested different dark matter distribution profiles for M31 halo. Here, in this paper we use the

Navarro-Frenk-White (NFW) [15], Moore [17] and Burkert [16] models. The corresponding density and velocity distributions are presented below:

$$\rho_{NFW}(r) = \frac{\rho_c}{(\frac{r}{r_c})\Big(1+(\frac{r}{r_c})\Big)^2}, \tag{3.3}$$

$$V^2_{NFW}(r) = 4\pi G\rho_c \frac{r_c^3}{r}[ln(1+\frac{r}{r_c}) - \frac{\frac{r}{r_c}}{1+\frac{r}{r_c}}], \tag{3.4}$$

$$\rho_{Moore}(r) = \frac{\rho_c}{(\frac{r}{r_c})^{1.5}\Big[1+(\frac{r}{r_c})^{1.5}\Big]}, \tag{3.5}$$

$$V^2_{Moore}(r) = \frac{8}{3}\pi G\rho_c \frac{r_c^3}{r} ln\Big[1+(\frac{r}{r_c})^{1.5}\Big], \tag{3.6}$$

$$\rho_{Burkert}(r) = \frac{\rho_c}{\Big(1+\frac{r}{r_c}\Big)\Big[1+(\frac{r}{r_c})^2\Big]}, \tag{3.7}$$

$$V^2_{Burkert}(r) = 2\pi G\rho_c \frac{r_c^3}{r}\Big\{\Big[ln(1+\frac{r}{r_c})\sqrt{1+(\frac{r}{r_c})^2}\Big] - \arctan(\frac{r}{r_c})\Big\}, \tag{3.8}$$

where $r_c = \frac{r_{vir}}{r}$ and ρ_c are characteristic radius and density. The virial radius r_{vir} is defined as the radius at which the mean density is equal to the overdensity constant (Δ_{vir}) multiplied by the critical density of the universe.

The corresponding virial mass is defined as

$$M_{vir} = \frac{4\pi}{3}\Delta_{vir}\rho_{crit}R^3_{vir}. \tag{3.9}$$

Here ρ_c and r_c are free parameters, fixed by fitting procedure. In Table (3.5) the corresponding fitting values for these parameters are suggested by [138].

Profile	$\rho_c(M_\odot(pc)^{-3})$	$r_c(kpc)$	$M_{vir}(10^{11}M_\odot)$	$R_{vir}(kpc)$
NFW	$1.74 * 10^{-2}$	12.5	6.93	146.5
Moore	$2.05 * 10^{-3}$	25.0	7.38	149.6
Burkert	$5.72 * 10^{-2}$	6.86	5.16	132.8

Table 3.5: Best fit values of the DM profiles of [138].

On the other hand, we calculate the M31 halo rotational velocities using the Doppler effect induced temperature asymmetry formula for optically thin halo [47]

$$\frac{|\Delta T|}{T} = \frac{2vsini}{c}\tau. \tag{3.10}$$

Here the galaxy inclination angle is $i = 77^0$ and τ is the optical depth, which depends on the dust parameters and frequencies. T is the dust temperature, which is changed at large galactocentric distances (in GNILC model), and finally $|\Delta T|$ is the CMB temperature asymmetry in μK[2]. CMB temperature field at three frequencies are presented in the Fig.(3.4), where M31 galaxy's disk and halo components are clearly illustrated.

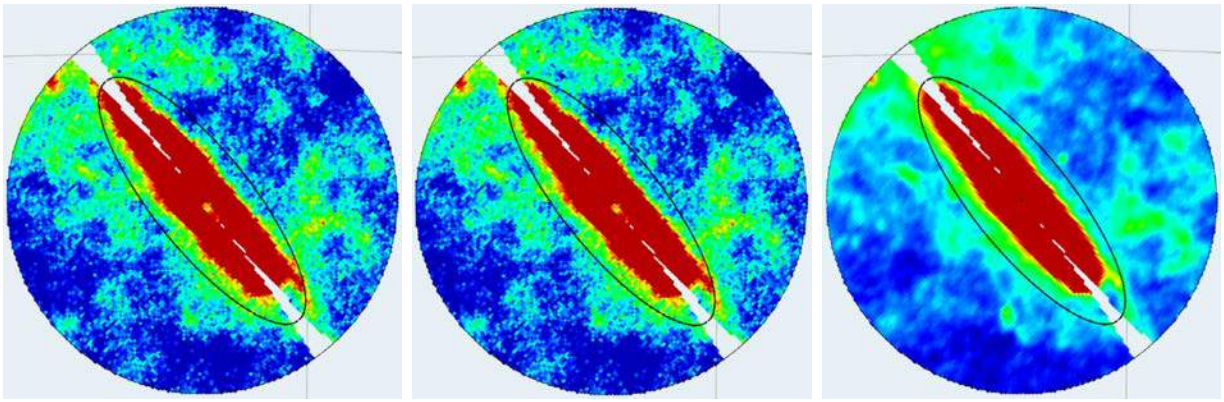

Figure 3.4: From left to right: CMB Temperature maps of the M31 galaxy at 353 GHz, 545 GHz and 857 GHz frequencies, respectively.

The values of temperature asymmetry are given in Table (3.6). Corresponding rotational velocities obtaining from Eq.(3.10) are given in the following Tables (3.7) and (3.8). In

[2]Actually, the Planck maps for 857 GHz and 545 GHz frequencies are given in MJy/sr units, which we have converted to μK via Planck High Frequency Instrument (HFI) unit conversion and colour correction coefficients [150].

Distance r (kpc)	$\nu = 857GHz$ $\frac{\Delta T}{T}(\mu K)(10^{-2})$	$\nu = 545GHz$ $\frac{\Delta T}{T}(\mu K)$	$\nu = 353GHz$ $\frac{\Delta T}{T}(\mu K)$
40	4.68	0.378	6.11
60	5.0	0.378	6.09
80	3.51	0.277	3.27
100	2.12	0.176	0.79

Table 3.6: CMB asymmetry data

Fig. (3.5) and (3.6) the illustrated dark halo rotational velocities are obtained by Eq.(3.4), Eq.(3.6) and Eq.(3.8) and thermal dust rotational velocities are obtained through Eq.(3.10). As we can see from that plots, both DL07 and GNILC dust models cannot explain through dark halo models. Note, that although high values of dust rotational velocity at 353 GHz, it has small contribution in halo rotation, because of the major part of interstellar dust are emitted mainly at high frequencies, where rotational velocities are obtained lower.

Even though we know that the dust contribution is highest in 857 GHz frequency band, we also calculate the velocities for 545 and 353 GHz bands for two different models (DL07 and GNILC). Calculations are performed for constant and non-constant temperature and spectral indexes.

From Tables (3.7) and (3.8) one can clearly see, that for DL07 model neither of two different scenarios show any significant difference, as opposed to GNILC model. For all these models and scenarios we get relatively small values for velocities for 857 GHz, which implies slow or no rotation of galactic dust component.

However, it is possible to roughly estimate the dust velocity in different way. One can assume that the dust component has a Keplerian motion and that gravity and centrifugal force are in equilibrium, i.e. the orbital velocity is given by

$$V^2(r) = \frac{GM}{r}, \tag{3.11}$$

where M is the virial mass.

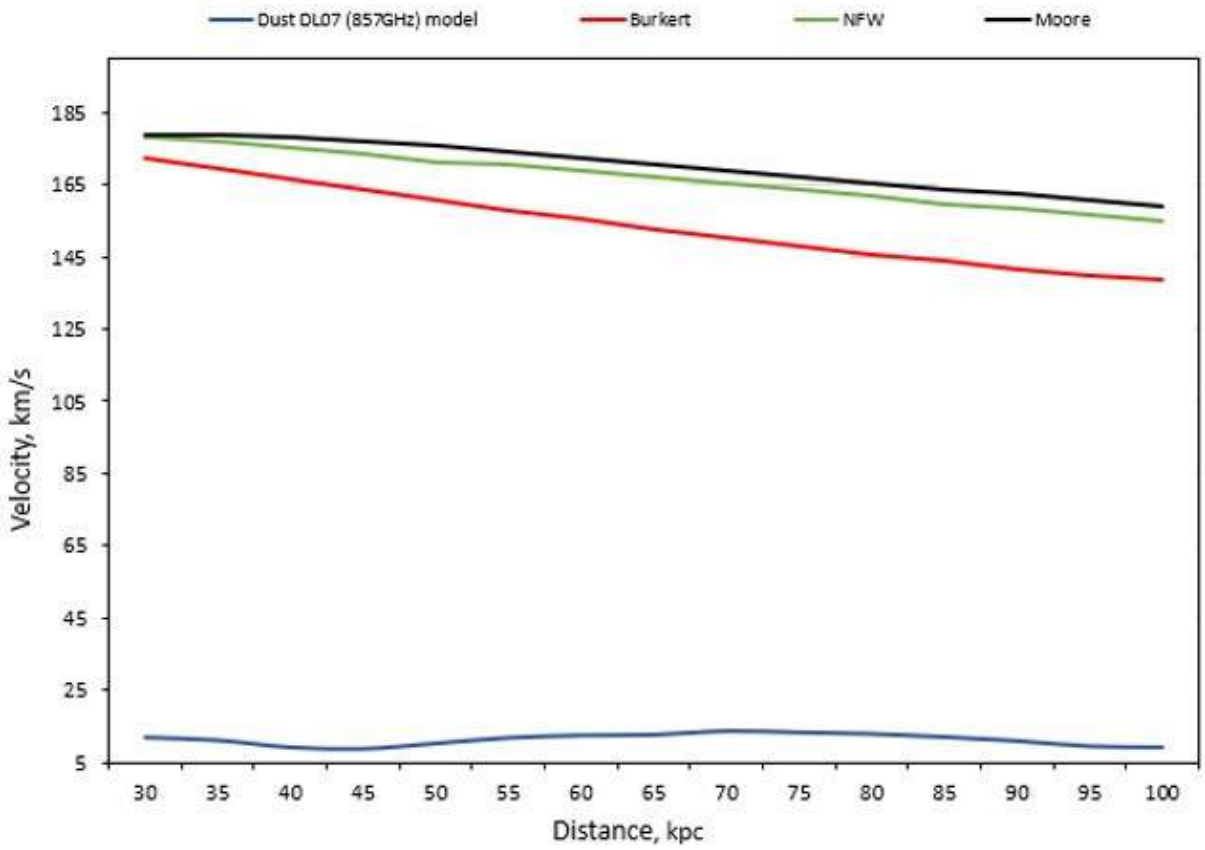

Figure 3.5: Rotational velocities from DL07 model (blue line) at 857 GHz frequencies, respectively. On the graph also shown plots of the Burkert (red line), NFW (green line) and Moore (black line) profile derived velocities.

There are different estimations for dust mass in M31. For example, according to [152] the mass is $M_{dust} = 3.8 \times 10^7 M_\odot$ and in [153] $M_{dust} = 1.3 \times 10^7 M_\odot$ values are given for dust within 18kpc from center of the M31.

However, the lower limit of $M_{dust} = 1.1 \times 10^7 M_\odot$ is derived [154] with a best-fit model value of $M_{dust} = 7.6 \times 10^7 M_\odot$, in agreement with expectations from *CO* and *HI* measurements. Here we adopt the values given by [153] and we obtain velocities in the range of 600-1200 km/s. The derived velocities strongly depend on the frequency bands, the highest values are obtained at 353 GHz, significantly higher than of 857 GHz and 545 GHz bands.

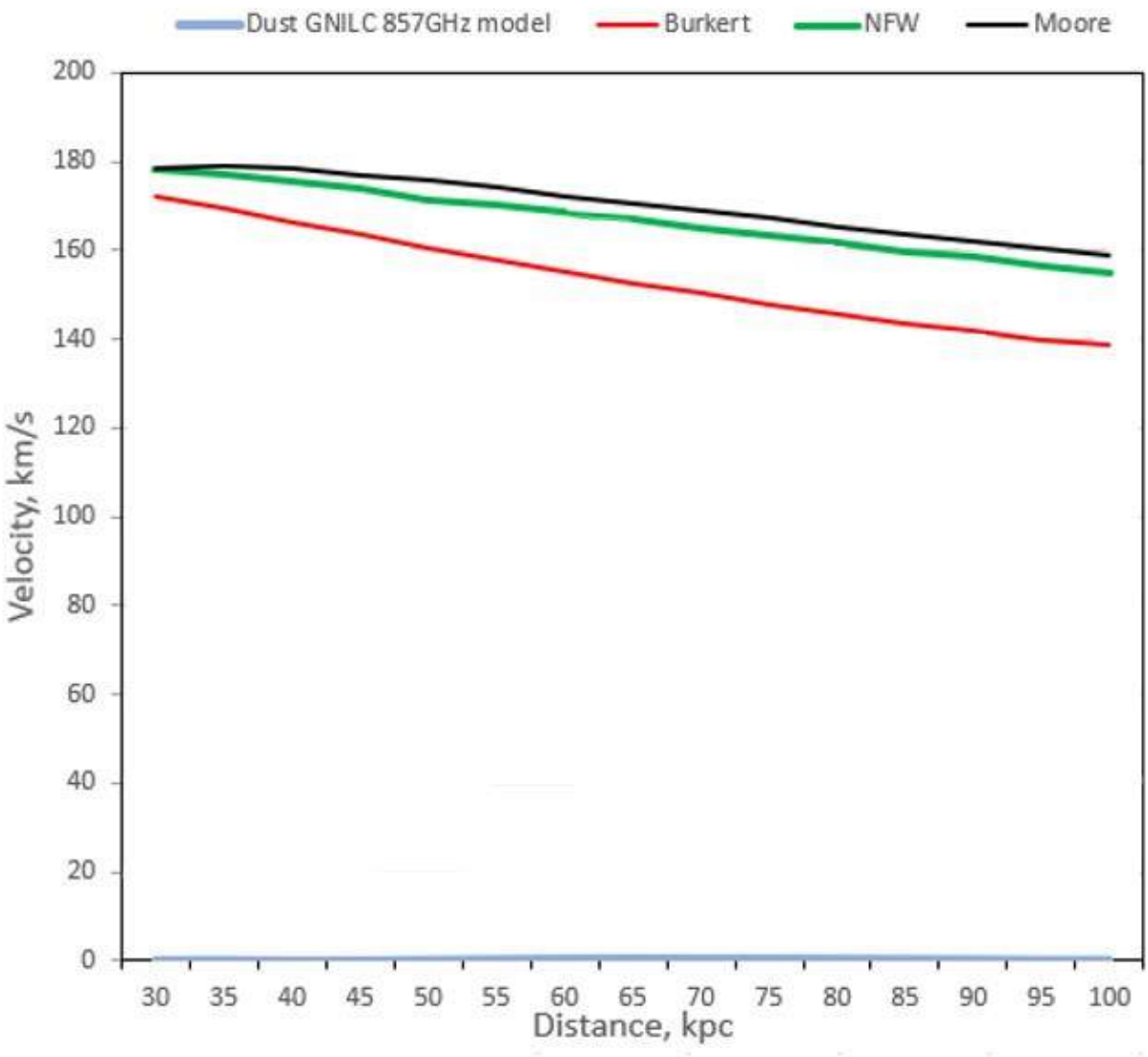

Figure 3.6: Rotational velocities from GNILC model (blue line) at 857 GHz frequencies, respectively. On the graph also shown plots of the Burkert (red line), NFW (green line) and Moore (black line) profile derived velocities.

3.2.6 Conclusions

Whence various details of the rotation of disks of spiral galaxies are well studied, the structure and the rotation of galactic dark halos still remain far less established. Here we attempted to study the halo dynamics using M31 galaxy dust emission data vs the microwave data. The microwave data can trace dark matter distribution at larger scales, e.g. [91]. We derived the velocity values for the rotation of the dust component using two different models, DL07

DL07 $\beta = const$ T=const			
Distance r (kpc)	$\nu = 857GHz$ V_{rot}(km/s)	$\nu = 545GHz$ V_{rot}(km/s)	$\nu = 353GHz$ V_{rot}(km/s)
40	9.45	36.21	359.41
60	12.6	70.08	643.30
80	13.02	99.38	474.15
100	9.47	142.41	640.54
DL07 $\beta = const$ $T \neq const$			
Distance r (kpc)	$\nu = 857GHz$ V_{rot}(km/s)	$\nu = 545GHz$ V_{rot}(km/s)	$\nu = 353GHz$ V_{rot}(km/s)
40	9.43	36.27	357.05
60	12.61	70.05	644.78
80	13.0	99.52	479.12
100	9.51	142.35	635.2

Table 3.7: M31 halo rotational velocities according to DL07 model.

GNILC $\beta \neq const$, $T \neq const$			
Distance r (kpc)	$\nu = 857GHz$ V_{rot}(km/s)	$\nu = 545GHz$ V_{rot}(km/s)	$\nu = 353GHz$ V_{rot}(km/s)
40	0.34	1.85	25.06
60	0.51	3.55	50.63
80	0.50	7.41	84.71
100	0.41	7.79	78.55
GNILC $\beta = 2$, $T = const$			
Distance r (kpc)	$\nu = 857GHz$ V_{rot}(km/s)	$\nu = 545GHz$ V_{rot}(km/s)	$\nu = 353GHz$) V_{rot}(km/s)
40	8.97	38.74	427.08
60	12.0	67.66	563.87
80	11.36	134.89	511.65
100	9.22	140.21	536.14

Table 3.8: M31 halo rotational velocities according to GNILC model.

and GNLIC. For 857 GHz frequency band we get relatively small velocity values for both models, while for 545 GHz we obtained up to 145 km/s and it is clear that the change of T_d does not affect the velocity values. It is worth to stress the relatively large values for 343 GHz, up to 650 km/s, which is consistent with our estimate of 600-1200 km/s. The dust emission flux densities which we have calculated from CMB maps have lower values at 545 GHz and 353 GHz bands. Since we can express the dust masses through the observed flux

densities and since the flux density at 857 GHz is significantly higher, the major part of the dust emission comes at this band. At this band the majority of dust velocities have low values, i.e. implying rather weak rotation.

The dust component alone certainly cannot entirely cover the entire radiation emission mechanisms in the galactic halos, however the accurate information on the dust dynamics can help to fill the gap between theoretical and measured velocity curves, including those obtained from the *Planck* microwave temperature maps.

3.3 On the role of dust in the microwave emission of galactic halos

3.3.1 Introduction

The study of the *Planck* data [155] in several microwave bands had revealed temperature asymmetry for several nearby edge-on spiral galaxies extending to their halos [56, 57, 59, 58, 60]. That asymmetry is frequency independent, thus indicating its Doppler nature. Previously we have studied [25] that effect based on the microwave data for the galaxy M31, namely, regarding the possible contribution of the thermal dust in the rotation of the halo. Here we continue the analysis, now using the data on galaxies M81 and M82. Since the galactic halos act as probes for testing of modified gravity models, we therefore discuss also that aspect with certain models based on revealed role of the thermal dust in the rotation of the halos.

Among various models the baryonic matter in the form of molecular clouds was suggested as the possible content of the dark matter in galaxies including their halos [156]. Then, the mentioned microwave asymmetry of Doppler nature has to reflect that. In our previous study of M31 galaxy [25] using the microwave temperature asymmetry data we have concluded that the thermal dust cannot be the main contributor to the dark matter, since the rotation

velocity provided by dust component is quite low. So, here we will perform the analysis for the M82 and M81 galaxies.

Crucial parameter of the interstellar dust is the optical depth, which indicates the fraction of the intensity decreased by extinction of the light emitted by dust particles grains at line-to-sight propagation. In general, when the light ray propagates through a dusty medium it weakens by extinction and is reinforced by thermal emission or scattering. It is clear, that galactic halos are optically thin ($\tau \ll 1$) and the optical depth decreases at large galactocentric distances. We obtain the optical depth as a function of the galactocentric radii, for which we use several Planck maps at different frequency bands. As in [25], also here we adopt a Modified Blackbody (MBB) spectrum for deriving optical depth at large distances, as well as two dust models, i.e. DL07 [157] and GNILC, see [158]. The temperature is a key parameter of the dust through which the dust is classified to warm and cold components. The warm dust can absorb energetic photons and heat up to 40K. For the cold dust illuminated by the background interstellar radiation field, the temperature is $10-25$K. In fact, the dust temperature strongly depends on the grain size, chemical composition, distance from the radiation source. So for cold grains, which are in local thermodynamic equilibrium (LTE) with interstellar radiation field (ISRF), the Kirchhoff law is applicable, according to which the ratio of emission and absorption coefficients are given via Planck function. The latter depends only on the temperature for given frequency band. In our work the calculations have been performed for large galactocentric distances corresponding to the presence of ISRF (see [157]). We fix he dust temperature from the *Planck* maps via MBB fitting procedure. Since the major fraction of the interstellar dust consists of cold dust component (over 90% [159]), we consider cold dust models ($T < 22$K) with typical values of the spectral index $\beta = (1.5-2)$ taken from *Planck* maps (see Fig.(3.7)), using the same frequency bands both for cold dust emission and temperature asymmetry maps.

We use *Planck* High Frequency Instrument (HFI) data [160] at three bands, 857 GHz,

545 GHz, 353 GHz and determine the relevant microwave temperature asymmetry. We have calculated the temperature asymmetry values using the methods of [59, 58, 60].

3.3.2 Rotation velocities of M82 halo

M82 is one of the brightest infrared objects located at distance of 3.63Mpc from us (in M81 group) [161]. It is a starburst late type galaxy, with 80^0 inclination angle [162]. The origin of the nuclear starburst region (with 500pc size[163]), is assumed to be due to a close encounter between M82 and NGC3077[70]. The near infrared data indicate the presence of bar with 1kpc size [164]. As reported by [165], the major part of galaxy's mass ($\approx 10^{10}\mathrm{M}_{\odot}$) is located in the inner region (within 2kpc). Besides this, there is a bulge component with $10^7\mathrm{M}_{\odot}$ mass and 7.5pc size [166]. It also has spiral arms which are not visible on the optical images (due to presence of dust particles). However, they can be seen on the near infrared wavelengths [167]. Also, M82 is a gas rich galaxy with $30-40\%$ gas fraction[168]. Furthermore, there are some evidences for the presence of dust in the inner disk [169]. The rotation curve of the M82 has been studied by many authors. According to [170] it is flat within $1-4$kpc, with $\approx 10^{10}\mathrm{M}_{\odot}$ dynamical mass. However, starting from 1.5kpc to 10kpc radius, the rotation velocity, derived by HI kinematics, sharply decreases from 120km/s to 50km/s [171]. It should be mentioned that although different components of M82, such as bar, bulge, disk or spiral arms are well studied. However, less information is available about its halo.

Dust emission parameters for M82 halo: Here we attempt to obtain radial behavior of dust emission optical depth [25] using several *Planck* maps [144, 148]. The description of used *Planck* maps, as well as calculation technique is described in [25]. Similarly to M31 [25], we calculate optical depth for two dust models: DL07[157] and GNILC[158]. The necessary parameters of the MBB spectrum, dust spectral index β and temperature T_d, are taken from *Planck* GNILC maps (see Fig.(3.7)).

The parameters used in this paper are calculated as follows: from *Planck* map we take

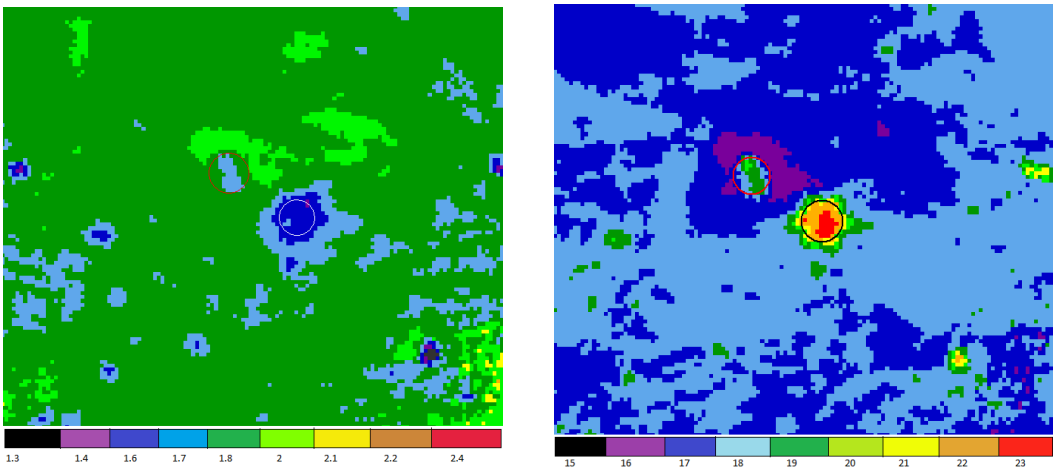

(a) M31 dust spectral index (β) map

(b) M31 dust temperature(T) map

Figure 3.7: M81 and M82 spectral index (a) and temperature (b) maps from GNILC, with 10° width region. In the β map M81 galaxy marked by red circle and M82 galaxy- white circle. While in the temperature map M81 marked by red circle and M82- black circle. Each colored pixel gives the corresponding values of β and T. Here β is a dimensionless quantity, while temperature given in K units.

circles of 15kpc, 20kpc and 25kpc radii, their centers coincide with the center of the galaxy. Then we calculate the average value of each parameter for given radii. For DL07 model spectral index is equal to 2 for all radii, while in the case of GNILC model β varies within large distances. For M82 and M81 galaxies there is also an anti correlation between β and T_d (see Table (3.9)), which is appeared during MBB spectrum fitting (caused by noise) [173].

Distance	Microwave temperature asymmetry $\frac{\lvert\Delta T\rvert}{T_d}(\mu K)$			Spectral index	Temperature
$r(kpc)$	857 GHz	545 GHz	353 GHz	(β)	$T_d(K)$
15	0.0493	0.305	4.81	1.577	20.381
20	0.0472	0.305	3.24	1.639	19.382
25	0.0396	0.254	1.68	1.687	18.695

Table 3.9: Dust temperature, spectral index and microwave asymmetry data.

As already mentioned, we derive optical depth τ from MBB spectrum. We use three frequency maps for two dust models, which are illustrated in Fig.(3.8) and (3.9).

It should be noticed that τ remains almost unchanged for $T_d \neq const$, however, it strongly depends on the spectral index. For example, in the case of DL07 ($\beta = 2$) the order of τ

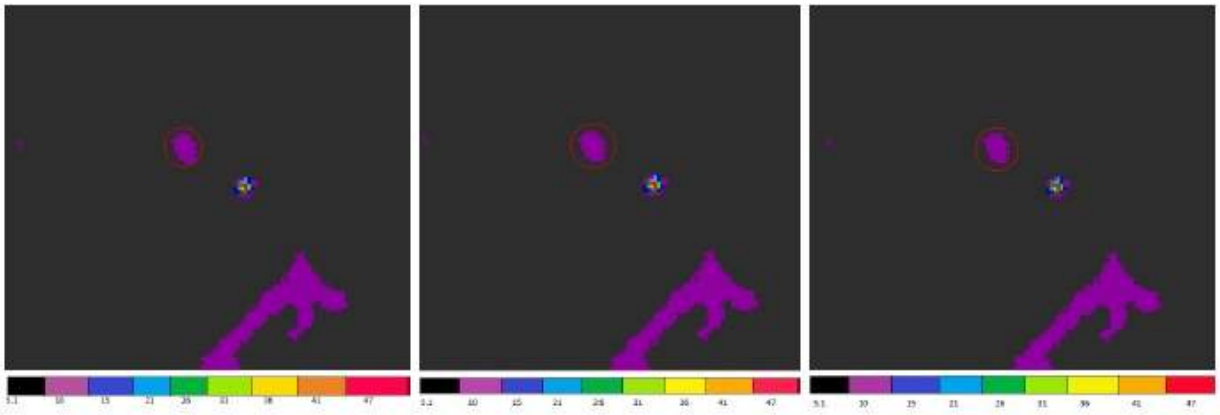

Figure 3.8: M81 (marked by red circle) and M82 dust DL07 maps at 353 GHz, 545 GHz and 857 GHz frequencies

is 10^{-3}, while for GNILC ($\beta \neq const$) it is 10^{-2} . In fact, for all models and all cases τ decreases for large radii (see Tables (3.10-3.12)).

DL07, $\beta = 2$, $T = 19.48K$			
Distance r (kpc)	Optical depth τ_{857} (10^{-3})	Optical depth τ_{545} (10^{-3})	Optical depth τ_{353} (10^{-3})
15	1.730	2.959	4.602
20	1.231	2.306	3.431
25	1.038	1.982	3.210
DL07, $\beta = 2$, $T \neq const$			
Distance r (kpc)	Optical depth τ_{857} (10^{-3})	Optical depth τ_{545} (10^{-3})	Optical depth τ_{353} (10^{-3})
15	1.650	2.818	4.387
20	1.231	2.313	3.515
25	1.079	2.064	3.344

Table 3.10: The optical depth for DL07 model.

M82 dust rotation velocities: The rotation velocities of M82 are obtained via the formula [47]

$$\frac{|\Delta T|}{T_d} = \frac{2v\, sini}{c}\tau, \tag{3.12}$$

where the inclination angle $i = 80^{\circ}$, the temperature asymmetry $\frac{|\Delta T|}{T_d}$ and optical depth τ

GNILC, $\beta = 2$, $T \neq const$			
Distance r (kpc)	Optical depth τ_{857} (10^{-3})	Optical depth τ_{545} (10^{-3})	Optical depth τ_{353} (10^{-3})
15	1.065	2.492	4.341
20	0.973	2.295	4.058
25	0.941	2.160	3.721

Table 3.11: The optical depth for GNILC model with constant β.

GNILC, $\beta \neq const$, $T = const$			
Distance r (kpc)	Optical depth τ_{857} (10^{-2})	Optical depth τ_{545} (10^{-2})	Optical depth τ_{353} (10^{-2})
15	1.858	3.584	4.932
20	1.116	2.223	3.366
25	0.778	1.551	2.422

Table 3.12: The optical depth for GNILC model with varying β.

depend not only on the radius, but also on the given frequency band. In Eq.(3.12) v is the dust rotational velocities at 15kpc, 20kpc, 25kpc distances.

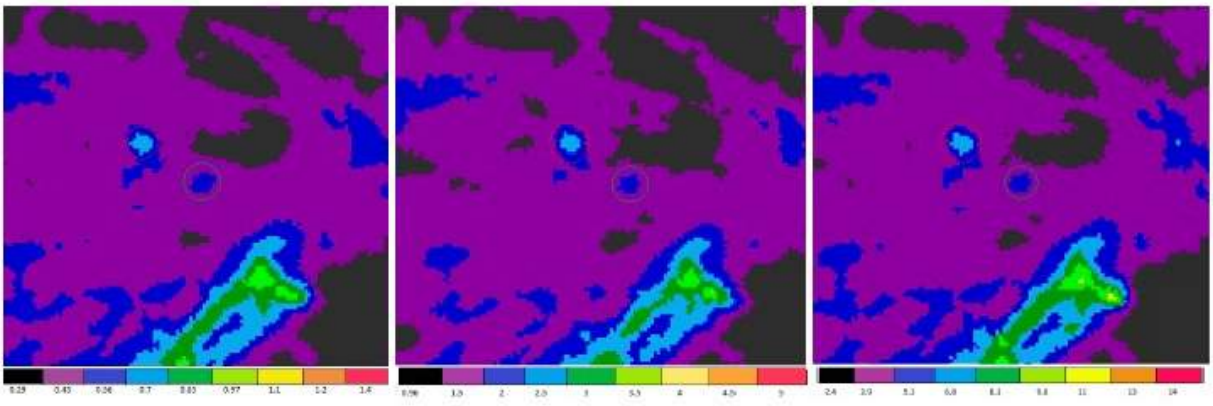

Figure 3.9: M81 (marked by red circle) and M82 (marked by green circle) dust GNILC maps at 353 GHz, 545 GHz and 857 GHz frequencies

So, based on Eq.(3.12) we aim to find out whether interstellar dust component can give a significant contribution in the halo rotation. Since we use two different dust models at three frequency bands, the obtained velocities are different. The temperature asymmetry

has relatively high values especially at 353 GHz band (see Table (3.9)). M82 galaxy's CMB maps at the two high frequencies shown in the Fig.(3.10).

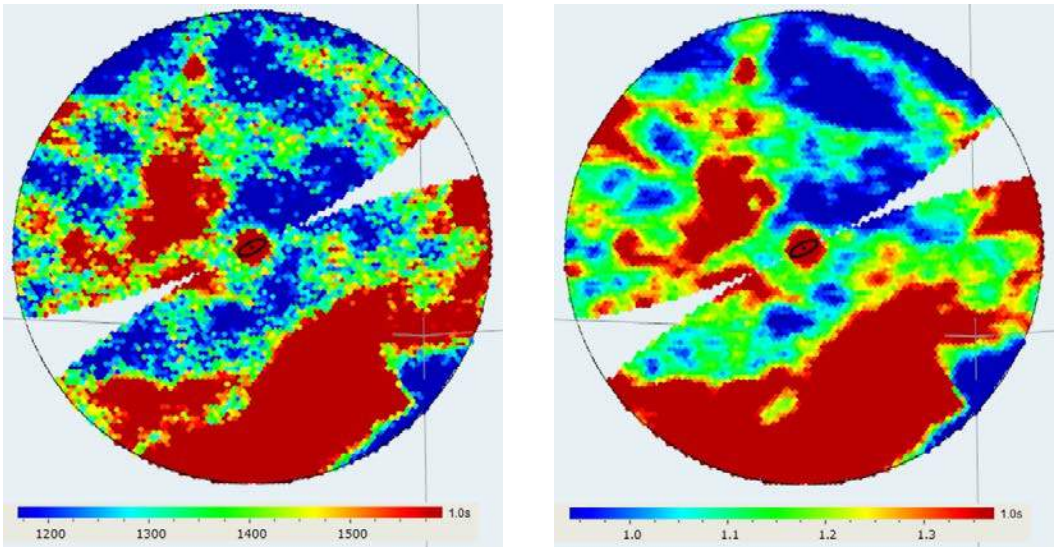

(a) (b)

Figure 3.10: CMB temperature maps of M82 galaxy at 353 GHz (a) and 545 GHz (b) frequencies.

As we can see from Table (3.13) and (3.14), the rotation velocities vary significantly according to frequency. On the other hand velocities derived by DL07 dust model, have their lowest values at 857 GHz band. In this case, there is no significant change of velocity within the specified radius. Namely, at 545 GHz band it rises up to 20kpc, then decreases only by 0.61km/s. Finally, at 353 GHz it decreases from 159km/s to 80km/s. As in the DL07 case, for GNILC the velocities have their lowest values at 857 GHz and relatively higher ones at 545 GHz and 353 GHz bands.

DL07, $\beta = const$, $T = const$			
Distance r (kpc)	$\nu = 857GHz$ V_{rot} (km/s)	$\nu = 545GHz$ V_{rot} (km/s)	$\nu = 353GHz$ V_{rot} (km/s)
15	4.35	15.76	159.69
20	5.86	20.24	163.74
25	5.84	19.63	80.12

Table 3.13: M82 dust rotational velocities by DL07 model.

GNILC $\beta \neq const$, $T = const$			
Distance r (kpc)	$\nu = 857GHz$ V_{rot} (km/s)	$\nu = 545GHz$ V_{rot} (km/s)	$\nu = 353GHz$ V_{rot} (km/s)
15	0.405	1.302	14.91
20	0.647	2.10	14.71
25	0.779	2.507	10.61

Table 3.14: M82 dust rotational velocities by GNILC model.

The optical depth obtained according to MBB formula strongly depends on the flux density in given frequency band and the radial distance. Flux density decreases at large galactocentric distances. It also decreases from 857 GHz to 353 GHz band. In general, the dust radiates on broad range of frequencies, e.g. the warm grains, which have small size, emit mainly at NIR/MIR range, while cold grains of larger size emit at submillimeter range. The cold dust within the ISRF emits at high frequencies ($\nu > 353$ GHz), however for our work we consider the three bands in view of the temperature asymmetry data. Namely, for both - the microwave data and the dust - we consider the same bands. Consequently, at 857 GHz, the dust rotational velocity has the lowest value. We will discuss these results in more details in Section 2.3 and check that the dust mass has higher values at 353 GHz, 545 GHz and therefore the velocities at these bands are higher than those at 857 GHz. Actually, the frequency-dependent velocity appears during the calculation of optical depth, since we use the MBB spectrum. Namely, we calculate the mean flux density ($S(\nu)$) for given galactocentric radii and given frequency, then obtain the optical depth $\tau(\nu)$ via MBB formula and finally, according to Eq.(3.12) we obtain the dust rotational velocity, which depends not only on the dust model, but also on given frequency.

Dust masses: Dust mass depends on the frequency at which it is emitted. For example, in [174] the dust masses have been estimated at 37μm ($\approx$ 8102 GHz) and 31μm ($\approx$ 9670 GHz) within 1kpc. According to emission peaks at these wavelengths the estimated masses are $3.6 \times 10^4 M_\odot$ and $1.8 \times 10^4 M_\odot$, respectively. At wavelength ($\lambda = 1.2$mm) [175] the total dust mass in the inner region (3kpc) is $7.5 \times 10^6 M_\odot$. Furthermore, the dust mass has been

estimated to be roughly $(1-3)\times 10^5 M_\odot$ based on the giant star population and starburst model [176] (within 500pc). At 450μm range (666 GHz), $M_d = 3.66\times 10^6 M_\odot$ has been reported by [177].

For our bandwidths we estimate dust mass from [143] :

$$M_{dust} = \frac{\tau D^2 \Omega}{k}, \tag{3.13}$$

where τ, $k = \frac{3Q_\nu}{4a\rho}$, a and ρ stand for the optical depth, the mass absorption coefficient, dust grain radius and density, respectively, Ω is the solid angle, D is the distance between the source and the observer, Q_ν is the grain emission efficiency. Since these quantities are not well defined for our frequencies, we adopt a power law shape of k and parametrized form $k = 0.1\mathrm{cm}^2\mathrm{g}^{-1}(\frac{\nu}{1000(\mathrm{GHz})})^\beta$ according to [82]. In this way we estimate the dust mass for 857 GHz, 545 GHz and 353 GHz frequencies and two models: DL07 and GNILC (see Tables (3.15) and (3.16)).

DL07, $\beta = const$, $T = const$			
Distance r (kpc)	$\nu = 857GHz$ $M_\odot$ (10^7)	$\nu = 545GHz$ $(M_\odot$ (10^7)	$\nu = 353GHz$ $M_\odot$ (10^7)
15	0.313	1.265	3.542
20	0.188	0.785	2.417
25	0.131	0.547	1.739

Table 3.15: M82 dust masses for DL07 model.

GNILC, $\beta \neq const$, $T = const$			
Distance r (kpc)	$\nu = 857GHz$ $M_\odot$ (10^6)	$\nu = 545GHz$ $M_\odot$ (10^6)	$\nu = 353GHz$ $M_\odot$ (10^6)
15	0.291	1.045	3.305
20	0.207	0.814	2.607
25	0.174	0.700	2.305

Table 3.16: M82 dust masses for GNILC model.

In fact, even in the same frequencies different dust masses (up to an order of magnitude)

are derived from DL07 and GNILC models [3]. From these masses one can obtain the dust orbital velocities

$$V^2(r) = \frac{GM_d}{r}, \tag{3.14}$$

where M_d is the dust mass. Note that, the dust mass can be minor fraction of the entire galactic dynamical mass and therefore the rotation velocity obtained by the dust mass can define not the global galactic rotational velocity. Regarding the Doppler induced microwave temperature asymmetry, we assume that it is determined by presence of cold dust and hence the obtained velocities are attributed only to the dust component. If in Eq.(3.14) we also add the stellar mass or other baryonic components, we will obtain higher velocities, than what we have according to Eq.(3.12). This is due to the fact that the ISM fraction with respect to the total baryonic mass is about 10% and the dust mass contribution in ISM is small. On the other hand, by including other baryonic components in the Eq.(3.14) one has to take them into account also in Eq.(3.12), since the rotation determined by the microwave temperature asymmetry with respect to dust component is also present there (expressed via dust emission optical depth (τ)). Since we are interested in the rotation at large galactocentric distances, we do not take into account the effects important at small distances from the galactic center. The results are presented in Tables (3.17) and (3.18).

DL07, $\beta = const$, $T = const$			
Distance r (kpc)	$\nu = 857GHz$ V_{rot} (km/s)	$\nu = 545GHz$ V_{rot} (km/s)	$\nu = 353GHz$ V_{rot} (km/s)
15	0.950	1.911	3.198
20	0.736	1.505	2.641
25	0.615	1.256	2.240

Table 3.17: M82 dust rotational velocities by DL07 model.

Comparing the above results with the velocities obtained with Eq.(3.12), we see that the

[3]The reason of such differences for the dust masses (in the same frequency) arises from the given dust model i.e. DL07 and GNILC models have different parameters (e.g. spectral index β, optical depth τ) describing the dust emission properties and composition.

GNILC, $\beta \neq const$, $T = const$			
Distance r (kpc)	$\nu = 857GHz$ V_{rot} (km/s)	$\nu = 545GHz$ V_{rot} (km/s)	$\nu = 353GHz$ V_{rot} (km/s)
15	0.289	0.549	0.976
20	0.244	0.484	0.867
25	0.224	0.449	0.815

Table 3.18: M82 dust rotational velocities by GNILC model.

former have significantly lower values.

3.3.3 Rotation velocities of M81 halo

M81 (NGC3031) is a SA(s)ab galaxy with 26.9arcmin angular diameter and about 3.6 ± 0.2Mpc distance from us [61]. It is the largest member of the M81 Group and its apparent magnitude in the B band is 7.69. It has −35km/s heliocentric radial velocity and its extinction in the B band (A_B) is 0.36 [71]. Also there is an evidence for the presence of HI bridge and interaction between M81 and M82 [70].

M81 dust emission parameters: We calculate dust emission optical depth using the value of spectral index and dust temperature. According to Table (3.19), the cold dust temperature is lower compared to M82. Actually, for M82 mean temperature and spectral index [4] are $T_d = 19.48$K, $\beta = 1.634$, respectively, whereas for M81 $T_d = 16.92$K, $\beta = 1.840$.

Distance	Microwave temperature asymmetry $\frac{\Delta T}{T_d}$ (μK)			Spectral index	Temperature
r (kpc)	857 GHz	545 GHz	353 GHz	(β)	T_d(K)
15	0.0296	0.351	8.904	1.822	17.083
20	0.0123	0.205	6.140	1.847	16.845
25	0.0037	0.0586	3.783	1.853	16.848

Table 3.19: M81 dust temperature, spectral index and microwave temperature asymmetry data.

The optical depths for three frequencies and two models are presented in Tables (3.20)

[4]The values of spectral index for both M81 and M82 galaxies and also the temperature and flux density for each frequency have been calculated from Planck GNILC maps[158]. Description of the Planck maps, as well as the calculation technique have been presented in [25].

and (3.21).

DL07, $\beta = 2$, $T = 16.92K$			
Distance r (kpc)	Optical depth τ_{857} (10^{-3})	Optical depth τ_{545} (10^{-3})	Optical depth τ_{353} (10^{-3})
15	1.57	3.48	5.80
20	1.32	2.94	4.90
25	1.14	2.60	4.34
DL07, $\beta = 2$, $T \neq const$			
Distance r (kpc)	Optical depth τ_{857} (10^{-3})	Optical depth τ_{545} (10^{-3})	Optical depth τ_{353} (10^{-3})
15	1.55	3.46	5.77
20	1.32	2.94	4.94
25	1.15	2.61	4.38

Table 3.20: M81 optical depth for DL07 model.

GNILC, $\beta \neq const2$, $T = const$			
Distance r (kpc)	Optical depth τ_{857} (10^{-2})	Optical depth τ_{545} (10^{-2})	Optical depth τ_{353} (10^{-2})
15	0.531	1.084	1.726
20	0.402	0.848	1.354
25	0.360	0.764	1.230

Table 3.21: M81 optical depth for GNILC model.

In the case of Table (3.20) the optical depth varies significantly in GNILC model, where $\beta \neq const$. In this case again there is almost no temperature dependency, hence the optical depths for DL07 and GNILC models (when both temperature and spectral index are constant) are determined only by the flux density. Thus, the values of optical depths are close to each other.

M81 dust rotational velocities and masses: As in case of M82, we use Eq.(3.12) for calculation of velocities, where for galaxy disk the inclination angle we adopt as 58° (we

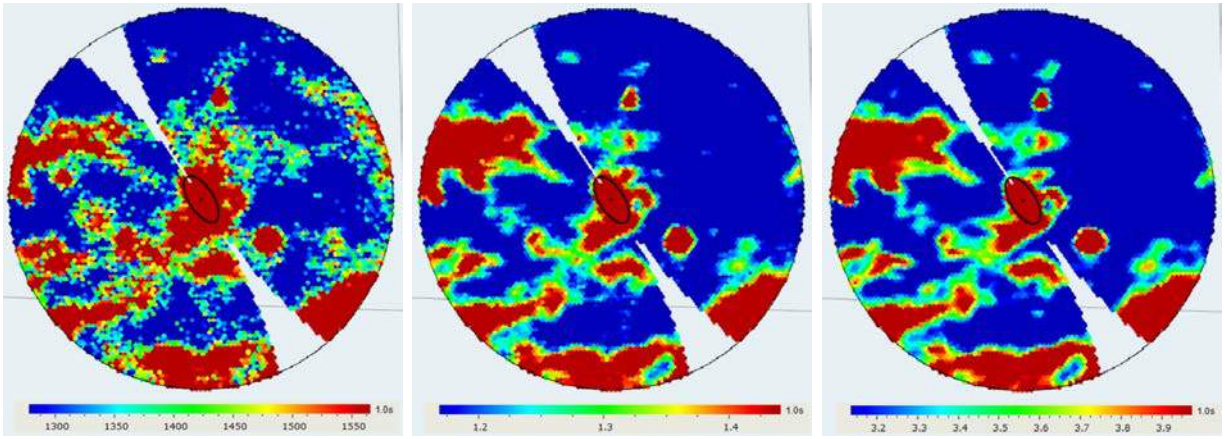

Figure 3.11: From left to right: CMB temperature maps of M81 galaxy at 353 GHz, 545 GHz and 857 GHz frequencies, respectively.

assume, that the halo has the same inclination angle as the disk). The CMB temperature fields of the M81 galaxy are shown in the Fig.(3.11).

The velocities have been illustrated in Tables (3.22) and (3.23). Once again, we obtain the most high value at 353 GHz (due to high value of microwave temperature asymmetry). However, these values are significantly low compared to M31's velocities [25] because of relatively low value of optical depth. For example, optical depths for M31 galaxy (at 353 GHz) vary within $10^{-3} - 10^{-4}$ range, while in this case the order of magnitude of the optical depth is more or less the same, similarly to the discussion in the previous section.

DL07, $\beta = const$, $T = const$			
Distance r (kpc)	$\nu = 857$ GHz V_{rot} (km/s)	$\nu = 545$ GHz V_{rot} (km/s)	$\nu = 353$ GHz V_{rot} (km/s)
15	3.35	81.2	272.37
20	1.66	12.3	222.16
25	0.57	4	154.53

Table 3.22: M81 dust rotational velocities for DL07 model obtained from microwave temperature asymmetry data.

The dust rotation velocity can be obtained from the dust mass as well. There are various estimates of M81's dust mass. According to [179] the mass is $3.4 \times 10^7 M_\odot$ for $100 - 500\mu$m wavelengths range. Another value of dust mass, $1.293 \times 10^7 M_\odot$, is given in DustPedia [180].

GNILC, $\beta \neq const$, $T = const$			
Distance r (kpc)	$\nu = 857$ GHz V_{rot} (km/s)	$\nu = 545$ GHz V_{rot} (km/s)	$\nu = 353$ GHz V_{rot} (km/s)
15	0.98	13.21	91.92
20	0.54	9.90	80.75
25	0.18	3.15	54.93

Table 3.23: M81 dust rotational velocities for GNILC model obtained from microwave temperature asymmetry data.

Here we also use Eq.(3.13) for determining dust masses at three frequencies and two dust models. Since the mass absorption coefficient (k) depends only on given frequency, we adopt the same k which we have used for M82. As for the optical depth, we use values from Tables (3.11) and (3.12), calculated from MMB spectrum.

Performing the same analysis as of M82, we find out the masses and the velocities for M81, as presented in Tables (3.24-3.27).

DL07, $\beta = const$, $T = const$			
Distance r (kpc)	$\nu = 857$ GHz $M_\odot$ (10^6)	$\nu = 545$ GHz ($M_\odot$ (10^6)	$\nu = 353$ GHz $M_\odot$ (10^6)
15	0.260	1.210	4.104
20	0.219	1.025	3.469
25	0.189	0.904	3.073

Table 3.24: M81 dust mass for DL07 model.

GNILC, $\beta \neq const$, $T = const$			
Distance r (kpc)	$\nu = 857$ GHz $M_\odot$ (10^5)	$\nu = 545$ GHz $M_\odot$ (10^6)	$\nu = 353$ GHz $M_\odot$ (10^6)
15	8.814	3.770	9.147
20	6.673	2.949	8.575
25	5.976	2.657	8.199

Table 3.25: M81 dust mass for GNILC model.

Thus, we use two approaches for deriving the dust rotation velocity. First, we compute it using the microwave temperature asymmetry data. Then, we obtain the velocity via

DL07, $\beta = const$, $T = const$			
Distance r (kpc)	$\nu = 857$ GHz V_{rot} (km/s)	$\nu = 545$ GHz V_{rot} (km/s)	$\nu = 353$ GHz V_{rot} (km/s)
15	0.273	0.591	1.088
20	0.251	0.544	1.00
25	0.233	0.510	0.941

Table 3.26: M81 dust rotational velocities for DL07 model derived with Eq.(3.14).

GNILC, $\beta \neq const$, $T = const$			
Distance r (kpc)	$\nu = 857$ GHz V_{rot} (km/s)	$\nu = 545$ GHz V_{rot} (km/s)	$\nu = 353$ GHz V_{rot} (km/s)
15	0.504	1.043	1.625
20	0.438	0.922	1.573
25	0.415	0.875	1.538

Table 3.27: M81 dust rotational velocities for GNILC model derived with Eq.(3.14).

Eq.(3.14) and find that the obtained velocities in the first case are significantly higher than those determined by microwave temperature asymmetry data. In the second case i.e. where we use pure dust parameters without microwave data, the velocities have smaller values.

3.3.4 Modified gravity and dark halos

The essential fraction of the dark matter in galaxies is commonly believed to be stored in the halos and various density profiles are proposed to fit the observations. Here we list some of the commonly used profiles to model dark matter halos. The so-called pseudo-isothermal profile is written as [181]

$$\rho(r) = \rho_0 \left[1 + \left(\frac{r}{r_c}\right)^2\right]^{-1}, \tag{3.15}$$

where ρ_0 denotes the central density and r_c is the core radius. The Navarro-Frenk-White (NFW) [15] profile with broad range of applications is

$$\rho(r) = \frac{\rho_{crit}\delta_c}{\left(\frac{r}{r_c}\right)\left(1 + \frac{r}{r_c}\right)^2}, \tag{3.16}$$

where ρ_{crit} is the critical density of the universe defined as

$$\rho_{crit} = \frac{3H^2}{8\pi G}, \tag{3.17}$$

H stands for the Hubble constant. One of important features of this profile is that it depends directly on the cosmological parameter ρ_{crit}. The dimensionless parameter δ_c relates the two radii i.e. ρ_{crit} to ρ_0 for the halo under consideration: $\rho_{crit} = \delta_c \rho_0$. Along with NFW, other profiles are also considered for modeling the halos, e.g. the Burkert one[16]

$$\rho(r) = \frac{\rho_{crit}\delta_c}{\left(1 + (\frac{r}{r_c})\right)\left(1 + (\frac{r}{r_c})^2\right)} \tag{3.18}$$

and Moore profile [17]:

$$\rho(r) = \frac{\rho_{crit}\delta_c}{\left(\frac{r}{r_c}\right)^{\frac{3}{2}}\left(1 + (\frac{r}{r_c})^{\frac{3}{2}}\right)} \tag{3.19}$$

These three profiles have been used to model the dark matter halo of M31 [138].

Recalling the fact that the first indirect observation of dark matter in galaxies was related to the virial theorem

$$\sigma^2 = \frac{GM}{R}, \tag{3.20}$$

where σ, M and R stand for the velocity dispersion, the virial mass and the virial radius, respectively, for above mentioned halo profiles the velocity dispersions read as (see [25] for more details)

$$\sigma^2_{NFW} = 4\pi G\rho_c \frac{r_c^3}{r}(ln(1 + \frac{r}{r_c}) - \frac{\frac{r}{r_c}}{(1 + \frac{r}{r_c})}), \tag{3.21}$$

$$\sigma^2_{Moore} = \frac{8}{3}\pi G\rho_c \frac{r_c^3}{r}(ln(1 + (\frac{r}{r_c})^{\frac{3}{2}})), \tag{3.22}$$

$$\sigma^2_{Burkert} = 2\pi G\rho_c \frac{r_c^3}{r}((ln(1 + \frac{r}{r_c})\sqrt{1 + (\frac{r}{r_c})^2}) - \arctan(\frac{r}{r_c})). \tag{3.23}$$

In addition to these profiles, another widely used profile is the Einasto law [182]

$$\rho(r) = \rho_e e^{\left(-d_n\left(\left(\frac{r}{r_e}\right)^{\frac{1}{n}}-1\right)\right)} \tag{3.24}$$

In Einasto model [183] d_n is function of n such that ρ_e is the density at the radius r_e of the volume containing half of the total mass.

The cosmological constant Λ entering the Einstein equations

$$G_{\mu\nu} + \Lambda g_{\mu\nu} = \frac{8\pi G}{c^4} T_{\mu\nu}, \tag{3.25}$$

is currently considered to fit the dark energy data.

Various classes of modified gravity models are being considered to explain the dark matter and dark energy data. The models include e.g. scalar field entering the action

$$S = \frac{c^4}{16\pi} \int \left(\phi R - \frac{\omega}{\phi}\partial_a\phi\partial^a\phi\right)\sqrt{-g}d^4x, \tag{3.26}$$

where ω is a dimensionless constant known as Dicke coupling constant [184]. Other models are based on the modification of Einstein-Hilbert action

$$S = \frac{c^4}{16\pi G} \int R\sqrt{-g}\, d^4x, \tag{3.27}$$

where R is the Ricci scalar. This defines the $f(R)$ theories of gravity [20, 19]. All modified theories are reduced to ordinary General Relativity at specific regimes.

The Modified Newtonian Dynamics (MOND) [18] is one of the well known model for explaining the dark matter problem. In MOND the Newton's second law is modified as

$$F = ma\mu(\frac{a}{a_0}), \tag{3.28}$$

where $\mu(\frac{a}{a_0})$ is the "extrapolating function" and depends on a parameter $a_0 \approx 1.2\times10^{-12}ms^{-2}$. Thus, although for $a_0 << a$ Newton's second law remains valid, in the so-called "deep-MOND" regime, it is modified to

$$F = m\frac{a^2}{a_0}, \quad (a << a_0). \tag{3.29}$$

Consequently, for the circular motion of an object with mass m around another object with mass M one has

$$\frac{GmM}{r^2} = m\frac{(\frac{v^2}{r})^2}{a_0}. \tag{3.30}$$

Considering the above relation, it turns out that one can explain the so-called "flat rotation curves" of galaxies without any need of dark matter. Meantime, it is possible to interpret Eq.(3.30) as the modification of Newtonian gravity, leaving Newton's law intact. In such case, the modified gravitational potential is

$$\Phi = (GMa_0)^{\frac{1}{2}} lnr. \tag{3.31}$$

Thus, MOND proposes a modification of gravity according to Eq.(3.30) without any further need the dark matter. For M31, particularly, the rotation curves predicted by MOND seem to be inconsistent with observations [185].

We mention one more approach to describe the dark matter and dark energy within a single concept. Namely, considering the Newton's theorem on the equivalency of gravitational fields produced by sphere and that of the point, the weak-field limit of General Relativity is written as [21, 22]

$$g_{00} = 1 - \frac{2Gm}{rc^2} - \frac{\Lambda r^2}{3}; \;\; g_{rr} = (1 - \frac{2Gm}{rc^2} - \frac{\Lambda r^2}{3})^{-1}. \tag{3.32}$$

Then the cosmological constant enters naturally in the gravity equations (both General

Relativity and Newtonian one as its weak-field limit) which in its turn enables one to study the effect of Λ not only in the cosmological scales, but also in the Local Supercluster scale [21, 186]. Consequently, the virial theorem is written as

$$\sigma^2 = \frac{GM}{R} + \frac{\Lambda c^2 R^2}{6}, \tag{3.33}$$

while for rotational velocity we have

$$V(r)^2 = \frac{GM_d}{r} - \frac{\Lambda c^2 r^2}{3}. \tag{3.34}$$

This relation can be considered as further support to the conclusions in the previous sections, but now from entirely different point of view. Namely, as shown in [21, 22, 186] Eqs.(3.33),(3.34) are able to describe the dynamics of galactic halos and at higher scale galaxy configurations. However, if considering the dust mass obtained above as significant component of halos, one comes at contradiction i.e. the square of rotational velocity, V^2, according to Eq.(3.34) will decrease and even can become negative. That contradiction can either indicate the limitations of the model on that scales or that the actual contribution of dust in the halos has to be small.

3.3.5 Conclusion

We studied the thermal dust contribution in the M81 and M82 galactic halos' rotation, up to 25kpc. We found dust rotation velocities with three frequency bands and two dust models, using Doppler induced microwave temperature asymmetry data. We estimated the dust rotation velocities via dust mass, which again depends on the given frequency. We obtained the lower values of the dust opacity using Doppler formula for microwave temperature asymmetry and conclude that velocities obtained via microwave asymmetry data (with Doppler effect) has a higher value at 353 GHz band, with $V = 160 - 80$km/s for

DL07 dust model and $V = 14 - 10$km/s for GNILC model (both for M82 galaxy). Since the dust spectral index specifies the dust model, we considered DL07 model with $\beta = 2$ spectral index and GNILC of varying spectral index; the dust characteristic parameters significantly different for those models, hence vary the values of the dust velocities. In fact, spectral index is a crucial parameter through which almost all properties of the dust are being fixed.

We also analyzed the relevance of the obtained results to certain modified gravity models proposed to explain the dark matter indications including the flat rotation curves in galaxies. We mentioned a self-consistent approach to the dark matter problem based on Newton's theorem on sphere-point equivalency, where the cosmological constant Λ is introduced naturally in the weak-field General Relativity. The notable conclusion is that although we used different models, we arrived at the same conclusion on the minor role of the dust in the entire dynamical mass of the considered galaxies.

Conclusions

The main results of the thesis are as follows:

1. The Cosmic Microwave Background temperature maps obtained by the PLANCK satellite are analysed for 3 frequency bands and foreground-corrected SMICA band at $N_{side} = 2048$ in the HEALPix scheme in direction of two nearby edge-on galaxies.

2. Frequency independent temperature asymmetry is revealed for galaxies M81 and M104 indicating its Doppler-induced nature. The temperature asymmetry is shown to correlate with the direction of rotation of the galaxies. Thus the analysis of the cosmic microwave background temperature asymmetry for galaxies is shown to act as a direct tool in revealing the galactic halos and the intergalactic bridges, invisible in other bands or by other methods.

3. The parameters obtained by the CMB temperature asymmetry analysis regarding the galactic halo extensions are compared with the theoretical models for the baryonic dark matter profiles.

4. The role of the dust is analysed in the microwave radiation in 3 bands using the models of dust emission GNILC and DL07 and the phenomenological profiles of the dark matter configurations, thus revealing the contribution of dust, among other radiation mechanisms in deciphering the dark halo parameters. The obtained properties on the halo rotation are also analysed in the context of the modified gravity theories proposed to describe the baryonic dark matter configurations.

Bibliography

[1] Hamilton, A. J. S. *General Relativity, Black Holes, and Cosmology*, 226, 2018.

[2] Patrick P. and Uzan J-P., *Primordial cosmology*, Oxford University Press, 2013.

[3] Wald R. M., *General relativity*, University of Chicago Press, 2007.

[4] Liddle A., *An introduction to modern cosmology*, John Wiley & Sons, 2015.

[5] Rubakov V.A., and Gorbunov D.S., *Introduction to the Theory of the Early Universe: Hot big bang theory*, World Scientific, 2018.

[6] Raine D. J., and Thomas E.G., *An introduction to the science of cosmology. Series in Astronomy and Astrophysics*, 2001.

[7] Riess A.G., et al., AJ **116**, 1009, 1998.

[8] Perlmutter S., et al., ApJ, **517**, 565, 1999.

[9] Rich J., *Fundamentals of cosmology*, Springer, 2009.

[10] Thanu Padmanabhan, *Theoretical Astrophysics: Galaxies and Cosmology*, Cambridge University Press, 2002.

[11] Aghanim N. et al., arXiv:1807.06209, 2018.

[12] Zwicky F., *Die rotverschiebung von extragalaktischen nebeln*, Helvetica physica acta, **6**, 110, 1933.

[13] Smith S., Astrophys. J., **83**, 23, 1936.

[14] Rubin V. C. and Ford W.K. Jr, Astrophys. J. **159**, 379, 1970.

[15] Navarro J.F., Frenk C.S., White S.D.M., *ApJ*, **490**, 493, 1997.

[16] Burkert A., *ApJL*, **447**, L25, 1995.

[17] Moore B. et al., *MNRAS*, **310**, 1147, 1999.

[18] Milgrom M., *ApJ*, **270**, 365, 1983.

[19] Capozziello S., De Laurentis M., *Phys. Rep.,* **509**, 167, 2011.

[20] Sotiriou T.P., Faraoni V., *Rev. Mod. Phys.*, **82**, 451, 2010.

[21] V.G. Gurzadyan, *Eur. Phys. J. Plus* **134**, 14, 2019.

[22] V.G. Gurzadyan, A. Stepanian, *Eur. Phys. J. C* **78**, 632, 2018.

[23] Matilla J., Haiman Z., *Phys.Rev. D* (in press), arXiv: 1909.04690, 2019.

[24] Gurzadyan V.G., De Paolis F., Nucita A.A.; Kashin A.L., Amekhyan A., Sargsyan S., Yegorian G., Qadir A., Ingrosso G., Jetzer Ph., Vetrugno D., *A & A*, **609**, A131, 2018.

[25] Amekhyan A., Sargsyan S., Stepanian A., *Mod.Phys.Lett.*, **A 34**, 1950308, 2019.

[26] De Paolis F., Gurzadyan A.V., Nucita A.A., Gurzadyan V.G., Qadir A., Kashin A., Amekhyan A., Sargsyan S., Jetzer Ph., Ingrosso G., Tahir N., *A & A*, **629**, A87, 2019.

[27] Amekhyan A., *IJMPD*, **29**, 2040016, 2020; arXiv:1903.10757.

[28] Penzias A.A. and Wilson R., *Astrophys.J.*, **142**, 419, 1965.

[29] Smoot G.F. et al., *Astrophys. J.*, **396**, L1, 1992.

[30] Lueker Martin et al., *Astrophys. J.*, **719.2**, 1045, 2010.

[31] Kosowsky A., *New Astronomy Reviews*, **47.11-12**, 939-943, 2003.

[32] Bennett C. L. et al., *Astrophys. J.*, **583**, 1, 2003.

[33] Jarosik N. et al., *Astrophys. J. Supp.*, **170**, 263, 2007.

[34] Hinshaw G. et al., *Astrophys. J. Supp.*, **180**, 225, 2009.

[35] Jarosik N. et al., *Astrophys. J. Supp.*, **192**, 14, 2011.

[36] Hinshaw G. et al., *Astrophys. J. Supp.*, **208**, 19, 2013.

[37] Tauber J.A. et al., *A. & A.*, **520**, 1, 2010.

[38] Sunyaev R. A., Zeldovich Y. B., *Astrophysics and Space Science*, **7**, 3, 1970.

[39] Sunyaev R. A., Zeldovich Y. B., *Comments on Astrophysics and Space Physics*, **4**, 173, 1972.

[40] Kompaneets A. S., *Soviet Physics JETP*, **4**, 730, 1957.

[41] Ade P. A. R. et al., *A & A* , **596**, A101, 2016.

[42] Bolliet B. et al., arXiv:1906.10359, 2019.

[43] Maller A. H. and Bullock J.S., *MNRAS*, **355**, 694, 2004.

[44] Bullock J. S. et al., *Astrophys. J.*, **555.1**, 240, 2001.

[45] Bennett C. L. et al., *Astrophys. J. Lett.*, **464**, L1, 1996.

[46] Landau L. D. and Lifshits E. M., *Fizicheskaya Kinetika*, Moscow: Nauka, 1984.

[47] De Paolis F. et al., *A & A*, **299**, 647, 1995.

[48] Muciaccia P.F. et al., *Astrophys. J.* **488**, L63, 1997.

[49] Kunszt P.Z. et al., *Physics and astronomy.* In: Mining the Sky. ESO Astrophys. Symp., vol. 631., Springer, Berlin/Heidelberg 2001.

[50] Tegmark M., *Astrophys. J.*, **470**, L81, 1996.

[51] Crittenden R.G., Turok N.G, *Exactly Azimuthal Pixelizations of the Sky*, Report-no: **DAMTP-1998-78**, astro-ph/9806374, 1998.

[52] Gorski K.M.et al, *ApJ*, **622**, 759, 2005.

[53] Doroshkevich A.G., Verkhodanov O.V., *Phys. Rev.*, **D 83**, 3002, 2011.

[54] De Paolis, F. et al., *A & A* **534**, L8, 2011.

[55] Rauzy S. and Gurzadyan V. G., *MNRAS*, **298**, 114, 1998.

[56] De Paolis F., Gurzadyan V.G. et al., *A & A*, **L3**, 565, 2014.

[57] De Paolis F., Gurzadyan V.G. et al., *A & A*, **L8**, 580, 2015.

[58] Gurzadyan V.G., De Paolis F. et al., *A & A*, **A77**, 582, 2015.

[59] De Paolis F., Gurzadyan V.G. et al., *A & A*, **A57**, 593, 2016.

[60] V.G. Gurzadyan et al, *A & A*, **A131**, 609, 2018.

[61] Gerke J. R., Kochanek C. S., et al., *ApJ*, 743, 176 2011.

[62] Planck Collaboration I, *A & A*, **A12**, **594**, 2016.

[63] Planck Collaboration XVI, *A & A*, **A16**, **594**, 2016.

[64] Chiboucas K, Karachentsev I. D & Tully R.B., *AJ*, **137**, 3009, 2009.

[65] Pfenniger D., Combes F. & Martinet L., *A & A*, **285**, 79, 1994.

[66] Gerhard O. E. & and Silk J., *ApJ*, **472**, 34, 1996.

[67] Cooray A. & Chen X., *ApJ*, **573**, 43, 2002.

[68] Chluba J. & Mannheim K., *A & A*, **396**, 419, 2002.

[69] Oehm W., Thies, I. & Kroupa P., *MNRAS*, **467**, 273, 2017.

[70] Yun M. S., Ho P. T. P. & Lo K. Y., *Nature*, **372**, 530, 1994.

[71] Karachentsev I. D., Dolphin A. E. & Geisler D., *A & A*, **383**, 125, 2002.

[72] Bremnes T., Binggeli B. & Prugniel P., *A & AS*, **129**, 313, 1998.

[73] Makarova L.N., Grebel E.K. & Karachentsev I.D., *A & A*, **396**, 473, 2002.

[74] Liu J.-F., Bai Y., Wang S. et al., *Nature*, **528**, 108, 2015.

[75] Arp H., *Science*, **148**, 363, 1965.

[76] Sun W.-H., Zhou X. et al., *ApJ*, **630**, L133, 2005.

[77] de Mello D.F., Smith L.J. et al., *AJ*, **135**, 548, 2008.

[78] Sollima A., Gil de Paz A. et al., *A & A*, **516**, A83, 2010.

[79] Davies J.L., Wilson C.D. et al., *MNRAS*, **409**, 102, 2010.

[80] Sandage A., *AJ*, **81**, 954, 1976.

[81] de Vries H.W., Heithausen A. & Thaddeus P., *ApJ*, **319**, 723, 1987.

[82] Heithausen A., *A & A*, **A21**, 543, 2012.

[83] Heithausen A., *A & A*, **L41**, 393, 2002.

[84] Cortese L., Bendo G.J. et al., *MNRAS*, **403**, L26, 2010.

[85] Barker M.K., Ferguson A.M.N. et al., *AJ*, **138**, 1469, 2009.

[86] Habibi F., Moniez M., Ansari R. & Rahvar S., *A & A*, **A108**, 525, 2011.

[87] Nicastro F., Senatore F. et al., *MNRAS*, **457**, 676, 2016.

[88] Lovell M.R., Bose S. et al, *MNRAS*, **468**, 4285, 2017.

[89] Piras D., Joachimi B. et al, arXiv:1707.06559, 2017.

[90] Pace VanDevender J., VanDevender A.P. et al., *Nature Scientific Reports*, **7**, 8758, 2017.

[91] Gurzadyan V.G. & Kocharyan A.A., *A & A*, **L61**, 493, 2009.

[92] Hazumi M., Borrill J. et al., *Proc. SPIE*, **8442**, 844219, 2012.

[93] Abazajian K.N., Adshead, P. Ahmed Z. et al., arXiv:1610.02743, 2016.

[94] Finelli F., Bucher M. et al., *(CORE Collaboration)*, arXiv:1612.08270, 2016.

[95] Kogut A., Fixsen D.J. et al., *JCAP*, **7**, 025, 2011.

[96] Liu H., von Hausegger S. & Naselsky P., arXiv:1705.05530v1, 2017.

[97] Cen R. & Ostriker J.P, *ApJ*, **514**, 1, 1999.

[98] Cen R. & Ostriker J.P, *ApJ*, **650**, 560, 2006.

[99] Gupta A. et al., *ApJ*, **756**, L8, 2012.

[100] Fraser-McKelvie A. et al., *MNRAS*, **415**, 961, 2011.

[101] De Paolis F., Ingrosso et al., *Phys. Rev. Lett.*, **74**, 14, 1995.

[102] Nieuwenhuizen T.M. et al., *Physica Scripta*, **T151**, 014085, 2012.

[103] Schmidt F. & Kamionkowski M., *Phys.Rev.D*, **82**, 103002, 2010.

[104] Bertone G., Particle dark matter, *Cambridge University Press*, 2013.

[105] Somerville R.S. et al., *MNRAS*, **473**, 2714, 2018.

[106] Kravtsov A.V., *ApJ*, **764**, L31, 2013.

[107] Moradinezhad Dizgah et al., *Phys. Rev.D*, **88**, 063513, 2013.

[108] An H. et al., *PRD 97.*, **123528**, 2017.

[109] Weinberg S., *Phys. Rev. D* , **70**, 083522, 2004.

[110] De Paolis F. et al., *A & A*, **299**, 647, 1995.

[111] Baxter et al., *JCAP*, **6**, 1, 2019.

[112] Fabian A.C. & Nulsen P.E.J.,*MNRAS*, **269**, 33, 1994.

[113] De Paolis F., *ApJ*, **500**, 59, 1998.

[114] Draine B.T., *ApJ*, **509**, L41, 1998.

[115] Walker M. & Wardle M., *ApJ*, **498**, L125, 1998.

[116] Lim S. et al., arXiv:1712.08619, 2017.

[117] Jardel J.R., *ApJ*, **739**, 21, 2011.

[118] Tempel E. & Tenjes P.,*MNRAS*, **371**, 1269, 2006.

[119] Adam R., Ade P.A.R. et al., *A & A*, **A1**, 594, 2016.

[120] Ade P.A.R., Aghanim N. et al., *A & A*, **A16**, 594, 2016.

[121] Jardel J.R., Gebhardt K., Fabricius M. & Drory N., *ApJ*, **739**, 21, 2011.

[122] Bridges T.J., et al., *MNRAS*, **284**, 376, 1997.

[123] Bridges T.J. et al., *ApJ*, **658**, 980, 2007.

[124] Li Z., Jones et al., *ApJ*, **730**, 84, 2011.

[125] Li Z. et al., *ApJ*, **721**, 1368, 2010.

[126] Tahir N., De Paolis F., Qadir A. & Nucita A.A., *IJMPD*, **28**, 1950088, 2019.

[127] Igarashi A., Mori M. & Nitta S., *MNRAS*, **444**, 1177, 2014.

[128] Wagner S.J., Dettmar R.J. & Bender R., *A & A*, **215**, 243, 1989.

[129] Gadotti D.A. & Sánchez-Janssen R., *MNRAS*, **423**, 877, 2012.

[130] Gurzadyan V.G. et al., *A & A*, **497**, 343, 2009.

[131] Ade P.A.R., et al., *ApJ*, **794**, 171, 2014.

[132] Liu H., von Hausyger S. & Naselsky P., *Phys. Rev.*, **D95**, 103517, 2017.

[133] A.V. Kravtsov, *Ap J Lett*, **764** (2013) L31.

[134] R. Feldmann, C.-A. Faucher-Giguère, D. Kereš, arXiv:1901.09039, 2019.

[135] T. Okumura et al, PRD, **92**, 103516, 2015.

[136] A. Tamm et al, *A & A*, **A4**, 546, 2012.

[137] Y. Sofue, *PASJ*, **67**, 4, 2015.

[138] E. Tempel, A. Tamm, P. Tenjes, arXiv:0707.4374, 2007.

[139] B.T. Draine, A. Li, *ApJ*, **657**, 810, 2007.

[140] P.A.R. Ade et al, *A & A*, **A28**, 582, 2015.

[141] A. Abergel et al, *A & A*, **A11**, 571, 2014.

[142] P.A.R. Ade et al, *A & A*, **A132**, 586, 2016.

[143] R.H. Hildebrand, *QJRAS*, **24**, 267, 1983.

[144] A. Abergel et al, *A & A*, **A55**, 566, 2014.

[145] X. Dupac et al, *A& A*, **L11**, 404, 2003.

[146] A. Abergel et al, *A & A*, **A25**, 536, 2011.

[147] M. Juvela et al, *A & A*, **A33**, 541, 2012.

[148] P.A.R. Ade et al, *A & A*, **A45**, 564, 2014.

[149] N. Aghanim, et al, *A & A*, **A109**, 596, 2016.

[150] P.A.R. Ade et al, *A & A*, **A9**, 571, 2014.

[151] Ade P. A. R. et al, *A & A*, **A132**, 586, 2016.

[152] M. Haas et al, *A & A*, **L33**, 338, 1998.

[153] A. Kong et al, *ApJ*, **585**, 298, 2003.

[154] M. Montalto, et al, *A & A*, **507** (2009) 283.

[155] P. A. R. Ade et al., *A&A*, **A13**, 594, 2016.

[156] F. De Paolis et al., *A & A*, **299**, 647, 1995.

[157] B.T. Draine, A. Li, *ApJ*, **657**, 810, 2007.

[158] N. Aghanim et al., *A & A*, **A109**, 596, 2016.

[159] Suzuki T. et al., *PASJ*, **59.sp2**, S473-S481, 2007.

[160] R. Adam et al., *A & A*, **A8**, 594, 2016.

[161] W.L. Freedman et al., *ApJ*, **427**, 628, 1994.

[162] C.P. Blackman et al., *MNRAS*, **189**, 751, 1979.

[163] N.M. Forster Schreiber et al., *ApJ*, **552**, 544, 2001.

[164] C.M. Telesco et al., *ApJ*, **369**, 135, 1991.

[165] Y. Sofue, *PASJ*, **50**, 227 1998.

[166] N.I. Gaffney *et al.*, *ApJ*, **407**, L57, 1993.

[167] Y.D. Mayya et al., *ApJ*, **628**, L33, 2005.

[168] J.S. Young et al., *ApJ*, **287**, 153, 1984.

[169] Y.D. Mayya et al., *ApJ*, **679**, 404, 2008.

[170] J.P. Greco et al., *ApJ*, **757**, 24, 2012.

[171] P. Martini et al., *ApJ* **856**, 61, 2018.

[172] A. Abergel et al., *A & A*, **A11**, 571, 2014.

[173] R. Shetty et al., *ApJ*, **696**, 676, 2009.

[174] T. Nikola et al., *ApJ*, **749**, L19, 2012.

[175] G. Thuma et al., astro-ph/0004182, 2000.

[176] D.H. Hughes et al., *MNRAS*, **244**, 759, 1990.

[177] D.H. Hughes et al., *MNRAS*, **270**, 641, 1994.

[178] I.D. Karachentsev et al., *AJ*, **127**, 2031, 2004.

[179] G.J. Bendo et al., *A & A*, **L65**, 518, 2010.

[180] *The DustPedia Archive*, http://dustpedia.astro.noa.gr/

[181] J. Gunn, J.R. Gott, *ApJ*, **176**, 1, 1972.

[182] Merritt M., *AJ*, **132**, 6, 2006.

[183] Einasto J., *Trudy Inst. Astrofiz.*, **5**, 87, 1965.

[184] Brans H.C., Dicke R., *Phys. Rev.*, **270**, 124, 1961.

[185] Corbelli E., Salucci P., *MNRAS*, **374**, 1051, 2007.

[186] Gurzadyan V.G., Stepanian A., *Eur. Phys. J. C* **79**, 169, 2019.